UNIVERSIDADE ESTADUAL PAULISTA “JÚLIO DE MESQUITA FILHO”
FACULDADE DE ENGENHARIA
CAMPUS DE ILHA SOLTEIRA

KAYC WAYHS LOPES

THE EFFECT OF DAMAGE ON WAVE PROPAGATION IN PLATES WITH CIRCULAR PIEZOELECTRIC TRANSDUCERS

ILHA SOLTEIRA
2023

KAYC WAYHS LOPES

THE EFFECT OF DAMAGE ON WAVE PROPAGATION IN PLATES WITH CIRCULAR PIEZOELECTRIC TRANSDUCERS

Thesis submitted to the Faculdade de Engenharia de Ilha Solteira - UNESP in partial fulfillment of the requirements for obtaining the Doctorate degree in Mechanical Engineering.
Knowledge area: Solid Mechanics

Advisor: Prof. Dr. Douglas Domingues Bueno
Co-Advisor: Prof. Dr. Camila Gianini Gonsalez-Bueno

ILHA SOLTEIRA

2023

FICHA CATALOGRÁFICA
Desenvolvido pelo Serviço Técnico de Biblioteca e Documentação

L864e

Lopes, Kayc Wayhs.
The effect of damage on wave propagation in plates with circular piezoelectric transducers / Kayc Wayhs Lopes. -- Ilha Solteira: [s.n.], 2023
124 f. : il.

Tese (doutorado) - Universidade Estadual Paulista. Faculdade de Engenharia de Ilha Solteira. Área de conhecimento: Mecânica dos Sólidos, 2023

Orientador: Douglas Domingues Bueno
Co-orientador: Camila Gianini Gonsalez Bueno
Inclui bibliografia

1. Wave propagation. 2. Structural health monitoring. 3. Symmetric damage. 4. Circular piezoelectric transducers. 5. Optimal frequencies.

Amanda Sertori dos Santos
Bibliotecária - CRB/8-9061
Seção Técnica de Referência, Atendimento ao Usuário e Documentação
Diretoria Técnica de Biblioteca e Documentação

UNIVERSIDADE ESTADUAL PAULISTA

Câmpus de Ilha Solteira

CERTIFICADO DE APROVAÇÃO

TÍTULO DA TESE: THE EFFECT OF DAMAGE ON WAVE PROPAGATION IN PLATES WITH CIRCULAR PIEZOELECTRIC TRANSDUCERS

AUTOR: KAYC WAYHS LOPES

ORIENTADOR: DOUGLAS DOMINGUES BUENO

COORIENTADORA: CAMILA GIANINI GONSALEZ BUENO

Aprovado como parte das exigências para obtenção do Título de Doutor em Engenharia Mecânica, área: Mecânica dos Sólidos pela Comissão Examinadora:

Prof. Dr. DOUGLAS DOMINGUES BUENO (Participaçao Virtual)
Departamento de Matematica / Faculdade de Engenharia de Ilha Solteira - UNESP

Dr. DANILO BELI (Participaçao Virtual)
Mechanical Engineering Department / Eindhoven University of Technology, Netherlands

Prof. Dr. FABRICIO CESAR LOBATO DE ALMEIDA (Participaçao Virtual)
Departamento de Engenharia Mecânica / Faculdade de Engenharia - UNESP

Prof. Dr. TOBIAS SOUZA MORAIS (Participaçao Virtual)
Departamento de Engenharia Aeronáutica / Universidade Federal de Uberlândia - UFU

Prof. Dr. CARLOS DE MARQUI JUNIOR (Participaçao Virtual)
Departamento de Engenharia Aeronáutica / Universidade de São Paulo - USP

Ilha Solteira, 20 de setembro de 2023

To my wonderful wife, Larissa.

Acknowledgments

I would like to thank God for everything He has done in my life.

I would like to thank my wife and best friend, Dr. Larissa Drews Wayhs Lopes, for her support, friendship, and for always being by my side. I always look up to her and I'm very grateful for having her in my life.

Many thanks to my parents, Gláucio Lopes and Sueli Lopes, for always encouraging me to keep studying. They did everything they could for me to have a good education. To my siblings, Carla, Kaio and Cauana, and my nephews, Iggor and Leonardo. I also would like to thank all the people from my family for all their support.

I would like to give thanks to Prof. Dr. Douglas Bueno for more than five years of guidance and friendship. Prof Douglas always helped me when needed, and I could not do this thesis without his advice. He is always concerned about the well-being of his students. I'm glad I have him as a friend and advisor. Many thanks to Prof. Daniel Inman from the University of Michigan, who allowed me to work in his lab (AIMS laboratory) for one year. I had a great time there and I will remember it for the rest of my life. Prof Inman helped me a lot and I'm thankful for all the things he did for me and for having him as a mentor. I also would like to thank Prof. Dr. Camila Gonsalez-Bueno for her help, especially when I started in the SHM and wave propagation areas.

Many thanks to my in-laws, Ricardo Wayhs, Márcia Wayhs, Gabriela and Bárbara, for all their support, especially during the pandemic time.

I would like to thank my friends Dr. Renan Geronel and Dr. Frederico Ribeiro, with whom I had the pleasure to share the office during the first year of the Ph.D. Many thanks to my friend Jessé Paixão for all the coffees and talks we had in the first year of the Ph.D. Those talks were very helpful. I also thank my friends Eduardo Preto, Matheus Donatoni, Rubens Manrique, Matheus Lima and Luciano Maia, with whom I have been friends since we started undergraduate together. Many thanks to my friends from the University of Michigan for all the time we had together, especially my lab mates, Dr. Christina Harvey, Dr. Kevin Haughn, Dr. Piper Sigrest, Greta Colford and Elliot Kimmel.

Thanks to all the employees from UNESP, PPGEM and the Department of Mechanical Engineering from FEIS/UNESP. I would like to thank the support of Carlos José Santana for his help in carrying out the experimental tests and José Carlos Melo for his help in processes related to FAPESP.

I would like to give thanks to the São Paulo Research Foundation (FAPESP), grant numbers 2019/21149-9 and 2021/11493-4, and the Brazilian National Council for Scientific and Technological Development (CNPq), grant number 133397/2019-0, for providing financial support for my Ph.D.

''Trust in the Lord with all your heart and lean not on your own understanding; in all your ways submit to Him, and He will make your paths straight.''

Proverbs 3:5-6

Abstract

Damage detection using Structural Health Monitoring (SHM) techniques is a challenge with increasing importance for the scientific community. SHM processes usually involve selecting actuators to excite the structure and sensors to measure outputs. The sensor outputs are post-processed to detect the damage. Usually, aspects such as the size and location of the actuators and sensors, and the choice of the excitation frequency are neglected in SHM campaigns, and they are very relevant to many damage detection algorithms. This thesis presents an approach to define the sensor's size in terms of its position in the structure considering the scattering of longitudinal and flexural waves in damaged plate-like structures. Modeling is developed to compute each wave packet of reflected and transmitted waves separately, which allows one to describe the wave scattering in thin plates with symmetric damage. Numerical simulations are carried out and the results show that the sensor size can be adjusted to improve the damage detection process. Results from experimental tests are presented to demonstrate the approach considering circular actuators. A damage index $\bar{R}$ is introduced and used to detect the damage. The modeling of circular piezoelectric transducers bonded to thin plates is also presented, and it demonstrates that there are optimal frequencies to create and measure these waves. In addition, new equations to compute the sensors' output voltages in terms of the actuator input voltage applied are presented and demonstrated from experimental tests. The findings contribute to SHM systems based on longitudinal and flexural wave propagation to detect damage in plate-like structures. They contribute to the current state of the art in wave propagation SHM by investigating the effects of different excitation frequencies and the influence of the damage parameters and sensor sizing on the resulting waves.

Keywords: wave propagation; structural health monitoring; symmetric damage; circular piezoelectric transducers; optimal frequencies.

Resumo

Detecção de danos via técnicas de Monitoramento da Integridade Estrutural (SHM, do inglês *Structural Health Monitoring*) é um desafio com crescente importância para a comunidade científica. Processos de SHM geralmente envolvem a seleção de atuadores para excitação da estrutura e sensores para medir as respostas. As respostas obtidas com os sensores são pós-processadas para detectar o dano. Normalmente, aspectos como o tamanho e localização dos atuadores e sensores, e a escolha da frequência de excitação são negligenciados nas campanhas de SHM, embora sejam muito relevantes para qualquer algoritmo de detecção de danos. Esta tese apresenta uma metodologia para definir o tamanho do sensor em termos de sua posição na estrutura, considerando a dispersão de ondas longitudinais e de flexão em estruturas do tipo placa. A modelagem é desenvolvida para se obter separadamente cada pacote de onda refletida e transmitida, o que permite descrever a dispersão da onda em placas finas com danos simétricos. Simulações numéricas são apresentadas e os resultados mostram que o tamanho do sensor pode ser ajustado para melhorar a detecção do dano. Resultados de testes experimentais são apresentados para demonstrar a abordagem considerando um atuador circular. Um índice de dano $\bar{R}$ é proposto e usado para detectar o dano. A modelagem de transdutores piezoelétricos circulares para gerar e capturar ondas longitudinais e de flexão também é apresentada. Ela permite demonstrar que existem frequências ótimas para criar e medir essas ondas. Além disso, novas equações são apresentadas e demonstradas para calcular as tensões elétricas de saída medidas pelos sensores em termos da tensão de entrada aplicada ao atuador. Os resultados contribuem para a evolução de sistemas de SHM baseados na propagação de ondas longitudinais e flexurais para detectar danos em placas e, também para o estado da arte na propagação de ondas para SHM, abordando os efeitos de diferentes frequências de excitação e a influência dos parâmetros de dano e dimensão de sensor.

Palavras-chave: propagação de ondas; monitoramento da integridade estrutural; dano simétrico; transdutores piezoelétricos circulares; frequências ótimas.

List of Figures

List of Tables

List of Acronyms

ASM	-	Average Scattering Matrix
BEM	-	Boundary Element Method
PZT	-	Piezoelectric transducer
SEM	-	Spectral Element Method
SHM	-	Structural Health Monitoring
TFM	-	Total Focusing Method

List of Symbols

$\bar{\mathbf{a}}$	-	Wave amplitude vector of longitudinal waves
$\mathbf{a}$	-	Wave amplitude vector of flexural waves
A_1	-	Flexural wave amplitude propagating in the y positive direction and attenuating in the x negative direction
A_2	-	Flexural wave amplitude propagating in the y positive direction and attenuating in the x positive direction
A_3	-	Flexural wave amplitude propagating in the y positive direction and in the x negative direction
$A_3^{()}$	-	Flexural wave amplitude A_3 at the point ()
A_4	-	Flexural wave amplitude propagating in the x and y positive directions
$A_4^{()}$	-	Flexural wave amplitude A_4 at the point ()
$A_r^{()}$	-	Reflected wave amplitude at the point ()
A_r	-	Reflected wave amplitude
$A_r^{()}\|_{(n)}$	-	Reflected wave amplitude of the n-th packet
$A_r\|_{(n)}^{\theta_{()}}$	-	Reflected wave amplitude of the n-th packet propagating with angle $\theta_{()}$
$A_t^{()}$	-	Transmitted wave amplitude at the point ()
A_t	-	Transmitted wave amplitude
$A_t^{()}\|_{(n)}$	-	Transmitted wave amplitude of the n-th packet
$A_t\|_{()}^{\theta_{()}}$	-	Transmitted wave amplitude of the n-th packet propagating with angle $\theta_{()}$
$A_t\|_c$	-	Amplitude of the resulting transmitted wave in case of circular wave propagation
$A_i^{()}$	-	Incident wave amplitude at the point ()
A_{ru}	-	Longitudinal wave amplitude propagating to the positive directions of x and y
$A_{ru}^{()}$	-	Longitudinal wave amplitude A_{ru} at the point ()
A_{rui}	-	Incident longitudinal wave amplitude A_{ru}
$A_{rui}^{()}$	-	Longitudinal wave amplitude A_{rui} at the point ()
A_{lu}	-	Longitudinal wave amplitude propagating to the negative direction of x and positive direction of y

$A_{lu}^{()}$ - Longitudinal wave amplitude A_{lu} at the point ()

A_{ld} - Longitudinal wave amplitude propagating to the negative directions of x and y

$A_{ld}^{()}$ - Longitudinal wave amplitude A_{ld} at the point ()

A_{rl} - Longitudinal wave amplitude propagating to the positive direction of x and negative direction of y

$A_{rl}^{()}$ - Longitudinal wave amplitude A_{rl} at the point ()

$B_{()}$ - Potential function amplitude

c - Distance between centers of actuator and sensor

c_l - Phase velocity of the longitudinal wave

c_f - Phase velocity of the flexural wave

$C_{t(.)}$ - Coefficient defined by the ratio between amplitudes of the transmitted and incident longitudinal waves

$C_{r(.)}$ - Coefficient defined by the ratio between amplitudes of the reflected and incident longitudinal waves

D_p - Flexural rigidity computed with properties of the undamaged region of the plate

d_x - Distance between two points in the x direction

d_y - Distance between two points in the y direction

E_{eq} - Equivalent Young's modulus

E_a - Young's modulus of the actuator

E_s - Young's modulus of the sensor

E_p - Young's modulus of the undamaged region of the plate

$\bar{E}_p$ - Young's modulus of the beam used to create the damaged section

E_d - Young's modulus of the damaged region of the plate

E_r - Energy of the reflected longitudinal wave

$E_r|_{(1)}$ - Energy of the first reflected longitudinal wave packet

E_t - Energy of the transmitted longitudinal wave

$E_t|_{(1)}$ - Energy of the first transmitted longitudinal wave packet

f_{opt}^l - Optimal frequency for damage detection with longitudinal wave

f_{opt}^f - Optimal frequency for damage detection with flexural wave

f_o^l - Optimal frequency to create and measure longitudinal waves with circular piezoelectric transducers

f_o^f - Optimal frequency to create and measure flexural waves with circular piezoelectric transducers

G_p	-	Shear modulus of the undamaged region of the plate
h	-	Ratio between h_d and h_p
$\bar{\mathbf{h}}$	-	Longitudinal wave state vector
$\mathbf{h}$	-	Flexural wave state vector
$\bar{\mathbf{H}}$	-	Longitudinal wave transformation matrix
$\mathbf{H}$	-	Flexural wave transformation matrix
$(\ )_p$	-	( ) computed with properties of the undamaged region of the plate
$(\ )_d$	-	( ) computed with properties of the damaged region of the plate
h_a	-	Actuator thickness
h_s	-	Sensor thickness
h_d	-	Damage thickness
h_p	-	Plate thickness
k_l	-	Longitudinal wavenumber
$\mathbf{i}, \mathbf{j}$	-	Unitary vectors in the x and y directions, respectively
i	-	Pure imaginary number
k_1	-	Component of the longitudinal wavenumber in the x direction
k_2	-	Component of the longitudinal wavenumber in the y direction
$k_{l(p)}$	-	Longitudinal wavenumber computed with properties of the undamaged region of the plate
$k_{l(d)}$	-	Longitudinal wavenumber computed with properties of the damaged region of the plate
k_f	-	Flexural wavenumber
$k_{f(p)}$	-	Flexural wavenumber computed with properties of the undamaged region of the plate
$k_{f(d)}$	-	Flexural wavenumber computed with properties of the damaged region of the plate
L_x,L_y	-	Dimensions of the plate in the x and y directions, respectively
l_x	-	Damage length in the x direction
$L_{y(d)}$	-	Damage length in the y direction
M_x,M_y	-	Bending moments along the x and y directions, respectively
M_{xy},M_{yx}	-	Twisting moments
N_x, N_y	-	Line forces per unit of displacement in the x and y directions, respectively
Q_x,Q_y	-	Shear forces

r_L	-	Circular sensor radius on the left-hand side of the damage
r_R	-	Circular sensor radius on the right-hand side of the damage
r_a	-	Circular piezoelectric transducer radius working as actuator
r_s	-	Circular piezoelectric transducer radius working as sensor
$\bar{R}$	-	Damage index
$\bar{R}_l$	-	Threshold value for damage detection
t	-	Time
$\bar{\mathbf{T}}$	-	Longitudinal wave spatial transformation matrix
$\mathbf{T}$	-	Flexural wave spatial transformation matrix
V_{in}	-	Input voltage applied to the actuator
V_{out}	-	Output voltage measured by the sensor
w	-	Transversal displacement
u, v	-	Longitudinal displacements respectively in the x and y directions
x, y, z	-	Coordinates of the reference system

Greek Letters

α, ϕ	-	Angles between direction of flexural wave propagation and the x axis
∇	-	Gradient operator
∇^2	-	Laplacian
φ	-	Scalar function representing the potential linear displacement
$\boldsymbol{\psi}$	-	Potential angular displacement
ρ_{eq}	-	Equivalent density
ρ_p	-	Plate material density of the undamaged region
$\bar{\rho}_p$	-	Beam material density used to represent the damaged section
ρ_d	-	Plate material density of the damaged region
ν_p	-	Plate Poison's coefficient of the undamaged region
ν_d	-	Plate Poison's coefficient of the damaged region
ν_a	-	Actuator Poison's coefficient
ν_s	-	Sensor Poison's coefficient
$\lambda_{f(p)}$	-	Flexural wavelength computed with properties of the undamaged region of the plate
$\lambda_{f(d)}$	-	Flexural wavelength computed with properties of the damaged region of the plate
$\lambda_{l(p)}$	-	Longitudinal wavelength computed with properties of the undamaged region of the plate
$\lambda_{l(d)}$	-	Longitudinal wavelength computed with properties of the damaged region of the plate
θ	-	Angle between direction of longitudinal wave propagation and the x axis
θ_1	-	Angle between direction of longitudinal wave propagation and the x axis for the first wave packet captured by the sensor in case of radial longitudinal wave
θ_2	-	Angle between direction of longitudinal wave propagation and the x axis for the second wave packet captured by the sensor in case of radial longitudinal wave
θ_x,θ_y	-	Slopes along the x and y directions, respectively
ω	-	Angular frequency

Contents

1 INTRODUCTION

This first chapter presents a brief motivation and the literature review, the objectives, the main contributions, and the outline of this thesis.

1.1 MOTIVATION AND LITERATURE REVIEW

Engineers and researchers have developed numerous techniques for structural health monitoring (SHM) to detect incipient damage, mainly focused on contributing to reducing costs of maintenance and improving safety in a variety of structures and machines (BAPTISTA *et al.*, 2014; LOPES JR *et al.*, 2000; FILHO; BAPTISTA; INMAN, 2011b; GONSALEZ *et al.*, 2015; SILVA; GONSALEZ; LOPES JR., 2011).

SHM systems are usually classified into the following levels: *i*) damage detection; *ii*) damage detection and location; *iii*) damage detection, location and quantification; *iv*) damage detection, location, quantification and prediction of useful life of structure (DOEBLING; FARRAR; PRIME, 1998). Many approaches in the literature are focused on post-processing input and output signals obtained experimentally by using actuators and sensors placed on the structure (HENDRICK, 1988; POVICH; LIM, 1994; RHIM; LEE, 1995; STASZEWSKI, 2002; DASGUPTA *et al.*, 2004; LEE; KIM, 2007; AI *et al.*, 2018). Filho, Baptista and Inman (2011a) for example present a new methodology for damage detection based on the magnitude of the coherence function computed with the signals obtained by piezoelectric transducers coupled to the host structure. The authors carried out experimental tests on healthy and damaged aluminum plates, computing the coherence index for the measured signals and they concluded that the approach is efficient for damage detection. In SHM applications, computational tools can be also involved, as presented by references Wu, Ghaboussi and Garrett (1992), Spillman *et al.* (1993), Doebling *et al.* (1996), and others.

SHM techniques based on post-processing input and output signals usually are demonstrated considering experimental data obtained from well-controlled tests conducted in laboratories. In these last years, authors have considered more signals and included statistic-based procedures to infer a general efficiency of their methods based on their particular findings. However, SHM techniques have also been developed by investigating the wave propagation in the structure. Gonsalez-Bueno (2019) presents a strategy for monitoring beams with corrosion like-damage. The author considers longitudinal and flexural waves to demonstrate the wave interactions with symmetric and asymmetric damage. Optimum frequencies are defined to improve damage detectability. Piezoelectric transducers are employed to obtain experimental data to validate the accuracy of the proposed modeling.

Modeling wave propagation in structures allows one to investigate different issues in engineering, as shown in references (SZEFI, 2003; NASCIMENTO, 2009; EBRAHIMIAN; TODOROVSKA, 2014; NANDA; KAPURIA, 2015; NUCERA *et al.*, 2015; SANTOS, 2018), and others. Ahmida and Arruda (2002) obtain structural vibration modes from wave propagation using the Spectral Element Method (SEM). The authors introduce a parameter to measure the structural mode complexity. Mace (1984) investigates the vibration behavior of beams considering the effect of geometric discontinuity. The article shows the importance of near-field waves for computing the amplitude of motion accurately. Santos *et al.* (2021) present a strategy to design periodic rods for flexural wave propagation for vibration supressions in mechanical structures. The authors obtain mathematical relations to compute the transmitted wave in terms of the incident wave and involving physical and geometrical properties of the structure, contributing to the design of an efficient structure to exhibit desired stop band. However, relatively fewer efforts have investigated wave propagation focused on developing SHM techniques (LEE; STASZEWSKI, 2003; MAL *et al.*, 2005; RYUE *et al.*, 2011; GONSALEZ-BUENO, 2019).

Luca *et al.* (2022) investigate the wave propagation phenomena in isotropic and anisotropic plates to understand the guided wave dispersion and highlight their differences. Their work contributes to an improvement in the design of SHM systems based on guided waves. In addition, the authors investigate the scattering due to a stiffener in aluminum and composite plates and show different effects between these two materials. Perfetto *et al.* (2023a) investigate guided waves on composite-type structures with curvature and compare the results with numerical simulations obtained for a flat plate. They noted more differences for the S_0 lamb wave mode propagation at the low-frequency range of excitation. On the other hand, no differences are observed for the A_0 lamb wave mode propagation.

Mechanical structures commonly operate under effects of different environmental conditions and load levels, which affect the wave propagation in the structures (PERFETTO *et al.*, 2022; PERFETTO *et al.*, 2023b; LUCA *et al.*, 2023). Then, Perfetto *et al.* (2022) investigated how guided waves (A_0 and S_0 lamb wave modes) propagate under the influence of temperature effects using the Finite Element Method for a composite-type plate. They also present results from experimental tests, which show that an increase in the temperature results in decreasing the group velocity of the S_0 lamb wave mode due to the decrease in the mechanical properties of the composite. On the other hand, they show that the group velocity of the A_0 lamb wave mode is less sensitive to changes in temperature. Their work provides an important contribution to the improvement of SHM systems based on guided waves considering the influence of temperature.

The effects of geometric discontinuities on the coefficients of transmission and reflection waves are investigated by Cho (2000), Schaal and Mal (2016) and Poddar and Giurgiutiu (2016) considering plate-like structures with cross-section changes. Thickness increasing and decreasing are employed to represent the discontinuity. On the other hand, different geometric shapes are considered in references Cho and Rose (2000), Lowe *et al.* (2002), Martin and Jata (2007), Benmeddour *et al.* (2008), Roberts (2008), Kim and Roh (2011), Ajith and Gopalakrishnan (2013), Glushkov *et al.* (2015), Pau and Achillopoulou (2017), Haider *et al.* (2018), Bhuiyan *et al.* (2018) and Kubrusly, Weid and Dixon (2019). Lowe and Diligent (2002) investigate the coefficient of reflection in a plate considering an asymmetrical rectangular crack considering the S_0 Lamb wave. The authors show that resulting wave amplitudes exhibit periodic behavior, with maximum and minimum magnitude depending on the damage and excitation frequency. They highlight the importance of understanding this dynamic behavior for detecting the damage via non-destructive-based techniques considering the S_0 lamb wave.

Pain and Drinkwater (2013) highlight that composite-materials-based structures have fibers that can present waviness, which can affect their mechanical strength. The authors introduce two methodologies to detect the waviness: which involve a post-processing algorithm of images called TFM (Total Focusing Method) and the Average Scattering Matrix (ASM) method. Experimental tests are carried out considering different levels of waviness. According to the authors, the phase TFM imaging presents potential to obtain the image of the waviness, especially for larger levels. They indicate that ASM shows a good performance to investigate the scattering of the waves and conclude that additional experimental tests are required to investigate the limitations of both techniques. Considering the case of Lamb waves, Ng and Veidt (2011) studies the wave scattering due to incidence of an A_0 Lamb Wave mode in the delamination of a composite plate using a 3D model. They employ the Finite Element method for a low-frequency range to detect and characterize the damage using the wave scattered amplitudes. The approach predicts the wave scattering field, including its characteristics, such as amplitudes and directions in terms of the delamination size and wavelength.

The wave interaction with stiffened plates has been investigated by Martin and Jata (2007), Roberts (2008), Ajith and Gopalakrishnan (2013), Haider *et al.* (2018) and Bhuiyan *et al.* (2018). Usually the studies consider incident wave perpendicular to the damage. However, if an oblique incidence is considered, He *et al.* (2020) and Santhanam and Demirli (2013) show that there are important variations in the transmitted and reflected wave amplitude and phase. Golato, Demirli and Santhanam (2014) consider a symmetric damage and the S_0 and A_0 Lamb wave modes with incidence of zero and ninety degrees. The authors verified the influence of this angle of incidence on the transmitted and reflected wave energy. They noted for the S_0 Lamb wave mode that there are reflected shear waves for high incidence angles, and they are reduced for large damage.

Piezoelectric transducers have been used to investigate the best monitoring setups, which includes defining shapes of actuators and sensors to improve the damage detection and decrease false diagnoses. Giurgiutiu (2003), for example, presents an isotropic plate with a piezoelectric transducer attached to its surface and acting as actuator. The author obtains the displacement and strain for different Lamb wave modes, and the waves are created due to external voltage applied to the actuator. The pin-force model is used to relate the host structure and the piezoelectric transducer. Raghavan and Cesnik (2004) demonstrate the displacement and strain for different Lamb wave modes considering circular piezoelectric actuators. They also introduce equations to compute the output voltage for a rectangular piezoelectric sensor.

Raghavan and Cesnik (2005) present an approach to obtain the displacement and output voltage for arbitrary shapes of actuator and sensor, respectively. The transducers are bonded to an isotropic plate. The authors investigate two different shapes of actuators (rectangular and circular) and a rectangular sensor. Their results show that at certain frequencies some wave modes present higher amplitudes than other ones, and those frequencies depend on the actuator and sensor shapes and dimensions. Similar results are observed by Nienwenhui *et al.* (2005), Scalea, Matt and Bartoli (2007), Lin *et al.* (2012) and Lin and Giurgiutiu (2012).

Damage detection processes based on waves using piezoelectric transducers usually involve defining the best kind of wave to detect each type of damage, and the most convenient shape for the actuator. In addition, based on the actuator shape, it is important to establish the best excitation frequency to create the desirable wave. The shape for the sensor, and the relative position between the transducers are also relevant issues to be addressed. The Waveform Revealer 3.0 is a robust software developed by Shen and Giurgiutiu (2016) and Giurgiutiu (2022). The software allows one to investigate guided waves interactions with damages, and it provides different theoretical solutions for S_0 and A_0 lamb wave modes, including analytical waveforms for different shapes and kinds of piezoelectric transducers. Li, Khodaei and Aliabadi (2020) present a methodology called Boundary Element Method (BEM) and introduce an approach similar to the pin-force model to couple actuator and host structure to each other. The authors investigate damage effects on the waves using the Dual BEM. However, the effects of the piezoelectric transducers sizing on creating and collecting waves are neglected.

Based on this context, the present thesis considers the modeling of longitudinal and flexural waves propagating in damaged plate-like structures to obtain S_0 and A_0 lamb wave modes for low-frequency range. The classical formulation is provided by Giurgiutiu (2014c), and different algebraic rearrangements are carried out to investigate the influence of the damage on the wave propagation. Circular piezoelectric transducers are considered and an analytical approach is introduced to demonstrate the sensor output voltage in terms of the input voltage applied to the actuator. A new damage detection index is proposed and theoretical and experimental results are presented to demonstrate the findings, and they contribute to the improvement of SHM processes to detect damage in plate-like structures. The work presented herein is currently situated at a relatively low Technology Readiness Level (TRL) (MANKINS, 1995). However, it holds substantial promise for advancing SHM systems and stands as a step towards addressing challenges and improving the reliability, accuracy, and efficiency of SHM technologies.

1.2 OBJECTIVES

The main objective of this work is to investigate how longitudinal and flexural waves interact with symmetrical damages in plates with circular piezoelectric transducers. The specific objectives are summarized below:

- Develop a dynamic model in the frequency domain to describe longitudinal and flexural wave propagation in a damaged plate-like structure with circular piezoelectric transducers;

- Determine an approach to compute optimal frequencies to detect damages in plate-like structures in terms of the damage physical and geometrical properties;
- Obtain optimal frequencies to create and measure longitudinal and flexural waves using circular piezoelectric transducers, in terms of their physical and geometrical properties;
- Demonstrate the effect of longitudinal and flexural waves considering oblique incidence into symmetrical damaged sections.

1.3 MAIN CONTRIBUTIONS

The main contributions of this work to the literature are summarized below:

- An analytical approach in the frequency domain to compute longitudinal and flexural wave amplitudes in damaged plate-like structures including circular piezoelectric transducers;
- Analytical equations to compute optimal frequencies to create and acquire longitudinal and flexural waves with circular piezoelectric transducers coupled to plates;
- Optimal frequencies to detect damage using longitudinal and flexural waves in terms of the damage characteristics;
- The number of wave packets collected by circular piezoelectric sensors depending on their dimensions and relative position.

The main results of this work were published in the following journal articles:

- Lopes, Gonsalez-Bueno and Bueno (2022): "On the Frequencies for Structural Health Monitoring in Plates with Symmetrical Damage: An Analytical Approach". Journal of Nondestructive Evaluation (2022).
- Lopes *et al.* (2023b): "On the modeling of circular piezoelectric transducers for wave propagation-based structural health monitoring applications". Journal of Intelligent Material Systems and Structures (2023).
- Lopes *et al.* (2023a): "Longitudinal wave scattering in thin plates with symmetric damage considering oblique incidence". Ultrasonics (2023).

and in the following conferences:

- Lopes *et al.* (2021): "On the Frequencies for Structural Health Monitoring in Plates with Symmetrical Damage: An Analytical Approach". 26th International Congress of Mechanical Engineering (2021).
- Lopes *et al.* (2022): "On the Frequencies for Structural Health Monitoring in Plates with Asymmetrical Damage: An Analytical Approach". Health Monitoring of Structural and Biological Systems XVI, SPIE (2022).
- Lopes *et al.* (2023c): "On the Symmetric Damage Detection with Flexural Waves when using Circular Piezoelectric Transducers". Health Monitoring of Structural and Biological Systems XVII, SPIE (2023).

In addition, the following awards and achievements were obtained in international conferences:

- Best Student Paper Award - Bronze award, 32nd International Conference on Adaptive Structures and Technologies (ICAST 2022).
- Health Monitoring of Structural and Biological Systems Best Student Paper Award - Third place, SPIE Smart Structures + Nondestructive Evaluation 2023.

1.4 OUTLINE

This thesis is structured into the following chapters:

- **Chapter 1 - INTRODUCTION**: it covers the motivation and literature review, objectives, main contributions, and the general content of the thesis.
- **Chapter 2 - SENSOR SIZE AND OPTIMUM FREQUENCIES TO DETECT DAMAGE WITH LONGITUDINAL WAVES**: it presents the mathematical modeling of longitudinal wave propagation in thin plates with symmetrical damage. The scattering of the longitudinal wave and equations to compute the wave amplitudes of the wave packets for oblique incidence are introduced. The effect of the number of wave packets collected by the sensor is written in terms of its dimensions. Optimal frequencies for damage detection are also introduced. Numerical simulations are presented to demonstrate the proposed approach, and

experimental tests are carried out considering circular actuator and radial wave propagation.

- **Chapter 3 - FLEXURAL WAVES WITH OBLIQUE INCIDENCE**: it provides a detailed modeling of flexural wave propagation in thin plates with symmetrical damages.

- **Chapter 4 - CIRCULAR PIEZOELECTRIC TRANSDUCERS FOR SHM**: it shows the modeling of circular piezoelectric transducers coupled to thin plates used to create and measure longitudinal and flexural waves. New equations to compute the sensor output voltage in terms of the actuator input voltage are introduced. Optimal frequencies to create and measure the waves in terms of both PZTs and plate properties are also presented, and it is shown that their physical and geometrical parameters affect the measurements obtained by the sensors.

- **Chapter 5 - FINAL REMARKS:** comprises the final conclusions, and suggestions for future work.

2 SENSOR SIZE AND OPTIMUM FREQUENCIES TO DETECT DAMAGE WITH LONGITUDINAL WAVES

This chapter presents an approach to define the sensors size in terms of their position in the structure. The approach includes a strategy to determine the plate thickness reduction due to the damage presence by considering an oblique incidence of waves generated by the actuator. Modeling is developed to compute each wave packet of reflected and transmitted waves separately from each other, which allows one to describe the wave scattering in thin plates with symmetric damage.

2.1 LONGITUDINAL WAVE PROPAGATION IN THIN PLATES

The longitudinal displacements are denoted u and v respectively in the x and y directions in a rectangular plate. The displacements are related by the following equations of motion (GIURGIUTIU, 2014a; LOPES; GONSALEZ-BUENO; BUENO, 2022)

$$\begin{aligned}
&\frac{\partial^2 u}{\partial x^2} + \frac{(1-\nu_p)}{2}\frac{\partial^2 u}{\partial y^2} + \frac{(1+\nu_p)}{2}\frac{\partial^2 v}{\partial x \partial y} = \frac{(1-\nu_p^2)\rho_p}{E_p}\frac{\partial^2 u}{\partial t^2} \\
&\frac{\partial^2 v}{\partial y^2} + \frac{(1-\nu_p)}{2}\frac{\partial^2 v}{\partial x^2} + \frac{(1+\nu_p)}{2}\frac{\partial^2 u}{\partial x \partial y} = \frac{(1-\nu_p^2)\rho_p}{E_p}\frac{\partial^2 v}{\partial t^2}
\end{aligned} \tag{1}$$

where E_p is the Young's modulus, ρ_p is the material density and ν_p is the Poison's coefficient. The subscript p indicates the undamaged plate. The solution of both equations in Equation (1) is obtained by considering the vector $\mathbf{d}$ on the x-y plane which contains the plate, such that $\mathbf{d} = u\mathbf{i} + v\mathbf{j}$, which allows one to rewrite the equation of motion as follows (PARK *et al.*, 2001; YEO *et al.*, 2017)

$$\frac{(1-\nu_p)}{2}\nabla^2\mathbf{d} + \frac{(1+\nu_p)}{2}\nabla\nabla\bullet\mathbf{d} = \frac{(1-\nu_p^2)\rho_p}{E_p}\frac{\partial^2\mathbf{d}}{\partial t^2} \tag{2}$$

where **i** and **j** are unitary vectors in the x and y directions, respectively, $\bullet$ indicates the scalar product, $\nabla = \frac{\partial()\mathbf{i}}{\partial x} + \frac{\partial()\mathbf{j}}{\partial y}$ is the gradient operator and $\nabla^2 = \nabla\bullet\nabla$ is the Laplacian.

The solution vector **d** can be conveniently given by considering potential functions $\varphi(x,y,t)$ and $\boldsymbol{\psi}(x,y,t)$, such that (MIKLOWITZ, 1978)

$$\mathbf{d}(x,y,t) = \nabla\varphi(x,y,t) + \nabla\times\boldsymbol{\psi}(x,y,t) \tag{3}$$

where $\varphi(x,y,t)$ is a scalar function representing the potential linear displacement and $\boldsymbol{\psi}$ represents the potential angular displacement and normal to the plate plane, i.e., $\nabla\bullet\boldsymbol{\psi} = 0$ (PARK *et al.*, 2001). Substituting Equation (3) into (2), it is obtained:

$$\begin{gathered}\frac{(1-\nu_p)}{2}\nabla^2\left[\nabla\varphi + \nabla\times\boldsymbol{\psi}\right] + \frac{(1+\nu_p)}{2}\nabla(\nabla\bullet\left[\nabla\varphi + \nabla\times\boldsymbol{\psi}\right]) = \\ \frac{(1-\nu_p^2)\rho_p}{E_p}\frac{\partial^2}{\partial t^2}\left[\nabla\varphi + \nabla\times\boldsymbol{\psi}\right]\end{gathered} \tag{4}$$

where $\nabla\bullet\nabla\varphi = \nabla^2\varphi$ and $\nabla\bullet(\nabla\times\boldsymbol{\psi}) = 0$ (PARK *et al.*, 2001), which allows one to rewrite

$$\frac{(1-\nu_p)}{2}\nabla^2\left[\nabla\varphi + \nabla\times\boldsymbol{\psi}\right] + \frac{(1+\nu_p)}{2}\nabla(\nabla^2\varphi) = \frac{(1-\nu_p^2)\rho_p}{E_p}\frac{\partial^2}{\partial t^2}\left[\nabla\varphi + \nabla\times\boldsymbol{\psi}\right] \tag{5}$$

considering that $\nabla^2(\nabla\varphi) = \nabla(\nabla^2\varphi)$ and $\nabla^2(\nabla\times\boldsymbol{\psi}) = \nabla\times(\nabla^2\boldsymbol{\psi})$. In this case, it is possible to obtain $\frac{\partial^2}{\partial t^2}(\nabla\times\boldsymbol{\psi}) = \nabla\times(\frac{\partial^2}{\partial t^2}\boldsymbol{\psi})$ and $\frac{\partial^2}{\partial t^2}(\nabla\varphi) = \nabla(\frac{\partial^2}{\partial t^2}\varphi)$, which allows one to write Equation (5) in the following form

$$\begin{gathered}\frac{(1-\nu_p)}{2}\left[\nabla(\nabla^2\varphi) + \nabla\times(\nabla^2\boldsymbol{\psi})\right] + \frac{(1+\nu_p)}{2}\nabla(\nabla^2\varphi) = \\ \frac{(1-\nu_p^2)\rho_p}{E_p}\left[\nabla\left(\frac{\partial^2\varphi}{\partial t^2}\right) + \nabla\times\left(\frac{\partial^2\boldsymbol{\psi}}{\partial t^2}\right)\right].\end{gathered} \tag{6}$$

From this last equation, it is possible to obtain

$$\nabla\left(\nabla^2\varphi - \frac{(1-\nu_p^2)\rho_p}{E_p}\frac{\partial^2\varphi}{\partial t^2}\right) + \nabla\times\left(\frac{(1-\nu_p)}{2}\nabla^2\boldsymbol{\psi} - \frac{(1-\nu_p^2)\rho_p}{E_p}\frac{\partial^2\boldsymbol{\psi}}{\partial t^2}\right) = 0. \tag{7}$$

Equation (7) allows one to write $\nabla^2\varphi = \dfrac{1}{c_l^2}\dfrac{\partial^2\varphi}{\partial t^2}$ and $\nabla^2\boldsymbol{\psi} = \dfrac{1}{c_s^2}\dfrac{\partial^2\boldsymbol{\psi}}{\partial t^2}$, and they are respectively related to the longitudinal and the shear waves in the middle plane of the plate. Their respective phase velocities are $c_l = \sqrt{E_p/[\rho_p(1-\nu_p^2)]}$ and $c_s = \sqrt{G_p/\rho_p}$, where G_p is the shear modulus. The shear waves can be neglected, which allows one to introduce the following equation to compute the potential linear displacement (PARK *et al.*, 2001)

$$\varphi(x,y,\omega) = [B_1 e^{i(-k_1x-k_2y)} + B_2 e^{i(k_1x-k_2y)} + B_3 e^{i(k_1x+k_2y)} + B_4 e^{i(-k_1x+k_2y)}]e^{-i\omega t} \tag{8}$$

where B_1 to B_4 are potential function amplitudes, k_1 and k_2 are components of the longitudinal wavenumber respectively in the x and y directions, and $i^2 = -1$. They can be written such that $k_1 = k_l \cos\theta$ and $k_2 = k_l \sin\theta$ (GOLATO; DEMIRLI; SANTHANAM, 2014), where $k_l = \omega/c_l$ is the wavenumber and θ the angle between direction of wave propagation and the x axis. $k_{l(p)} \equiv k_l$ for the plate undamaged region and $k_{l(d)}$ for the damaged one.

Based on Equation (8) and considering that $u = \partial\varphi/\partial x$ e $v = \partial\varphi/\partial y$ (PARK *et al.*, 2001), the longitudinal displacements are given by

$$\begin{aligned} u(x,y,\omega) &= \cos\theta[A_{ru}e^{--} - A_{lu}e^{+-} - A_{ld}e^{++} + A_{rd}e^{-+}]e^{-i\omega t} \\ v(x,y,\omega) &= \sin\theta[A_{ru}e^{--} + A_{lu}e^{+-} - A_{ld}e^{++} - A_{rd}e^{-+}]e^{-i\omega t} \end{aligned} \tag{9}$$

where $e^{i(\pm k_1x \pm k_2y)} \equiv e^{\pm\pm}$ is used to simplify the notation, i.e., for an instance $e^{++} = e^{i(+k_1x+k_2y)}$. The wave amplitudes are $A_{ru} = -B_1ik_l$, $A_{lu} = -B_2ik_l$, $A_{ld} = -B_3ik_l$ and $A_{rd} = -B_4ik_l$, where subscripts r (*right*) and u (*up*) indicate positive directions of x and y axes, respectively. The subscripts l (*left*) and d (*down*) are related to the negative x and y directions, respectively, such as illustrated in Figure 1.

The line forces per unit of displacement in the x and y directions are N_x and N_y, respectively, and they are given by (GIURGIUTIU, 2014a; RADWAŃSKA *et al.*, 2017)

$$\begin{aligned} N_x &= \frac{E_p h_p}{1-\nu_p^2}\left(\frac{\partial u}{\partial x} + \nu_p \frac{\partial v}{\partial y}\right) \\ N_y &= \frac{E_p h_p}{1-\nu_p^2}\left(\nu_p\frac{\partial u}{\partial x} + \frac{\partial v}{\partial y}\right) \end{aligned} \tag{10}$$

where h_p is the plate thickness. Substituting Equation (9) into Equation (10), it is possible to write

$$\begin{aligned} N_x &= \frac{E_p h_p}{1-\nu_p^2}\left[A_{ru}Le^{--} + A_{lu}Le^{+-} + A_{ld}Le^{++} + A_{rd}Le^{-+}\right]e^{-i\omega t} \\ N_y &= \frac{E_p h_p}{1-\nu_p^2}\left[A_{ru}\bar{L}e^{--} + A_{lu}\bar{L}e^{+-} + A_{ld}\bar{L}e^{++} + A_{rd}\bar{L}e^{-+}\right]e^{-i\omega t} \end{aligned} \tag{11}$$

Figure 1 – Longitudinal waves propagating from a point o on the plate, where $A_{(.)}$ is the wave amplitude and the subscripts r, l, u and d indicate respectively right, left, up and down. The angle θ indicates the direction of propagation in relation to the x axis. Point o indicates the coordinate system origin.

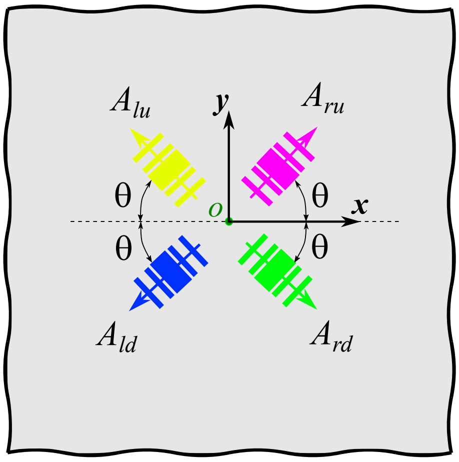

Source: elaborated by the author.

where $L = -i(k_1 \cos\theta + \nu_p k_2 \sin\theta)$ and $\bar{L} = -i(\nu_p k_1 \cos\theta + k_2 \sin\theta)$. Based on Equations (9) and (11), the state vector $\bar{\mathbf{h}} = \{u \;\; v \;\; N_x \;\; N_y\}^T$ is defined. Brennan (1994) noted that is convenient to introduce the transformation matrix $\bar{\mathbf{H}}$, the spatial transformation matrix $\bar{\mathbf{T}}$ and the vector of wave amplitudes $\bar{\mathbf{a}}$ to rewrite a state-vector notation such that

$$\bar{\mathbf{h}}(x, y, \theta, \omega) = \bar{\mathbf{H}}(\theta, \omega)\bar{\mathbf{T}}(x, y, \omega)\bar{\mathbf{a}}(\omega). \tag{12}$$

Note that the dependency of x, y, θ and ω indicated in Equation (12) is omitted in this chapter by simplicity. Although Brennan (1994) has investigated one dimensional structures, the equations for the plate considered herein can be similarly rearranged, and the following matrices and vector can be defined

$$\bar{\mathbf{H}} = \begin{bmatrix} \cos\theta & -\cos\theta & -\cos\theta & \cos\theta \\ \sin\theta & \sin\theta & -\sin\theta & -\sin\theta \\ \dfrac{E_p h_p L}{(1-\nu_p^2)} & \dfrac{E_p h_p L}{(1-\nu_p^2)} & \dfrac{E_p h_p L}{(1-\nu_p^2)} & \dfrac{E_p h_p L}{(1-\nu_p^2)} \\ \dfrac{E_p h_p \bar{L}}{(1-\nu_p^2)} & \dfrac{E_p h_p \bar{L}}{(1-\nu_p^2)} & \dfrac{E_p h_p \bar{L}}{(1-\nu_p^2)} & \dfrac{E_p h_p \bar{L}}{(1-\nu_p^2)} \end{bmatrix} \tag{13}$$

$$\bar{\mathbf{T}} = diag\left(\; e^{i(-k_1 x - k_2 y)}, e^{i(k_1 x - k_2 y)}, e^{i(k_1 x + k_2 y)}, e^{i(-k_1 x + k_2 y)} \; \right) \tag{14}$$

$$\bar{\mathbf{a}} = \left\{ \begin{array}{cccc} A_{ru} & A_{lu} & A_{ld} & A_{rd} \end{array} \right\}^T \tag{15}$$

where $diag(\ )$ indicates a diagonal matrix.

2.2 CROSS-SECTION CHANGE ANALYSIS

This section presents an investigation on the longitudinal wave propagation considering a cross-section change, as shown in Figure 2. The idea is to determine the coefficients to express transmitted and reflected waves in relation to the incident wave. These coefficients are written in terms of the physical and geometric properties of the plate.

Figure 2 – Plate with cross-section change in the y direction. C represents an actuator responsible by the generation of a longitudinal wave that propagates in the x and y positive directions. S_l and S_r are the sensors responsible by the acquisition of reflected and transmitted waves.

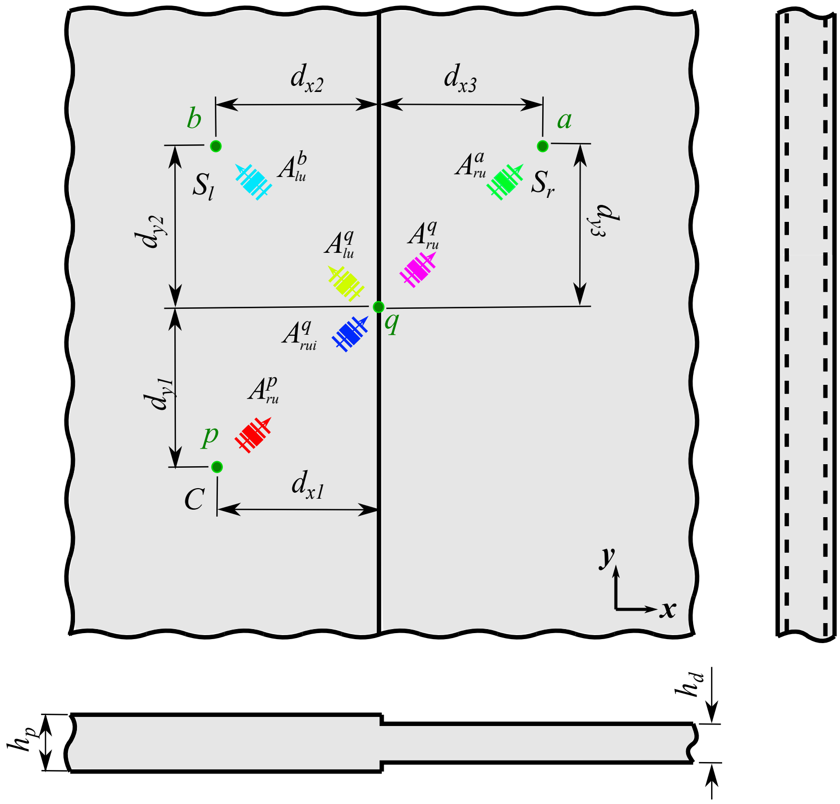

Source: elaborated by the author.

Considering an actuator at the point p shown in Figure 2. Assume that it can generate a longitudinal wave that propagates simultaneously in the x and y positive directions with an angle θ between its direction and the x axis. At the points a and b are considered two sensors S_r and S_l to obtain the transmitted and reflected waves, respectively. Equation (9) is rewritten as shown below:

$$\begin{aligned} u(x,y,\omega) &= \cos\theta[A_{ru}e^{--} - A_{lu}e^{+-}]e^{-i\omega t} \\ v(x,y,\omega) &= \sin\theta[A_{ru}e^{--} + A_{lu}e^{+-}]e^{-i\omega t}. \end{aligned} \tag{16}$$

Substituting Equation (16) in Equation (10), it is possible to obtain the line forces N_x and N_y as follows:

$$\begin{aligned} N_x &= \frac{E_p h_p}{1-\nu_p^2}\left[-A_{ru}ik_{l(p)}(\cos^2\theta + \nu_p\sin^2\theta)e^{--} - A_{lu}ik_{l(p)}(\cos^2\theta + \nu_p\sin^2\theta)e^{+-}\right]e^{-i\omega t} \\ N_y &= \frac{E_p h_p}{1-\nu_p^2}\left[-A_{ru}ik_{l(p)}(\nu_p\cos^2\theta + \sin^2\theta)e^{--} - A_{lu}ik_{l(p)}(\nu_p\cos^2\theta + \sin^2\theta)e^{+-}\right]e^{-i\omega t}. \end{aligned} \tag{17}$$

The line force N_x is rewritten such that

$$\left[A_{ru}e^{--} + A_{lu}e^{+-}\right]e^{-i\omega t} = -N_x\frac{(1-\nu_p^2)}{E_p h_p}\frac{1}{ik(\cos^2\theta + \nu_p\sin^2\theta)} \tag{18}$$

which allows one to write N_y and v in terms of N_x. Then,

$$v(x,y,\omega) = -N_x\frac{(1-\nu_p^2)}{E_p h_p}\frac{\sin\theta}{ik(\cos^2\theta + \nu_p\sin^2\theta)} \tag{19}$$

$$N_y(x,y,\omega) = N_x\frac{(\nu_p\cos^2\theta + \sin^2\theta)}{(\cos^2\theta + \nu_p\sin^2\theta)}. \tag{20}$$

Note that N_y and v are written in terms of N_x, which allows one to consider u and N_x to define the state vector $\bar{\mathbf{h}}(x,y,\omega) = \{u \quad N_x\}^T = \bar{\mathbf{H}}(\omega)\bar{\mathbf{T}}(x,y,\omega)\bar{\mathbf{a}}(\omega)$. In this case,

$$\bar{\mathbf{H}}(\omega) = \begin{bmatrix} \cos\theta & -\cos\theta \\ \dfrac{-ik_{l(p)}E_p h_p(\cos^2\theta + \nu_p\sin^2\theta)}{1-\nu_p^2} & \dfrac{-ik_{l(p)}E_p h_p(\cos^2\theta + \nu_p\sin^2\theta)}{1-\nu_p^2} \end{bmatrix} \tag{21}$$

$$\bar{\mathbf{T}}(x,y,\omega) = diag\left(e^{ik_{l(p)}(-x\cos\theta - y\sin\theta)}, e^{ik_{l(p)}(x\cos\theta - y\sin\theta)}\right) \tag{22}$$

$$\bar{\mathbf{a}}(\omega) = \{A_{ru} \quad A_{lu}\}^T. \tag{23}$$

Considering the point q in Figure 2, it is possible to write $A_{ru} \equiv A^q_{rui}$ and $A_{lu} \equiv A^q_{lu}$ for section with thickness h_p. On the other hand, $A_{ru} \equiv A^q_{ru}$ for section with thickness h_d. In this case $\bar{\mathbf{h}}_p = \bar{\mathbf{H}}_p \bar{\mathbf{a}}^q_p$, where $\bar{\mathbf{a}}^q_p = \{A^q_{rui} \;\; A^q_{lu}\}^T$ (at the point q). Similarly, $\bar{\mathbf{h}}_d = \bar{\mathbf{H}}_d \bar{\mathbf{a}}^q_d$ for $\bar{\mathbf{a}}^q_d = \{A^q_{ru} \;\; 0\}^T$. The subscripts indicate the corresponding section, i.e., d for section with thickness h_d; and p for section with thickness h_p. The superscripts indicate the evaluated point (see Figure 2). Considering $\bar{\mathbf{h}}_p = \bar{\mathbf{h}}_d$, it is obtained $\bar{\mathbf{a}}_p = \mathbf{Z}\bar{\mathbf{a}}_d$, where $\mathbf{Z} = [\bar{\mathbf{H}}_p]^{-1}\bar{\mathbf{H}}_d$. Then, the amplitudes A^q_{lu} and A^q_{ru} can be written in terms of the incident amplitude A^q_{rui}, as follows:

$$\frac{A^q_{ru}}{A^q_{rui}} = \frac{2}{1 + \bar{H}h\hat{P}} \quad \text{for } 0 \leq \theta \leq 60^o, \tag{24}$$

$$\frac{A^q_{lu}}{A^q_{rui}} = \frac{\bar{H}\hat{P} - 1}{1 + \bar{H}h\hat{P}} \quad \text{for } 0 \leq \theta \leq 60^o, \tag{25}$$

where $\bar{H} = \sqrt{(E_{dp}\rho_{dp})/\check{\nu}}$ ($E_{dp} = E_d/E_p$, $\rho_{dp} = \rho_d/\rho_p$), $h = h_d/h_p$, $\check{\nu} = (\hat{\nu_d}/\hat{\nu_p})$, $\hat{\nu_p} = (\nu_p^2 - 1)$ and $\hat{\nu_d} = (\nu_d^2 - 1)$. $\hat{P} = (P_d/P_p)$. $P_d = (\nu_d \sin^2\theta + \cos^2\theta)$ and $P_p = (\nu_p \sin^2\theta + \cos^2\theta)$. In addition, if the sections of thicknesses h_p and h_d have different physical properties, the propagation angle of the transmitted wave is different from the angles of the incident and reflected waves (which are the same) due to differences in their velocities. For this case, it is necessary to take into account the Snell-Descartes' law to compute the propagation angle of the transmitted wave.

Let $C_{t(pd)}$ be the coefficient defined by ratio between the amplitudes of the transmitted and incident longitudinal waves, and $C_{r(pd)}$ for the reflected wave, it is possible to write the following equations

$$C_{t(pd)} = \frac{2}{1 + h} \tag{26}$$

$$C_{r(pd)} = \frac{h - 1}{1 + h} \tag{27}$$

for $0 \leq \theta \leq 60^o$. If $h_p < h_d$, then,

$$C_{t(dp)} = hC_{t(pd)} = \frac{2h}{1 + h} \tag{28}$$

$$C_{r(dp)} = -C_{r(pd)} = \frac{1 - h}{1 + h}. \tag{29}$$

Equations (26) to (29) can be used to determine the relations between the wave amplitudes considering symmetrical cross-section change, and consequently, there is no conversion of modes due to symmetry of the cross-section change (PAU; ACHILLOPOULOU, 2017; PODDAR; GIURGIUTIU, 2016; LOPES *et al.*, 2022).

2.3 LONGITUDINAL WAVE SCATTERING IN THIN PLATES WITH SYMMETRICAL DAMAGE

Local thickness reduction has been successfully used to represent structural damage, as presented in references Lowe *et al.* (2002), Lowe and Diligent (2002), Glushkov *et al.* (2015), Gonsalez-Bueno (2019) and others. This approach was previously introduced by Shen and Pierre (1990) to describe symmetric cracks and this type of damage representation has been often considered in the literature to investigate the interactions between damage and wave propagation (PAU; ACHILLOPOULOU; VESTRONI, 2016). In particular for the plate, it is possible to include a damage with width $l_x << L_x$ and length $L_{y(d)} < L_y$ in the x and y directions, respectively, where L_x and L_y are the dimensions of the plate in the x and y directions. See a schematic illustration in Figure 3. Note that it is assumed $l_x << L_{y(d)}$ as discussed in the following sections.

2.3.1 Wave Scattering due to Oblique Incident Wave Propagating in the x and y Positive Directions

Figure 3 shows a thin plate with thickness h_p. The plate exhibits damage with physical properties equal to the undamaged section. However, it is characterized by thickness $h_d < h_p$. The point p represents the position of an actuator used for generating a longitudinal wave that propagates in the x and y positive directions with the angle θ in relation to the positive x axis, i.e., the wave is generated at the point p and propagates until the point q. Due to the damage presence, the incident wave is divided into transmitted (from point q to r) and reflected (from point q to e) waves. Health and damaged regions of the plate have the same physical properties, then, the velocities of the waves are the same in both regions and the propagation angle of the transmitted wave packet inside the damage is also θ. If the damage has different properties from the healthy region of the plate, it is necessary to take into account the Snell-Descartes' law to compute the propagation angle of the transmitted wave packet (see Section 2.2). In addition, this approach is applied for low-frequency range. The point a indicates the position of a circular sensor with radius r_R (subscript R indicates right-hand side of the plate). The first reflected wave packet is received at the point e, where encounters another circular sensor with radius r_L (subscript L indicates left-hand side of the plate).

Figure 3 – Thin plate with symmetrical damage of the width l_x in the x axis and length $L_{y(d)}$ ($L_{y(d)} < L_y$) in the y axis. L_x and L_y are the dimensions of the plate in the x and y directions, respectively. Point p represents the location of an actuator generating a longitudinal wave propagating from the point p to q. Circular sensors are considered at the points e and a, with radii r_L and r_R. Points a and e correspond to the first packets of transmitted and reflected waves, respectively.

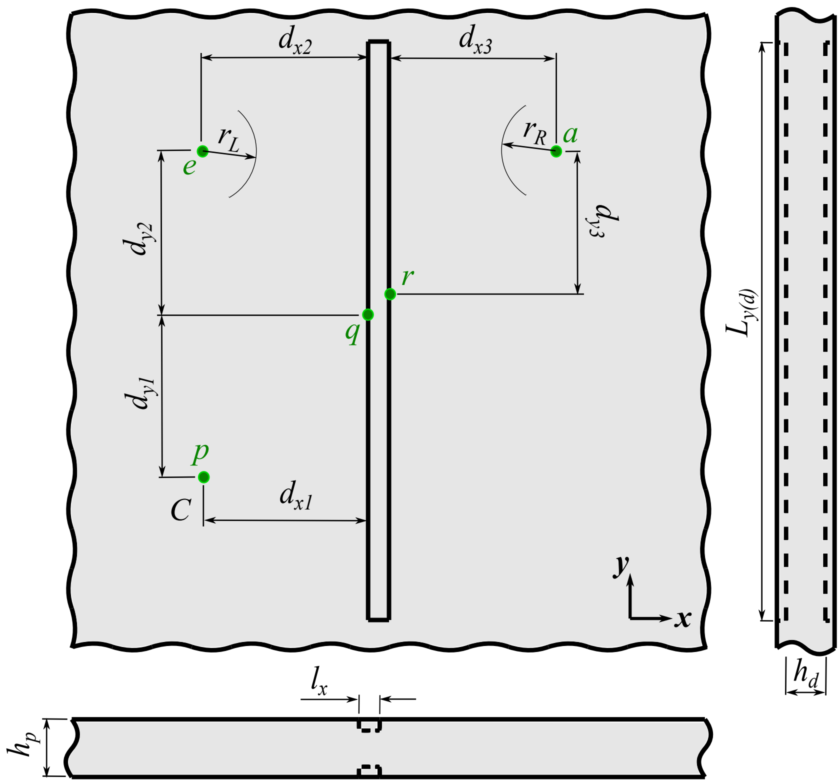

Source: elaborated by the author.

The wave transmitted from the point q is incident at point r. The wave generated at the point r propagates until the point s shown in Figure 4. From the point s, the second reflected wave packet propagates to the left-hand side of the plate until the point f. Similarly, the wave propagates from the point s to the right-hand side of the plate, until the point t. The second transmitted wave packet propagates from t until the point b. This process occurs continuously over time, and the third reflected wave packet arrives at the point g and the third transmitted wave packet arrives at the point c.

Considering a longitudinal wave from point p to point q, it is possible to write that the first reflected wave packet incoming at the point e is equal to $\frac{A_r^e}{A_i^p} = \frac{A_r^e}{A_r^q}\frac{A_r^q}{A_i^q}\frac{A_i^q}{A_i^p}$, where $A_r^{()}$ and $A_i^{()}$ are the reflected and incident wave amplitudes at the point ( ). A_r^q/A_i^q is the ratio between the reflected and incident wave amplitudes due to the cross-sectional change at the point q. Then, it is possible to write $A_r^q/A_i^q = C_{r(pd)}$, where $C_{r(pd)}$ is given by Equation (27) (see Section 2.2 for details). The ratio of amplitudes A_r^e/A_r^q and A_i^q/A_i^p are obtained using the spatial transformation matrix, as such $A_i^q/A_i^p = T_1^p$ and

Figure 4 – Thin plate with symmetrical damage of the width l_x in the x axis and length $L_{y(d)}$ ($L_{y(d)} < L_y$) in the y axis. Point p represents the location of an actuator generating a longitudinal wave propagating from the point p to q. Circular sensors are considered at the points e and a, with radii r_L and r_R. Points a and e correspond to the first packets of transmitted and reflected waves, respectively. The points a, b and c capture the transmitted wave packets, while points e, f and g capture the reflected wave packets.

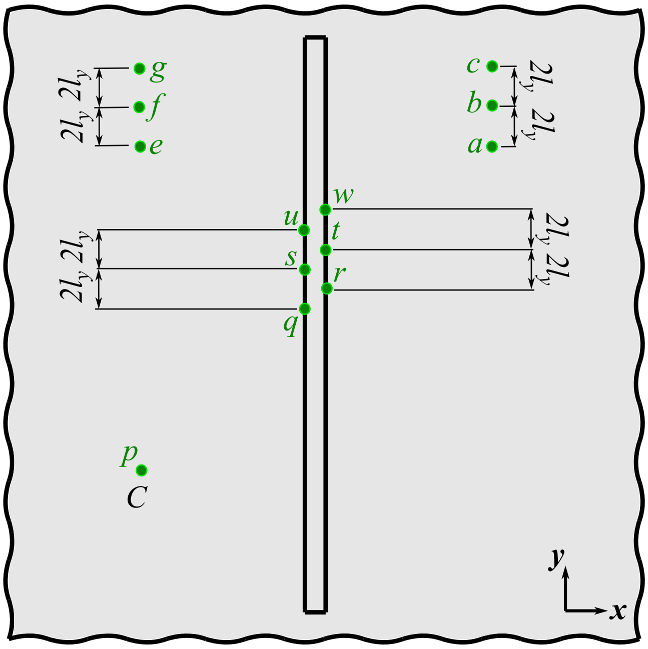

Source: elaborated by the author.

$A^e_r/A^p_i = T^p_2$, where $T^p_1 = e^{ik_{l(p)}(-d_{x1}\cos\theta - d_{y1}\sin\theta)}$ and $T^p_2 = e^{ik_{l(p)}(+(-d_{x2})\cos\theta - d_{y2}\sin\theta)}$. $k_{l(p)}$ is computed for the undamaged section properties of the plate. In this case, $\frac{A^e_r}{A^p_i} = T^p_1 T^p_2 C_{r(pd)}$, and considering $d_{x1} = d_{x2}$ e $d_{y1} = d_{y2}$, it is possible to obtain

$$\frac{A^e_r}{A^p_i} = \frac{(h-1)}{(h+1)} e^{-2ik_{l(p)}d_{x1}\sec\theta} \tag{30}$$

where $h = h_d/h_p$ and $\sec\theta = (1/\cos\theta)$. The amplitude ratio A^a_t/A^p_i at the point a can be written in terms of the generated wave by the actuator at the point p, such that $\frac{A^a_t}{A^p_i} = \frac{A^a_t}{A^r_t}\frac{A^r_t}{A^r_i}\frac{A^r_i}{A^q_t}\frac{A^q_t}{A^q_i}\frac{A^q_i}{A^p_i}$. In particular, $\frac{A^r_t}{A^r_i} = C_{t(dp)}$ (Equation 28) and $\frac{A^q_t}{A^q_i} = C_{t(pd)}$ because they correspond to the amplitudes resulting from the interaction between wave and cross-sectional change, respectively, at the points q and r. In addition, the amplitudes $\frac{A^a_t}{A^r_t}$ and $\frac{A^r_i}{A^q_t}$ can be obtained using the transformation matrix, such that $A^a_t/A^r_t = T^p_1$ (if $d_{x1} = d_{x3}$ and $d_{y1} = d_{y3}$) and $A^r_i/A^q_t = T^d_1$, in which $T^d_1 = e^{ik_{l(d)}(-l_x\cos\theta - l_y\sin\theta)}$. $k_{l(d)} \equiv k_{l(p)}$ because the damaged and undamaged sections both have equal physical properties. Also, note that $l_y = l_x\tan\theta$. Thus, it is possible to obtain $\frac{A^a_t}{A^p_i} = (T^p_1)^2 T^d_1 C_{t(pd)} C_{t(dp)}$, which allows one to write the following equation

$$\frac{A_t^a}{A_i^p} = \frac{4h}{(h+1)^2} e^{-2ik_{l(p)}d_{x1}\sec\theta} e^{-ik_{l(d)}l_x\sec\theta}. \tag{31}$$

The approach described above can be repeated to obtain the second and third wave packets. In this case, it is possible to write for the point f $\frac{A_r^f}{A_i^p} = \frac{A_r^f}{A_t^s}\frac{A_t^s}{A_i^s}\frac{A_i^s}{A_r^r}\frac{A_r^r}{A_i^r}\frac{A_i^r}{A_t^q}\frac{A_t^q}{A_i^q}\frac{A_i^q}{A_i^p}$, which describes the second reflected wave packet, where $\frac{A_r^r}{A_i^r} = C_{r(dp)}$, $\frac{A_t^s}{A_i^s} = C_{t(dp)}$ and $\frac{A_i^s}{A_r^r} = T_2^d$, considering that $T_2^d = e^{ik_{l(d)}(+(-l_x)\cos\theta - l_y\sin\theta)}$. This ratio is written by $\frac{A_r^f}{A_i^p} = T_1^pT_2^pT_1^dT_2^dC_{t(pd)}C_{r(dp)}C_{t(dp)}$, and the following equation is obtained

$$\frac{A_r^f}{A_i^p} = -\frac{4h\,(h-1)}{(h+1)^3} e^{-2ik_{l(p)}d_{x1}\sec\theta} e^{-2ik_{l(d)}l_x\sec\theta}. \tag{32}$$

Similarly, the amplitude ratio at the point g is $\frac{A_r^g}{A_i^p} = T_1^pT_2^p(T_1^dT_2^d)^2C_{t(pd)}(C_{r(dp)})^3C_{t(dp)}$, which can be rewritten as follows

$$\frac{A_r^g}{A_i^p} = -\frac{4h\,(h-1)^3}{(h+1)^5} e^{-2ik_{l(p)}d_{x1}\sec\theta} e^{-4ik_{l(d)}l_x\sec\theta}. \tag{33}$$

The second and third transmitted wave packets are obtained using similar approach. For the points b and c, it is possible to write $\frac{A_t^b}{A_i^p} = (T_1^p)^2(T_1^d)^2T_2^dC_{t(pd)}(C_{r(dp)})^2C_{t(dp)}$ and $\frac{A_t^c}{A_i^p} = (T_1^p)^2(T_1^d)^3(T_2^d)^2C_{t(pd)}(C_{r(dp)})^4C_{t(dp)}$, such that

$$\frac{A_t^b}{A_i^p} = \frac{4h\,(h-1)^2}{(h+1)^4} e^{-2ik_{l(p)}d_{x1}\sec\theta} e^{-3ik_{l(d)}l_x\sec\theta} \tag{34}$$

$$\frac{A_t^c}{A_i^p} = \frac{4h\,(h-1)^4}{(h+1)^6} e^{-2ik_{l(p)}d_{x1}\sec\theta} e^{-5ik_{l(d)}l_x\sec\theta}. \tag{35}$$

Based on the modeling introduced in this present chapter, it is possible to compute the first reflected and transmitted wave packets (i.e., incoming respectively at the points e and a) using the following equations:

$$\left.\frac{A_r}{A_i}\right|_{(1)} = \frac{(h-1)}{(h+1)} e^{-2ik_{l(p)}d_{x1}\sec\theta} \tag{36}$$

$$\left.\frac{A_t}{A_i}\right|_{(1)} = \frac{4h}{(h+1)^2} e^{-2id_{x1}k_{l(p)}\sec\theta} e^{-ik_{l(d)}l_x\sec\theta}. \tag{37}$$

The other packets of reflected and transmitted waves can also be defined respectively by the following equations

$$\left.\frac{A_r}{A_i}\right|_{(n)} = -\frac{4h(h-1)^{(2n-3)}}{(h+1)^{(2n-1)}} e^{-2id_{x1}k_{l(p)}\sec\theta} e^{-2(n-1)il_x k_{l(d)}\sec\theta} \tag{38}$$

$$\left.\frac{A_t}{A_i}\right|_{(n)} = \frac{4h(h-1)^{2(n-1)}}{(h+1)^{2n}} e^{-2id_{x1}k_{l(p)}\sec\theta} e^{-(2n-1)ik_{l(d)}l_x\sec\theta} \tag{39}$$

where $n = 2,\ 3,\ 4, \ldots$.

2.3.2 Resulting Wave due to Circular Longitudinal Wave Propagation

According to Raghavan and Cesnik (2005), the use of circular actuators in plates generates propagation of radial waves with the same wave amplitude in all directions. Figure 5 presents a thin plate with a circular actuator placed at the point p which creates radial longitudinal waves with amplitude A_i, as presented by Shen and Giurgiutiu (2016). A circular sensor with radius r_R is considered at the point a, and it captures the wave front created by the actuator for an angle range that depends on its size. The direction between the actuator and sensor centers is indicated by a solid line, with an angle θ_1 in relation to the x axis. The corresponding angle (see two dotted lines) is used to compute the sensor output voltage (YEUM; SOHN; IHN, 2011). Figure 6 shows the plate with symmetric damage of length l_x in the x direction. $A_r|_{()}^{\theta_1}$ and $A_t|_{()}^{\theta_1}$ represent respectively amplitudes for the reflected and transmitted waves, in which the subscript indicates the wave packet number. If the sensors radii are smaller than $2l_x\tan(\theta_1)$, these transducers capture just the first wave packet.

Figure 5 – Thin plate with a circular actuator placed at the point p to create radial waves with amplitude A_i. A circular sensor at the point a captures the wave front for an angle range around the angle θ_1.

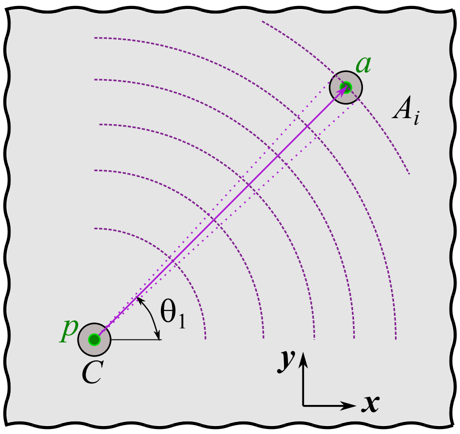

Source: elaborated by the author.

Figure 6 – Thin plate with symmetric damage of length l_x in the x axis. Points a and b indicate the first and second packets of amplitudes $A_t|_1^{\theta_1}$ and $A_t|_2^{\theta_1}$, and points e and f indicate the first two reflected wave packets with amplitudes $A_r|_1^{\theta_1}$ and $A_r|_2^{\theta_1}$, respectively.

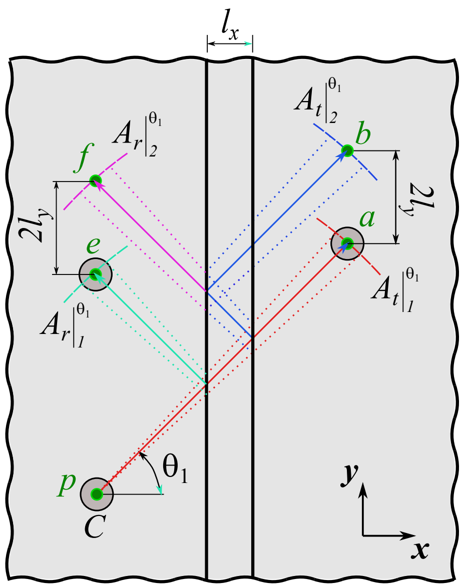

Source: elaborated by the author.

Considering that the circular actuator C generates radial waves in all directions, the first transmitted wave packet associated to the θ_1 direction achieves the sensor at point a. The second wave packet associated to an angle θ_2 also achieves the same sensor. Figure 7 illustrates the path of both wave packets, with amplitudes $A_t|_1^{\theta_1}$ and $A_t|_2^{\theta_2}$, for $\theta_2 < \theta_1$. Due to their small amplitudes, other wave packets (such as the third, fourth, etc) can be neglected (see Figure 10 to clarify). Then, assuming sensor sizes such as $r_{()} < 2l_x \tan(\theta_1)$, the resulting wave ($\frac{A_t}{A_i}\big|_c$) captured by the sensor at the point a can be accurately described by sum of the first and second packets, respectively associated to the angles θ_1 and θ_2. Note that the subscript c indicates the circular actuator. The wave amplitude for the first packet propagating in θ_1 is computed by Equation (37). In addition, the second wave packet propagating in θ_2 is computed by Equation (39) (for $n = 2$). Note that the angles θ_1 and θ_2 are determined from the relative positions between actuator and sensor. The resulting wave is accurately obtained by the following equation:

$$\left.\frac{A_t}{A_i}\right|_c \approx \left.\frac{A_t}{A_i}\right|_1^{\theta_1} + \left.\frac{A_t}{A_i}\right|_2^{\theta_2}. \tag{40}$$

Figure 7 – Plate with symmetric damage of length l_x in the x direction. Point a indicates the sensor capturing the first wave packet $(\bar{A}_t|_1^{\theta_1})$ for θ_1 and the second wave packet $(\bar{A}_t|_2^{\theta_2})$ for θ_2.

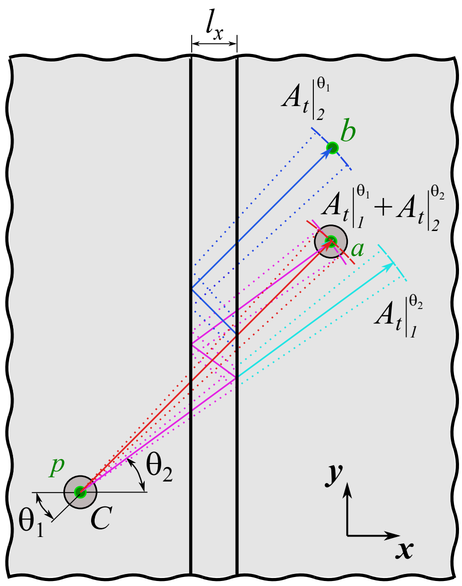

Source: elaborated by the author.

2.3.3 Detecting the Thickness Reduction in a Damaged Section

According to Glushkov *et al.* (2015), the energy of a longitudinal wave is proportional to the square of its absolute value. Considering the ratio between reflected and incident waves, or transmitted and incident, it is possible to write the relative energy of the reflected wave by

$$E_r = \left|\frac{A_r}{A_i}\right|^2 \tag{41}$$

and for the transmitted wave

$$E_t = \left|\frac{A_t}{A_i}\right|^2 . \tag{42}$$

Considering a circular sensor with radius $r_{(\,)} < 2l_y$, i.e., $r_{(\,)} < 2l_x \tan\theta$, placed at the points a and e, both sensors measure the first wave packets separately from the other ones. Comparing Equations (41) and (42) with Equations (36) and (37), the relative energy related to the measured reflected and transmitted wave packets in these sensors corresponds to the following equations

$$E_r \equiv E_r|_{(1)} = \frac{(1-h)^2}{(h+1)^2} \quad \text{and} \quad E_t \equiv E_t|_{(1)} = \frac{16h^2}{(h+1)^4}. \tag{43}$$

Based on these equations, the thickness of the plate in the damaged section can be determined by using the following equation:

$$h_d = \frac{1 - \sqrt{E_r|_{(1)}}}{1 + \sqrt{E_r|_{(1)}}} h_p, \tag{44}$$

which provides accurate estimates of h_d. Note that it is possible to write $h_d = h_p \left(1 - \sqrt{1 - E_t|_{(1)}}\right)^2 / \sqrt{E_t|_{(1)}}$. However, this last equation is mathematically limited to be applied for large damage depth (i.e., $1 - h > 20\%$), otherwise $E_t|_{(1)} > 1$, and a complex number is obtained from the term with the square root, and this equation must be neglected.

2.3.4 Index for Damage Detection in Plates using Transmitted Longitudinal Wave

The presence of a damage changes the transmitted wave amplitude at the frequency of excitation, which allows one to establish the damage detection index $\bar{R}$ defined by the ratio between the maximum magnitudes obtained for an unknown structural condition ($max(|A_u|)$, Figure 8, symbol $\triangledown$) and for the healthy plate ($max(|A_k|)$, Figure 8, symbol $\square$). Then, the index $\bar{R} = \frac{max(|A_u|)}{max(|A_k|)}$ is proposed, which implies to the theoretical value $\bar{R} = 1$ if the unknown condition corresponds to the undamaged structure. In particular, a five cycles tone burst is employed as input signal, and the output amplitudes are obtained from the magnitude in the frequency domain at the frequency of excitation (see an illustrative example in Fig. 8). In a practical case, it is interesting to consider more than one signal for characterizing the healthy structure, and one of them is used as reference. The damage index $\bar{R}$ can be computed considering the other signals, which allows one to establish a range $[\bar{R}_l, 1]$ for describing the healthy structure. Then, the minimum value of $\bar{R}$ for the healthy condition is denoted by $\bar{R}_l$, such that a damage is detected for an unknown structural condition if a computed damage index is $\bar{R} < \bar{R}_l$. Note that $\bar{R}_l$ establishes a threshold for the damage detection.

Figure 8 – Magnitude of the transmitted tone burst with 5 cycles at the frequency 100 kHz. Continuous line is obtained for healthy structure and the dashed line for the unhealthy one. Symbols □ and ▽ are the maximum values obtained for each case, respectively.

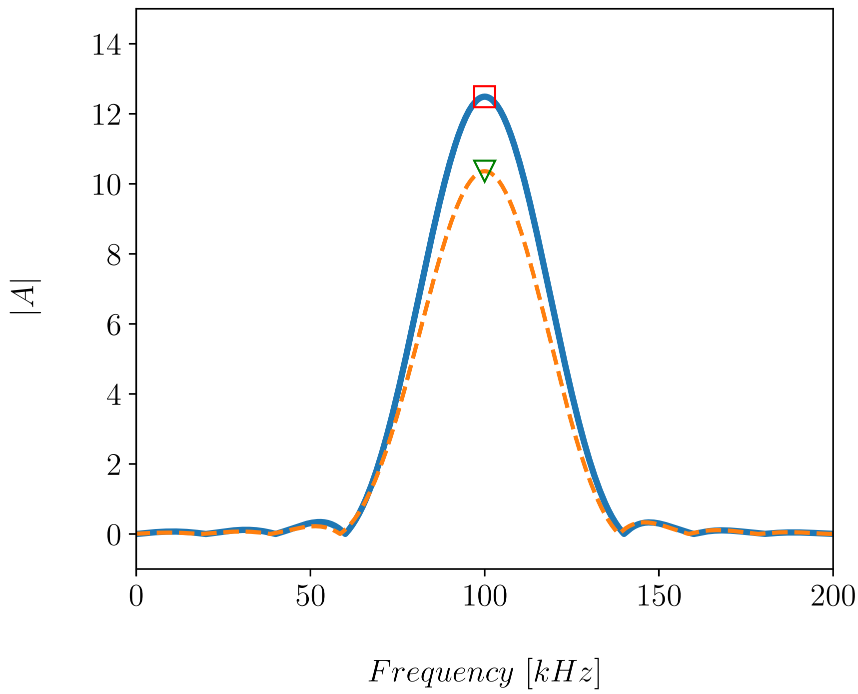

Source: elaborated by the author.

2.4 RESULTS AND DISCUSSION

This section presents numerical results to demonstrate the proposed approach to detect damage in an aluminum plate with $L_x = L_y = 50$ cm, $E_p = 69$ MPa, $\rho_p = 2710$ kg.m^{-3}, $h_p = 1.5$ mm, $l_x = 5$ mm, $d_{x1} = d_{x2} = d_{x3} = 10$ cm and $\nu_p = 0.31$. The longitudinal wave is generated from the point p, with oblique incidence in a damaged section. The physical properties of the damaged section are equal to the undamaged section, but with reduced thickness $h_d < h_p$.

Reflected ($|A_r/A_i|_{(n)}$) and transmitted ($|A_t/A_i|_{(n)}$) wave amplitude ratios are constants over both frequency and incidence angle, and they depend on the ratio $h = h_d/h_p$. Figures 9 and 10 show the four first wave packets of these amplitudes in terms of the damage depth $(1 - h)$. Based on Figure 9, it is noted that if $(1 - h) < 30\%$ the two first reflected wave packets present higher amplitudes in comparison with the other packets. These results indicate that if a circular sensor with radius $r_L < 2l_x \tan(\theta)$ is placed on the plate at the point e, it can measure the first packet and the measurement contains important amount of energy once it is proportional to the square of the wave amplitude.

In addition, the sensor can measure the first wave separately from the other packets, which is interesting to damage detection, as discussed herein.

Figure 9 – Reflected wave amplitude ratios ($|A_r/A_i|_{(n)}$) in terms of the damage depth $(1-h)$: first packet ($n=1$, dashed line), second ($n=2$, continuous line), third ($n=3$, dotted line) and fourth packets ($n=4$, dash-dotted line).

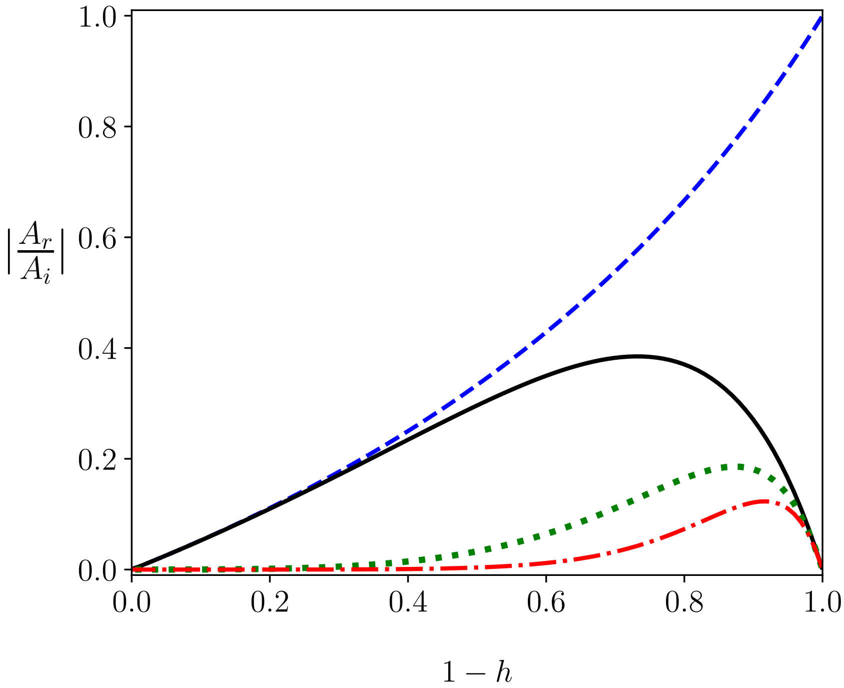

Source: elaborated by the author.

Figure 10 shows that the first transmitted wave packet is higher than the other packets. However, $|\frac{A_t}{A_i}|$ is almost equal to 1 for low damage depth (i.e., small value of $(1-h)$). In practice, this means that the transmitted wave amplitude for small $(1-h)$ is approximately equal to the amplitude of the wave generated by the actuator, which becomes difficult to detect the damage presence by comparing them.

Figure 11 shows that two different sizes of circular sensors r_L obtain amplitudes of reflected waves approximately equal to each other. Sensor sizes between the ranges $2l_x\tan(\theta) \leq r_L < 4l_x\tan(\theta)$ and $4l_x\tan(\theta) \leq r_L < 6l_x\tan(\theta)$ are compared. The incoming wave for the sensor size $2l_x\tan(\theta) \leq r_L < 4l_x\tan(\theta)$ corresponds to the first and second wave packets, whereas the three first wave packets are obtained if $4l_x\tan(\theta) \leq r_L < 6l_x\tan(\theta)$. However, there is a small contribution from the third and fourth wave packets, as shown in Figure 9. This characteristic is also verified for the transmitted wave, as shown in Figure 12. Based on these results, it is not necessary to consider a sensor with radius larger than $4l_x\tan(\theta)$. Note that the maximum wave amplitude ratios occur at

Figure 10 – Transmitted wave amplitude ratios ($|A_t/A_i|_{(n)}$) in terms of the damage depth $(1-h)$: first packet ($n = 1$, dashed line), second ($n = 2$, continuous line), third ($n = 3$, dotted line) and fourth packets ($n = 4$, dash-dotted line).

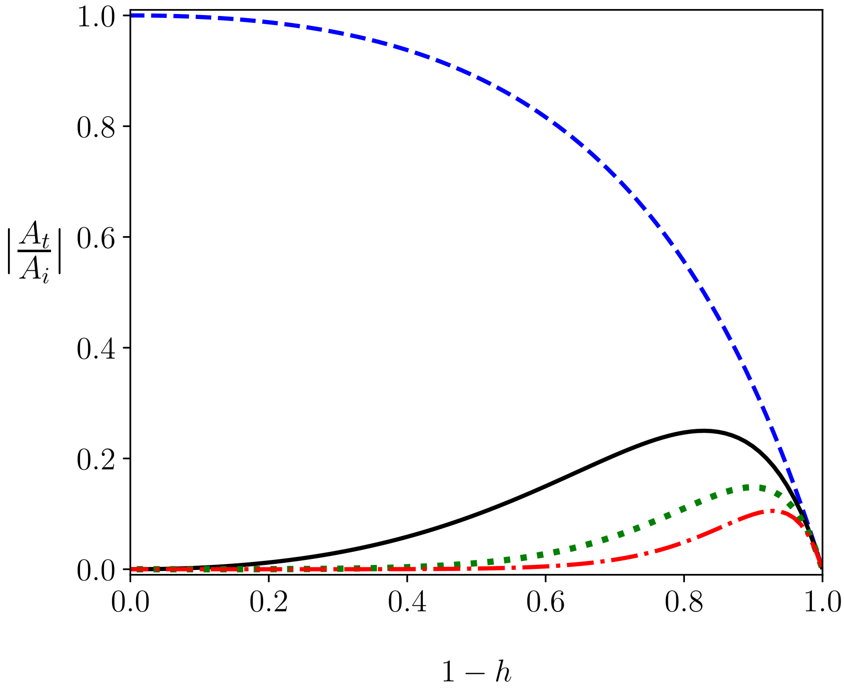

Source: elaborated by the author.

specific optimum frequencies $f^l_{opt} = \frac{(1+m)}{4l_x}\cos(\theta)\sqrt{E_d/[\rho_d(1-\nu_d^2)]}$, where $m = 0,\ 2,\ 4,...,$ which also depends on the angle of incidence θ. The optimal frequencies for symmetric damage are slightly different from those obtained for asymmetric damage, for which wave mode conversion is observed. The difference between these cases increases according to the damage asymmetry, as presented by Lopes *et al.* (2022) and Gonsalez-Bueno (2019). Therefore, it is important to know these frequencies for the symmetric case, which can correspond with good accuracy to the optimal frequencies for the asymmetric case, mainly when considering small damage. Note that it is useful to consider this result to define the SHM process, which allows one to establish the excitation frequency of the input signal.

Figure 11 – Magnitude of the reflected wave amplitude ratio obtained for $2l_x \tan(\theta) \leq r_L < 4l_x \tan(\theta)$ (continuous line) and $4l_x \tan(\theta) \leq r_L < 6l_x \tan(\theta)$ (dotted line): (a) $\theta = 30°$ and (b) $\theta = 60°$. The dashed vertical lines indicate $l_x/\lambda_{l(d)}$ for the optimum frequencies f^l_{opt}.

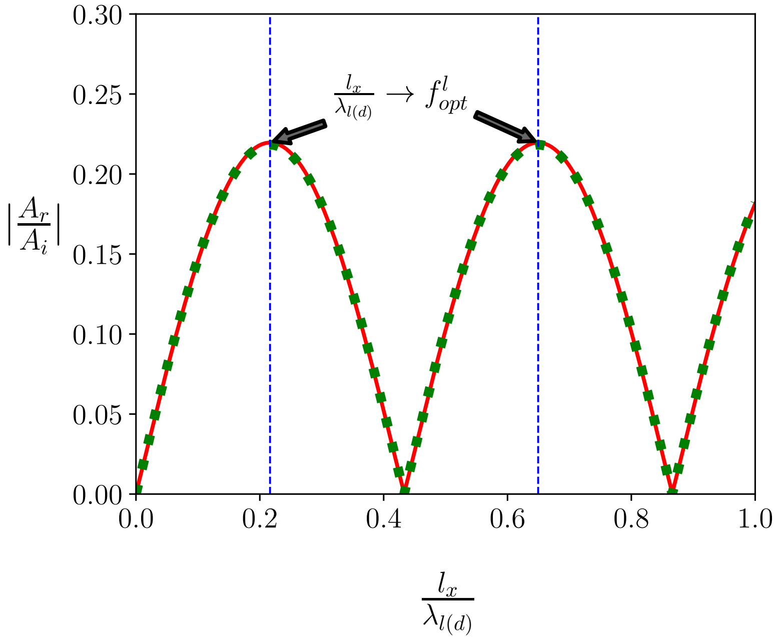

(a) $\theta = 30°$

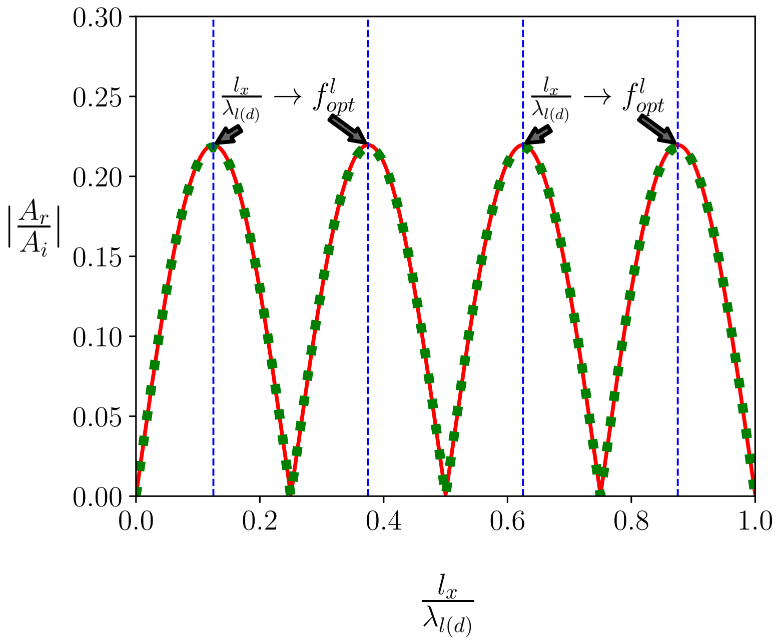

(b) $\theta = 60°$

Source: elaborated by the author.

Figure 12 – Magnitude of the transmitted wave amplitude ratio obtained for $2l_x \tan\theta \leq r_R < 4l_x \tan\theta$ (continuous line) and $4l_x \tan\theta \leq r_R < 6l_x \tan\theta$ (dotted line): (a) $\theta = 30°$ and (b) $\theta = 60°$. The dashed vertical lines indicate $l_x/\lambda_{l(d)}$ for the optimum frequencies f^l_{opt}.

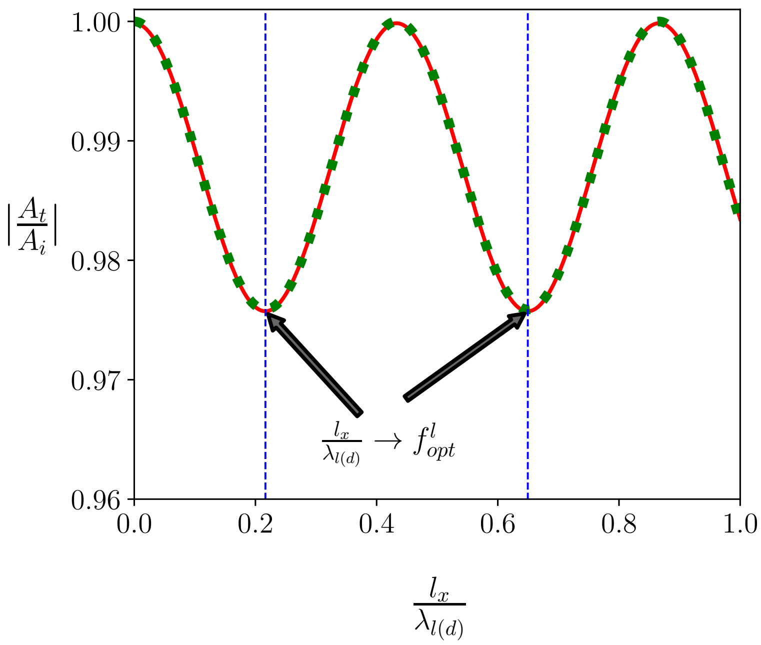

(a) $\theta = 30°$

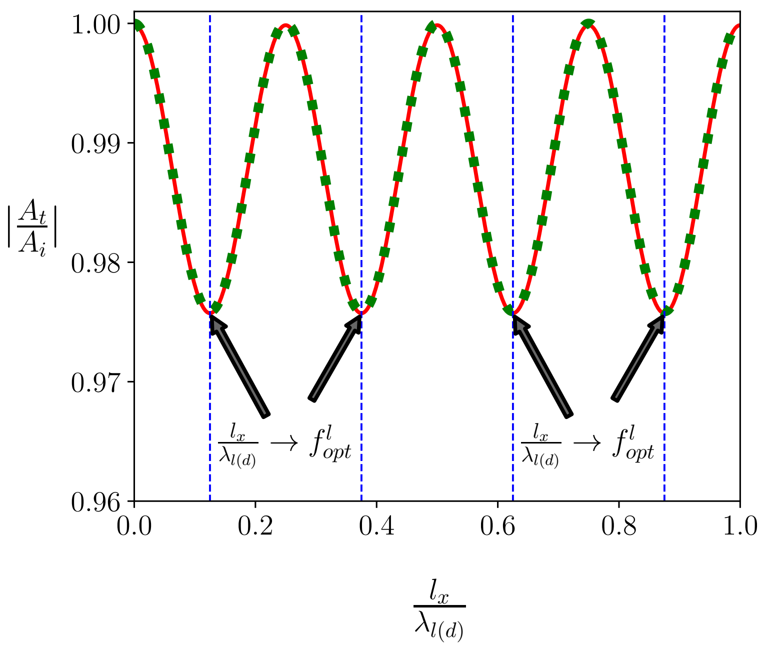

(b) $\theta = 60°$

Source: elaborated by the author.

The energy of the first reflected wave packet can be used to determine the plate thickness h_d in the damaged section. The idea for practical applications is to obtain the energy over time by measuring the wave amplitude. Note that the sensor size needs to be correctly defined, as presented previously herein. The damaged thickness h_d is numerically obtained from Equation (44). The procedure is illustrated by computing the Inverse Fourier Transform (IFT) of the first reflected wave packet amplitude for different damage depths, which allows one to obtain the amplitudes of the first reflected wave packets in the time domain. Then, three different levels of noise are artificially added to the obtained signals. The three noisy signals are numerically obtained by considering 3%, 5% and 10% of the signal energy (by using the of signal-to-noise ratio (SNR) approach). A similar approach is used by Rébillat, Hajrya and Mechbal (2014) and Brogin, Faber and Bueno (2020). The energy for each noisy signal is computed, and the corresponding damaged thickness h_d^{det} is determined by using Equation (44) for the different damage depths.

Briefly, (i) the amplitude of the first reflected wave packet is obtained in the frequency domain; (ii) the IFT is applied to the result; (iii) the noise is added to the signal in the time domain and; (iv) the relative energy is computed, which allows one to obtain h_d^{det}. Note that $h_d^{det} = h_d$ if no noise is considered. However, the noise affects the damaged thickness estimate. Then, $h_d^{det}/h_d = \bar{h}_d \to 1$ for low level of noise. Figure 13 shows $\bar{h}_d$ for the three different levels of noise and considering different damage depth $(1-h)$. Twenty signals were simulated for each boxplot shown in Fig. 13. The red line of the boxes indicate the median values obtained from the signals for each frequency, the lower and upper lines from the boxes show the first and third quartiles, respectively, and the vertical lines are called whiskers[1]. It is possible to obtain an accurate estimation of h_d for low damage depth even if that higher level of noise is considered. The accuracy decreases with increasing of noise if the damage depth is $(1-h) > 50\%$.

[1]For more information about boxplot figures, see https://matplotlib.org/stable/api/_as_gen/matplotlib.pyplot.boxplot.html.

Figure 13 – $\bar{h}_d$ in terms of the damage depth $(1-h)$. Continuous line corresponds to no noise condition. Symbols ◂, • and ▸ respectively correspond to the results obtained by considering 3%, 5% and 10% of noise added to the signal energy.

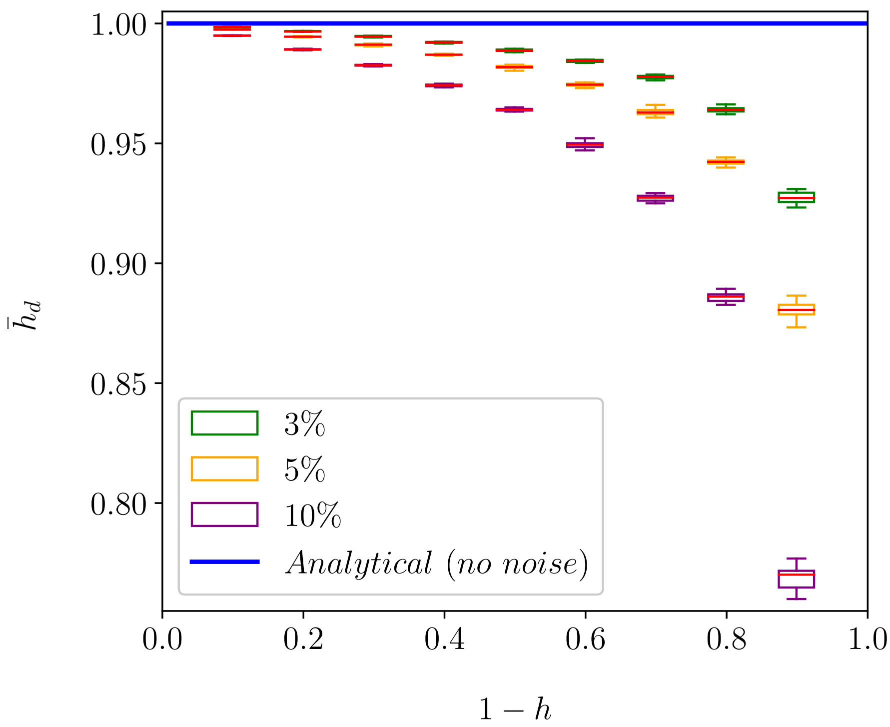

Source: elaborated by the author.

2.5 EXPERIMENTAL TESTS

The proposed approach is demonstrated through experimental tests. An aluminum plate with dimensions 1000×1000×1.5 mm is considered, for which E_p = 69 MPa, ρ_p = 2710 kg/m^3 and ν_p = 0.33. Figure 14 presents a schematic view and photographies of the experimental setup, which considers 3 circular piezoelectric transducers coupled to the plate. They are disc bender with ceramic diameters equal to 19.4 mm and thickness 0.45 mm, such that one of them works as an actuator (C) and the other ones are employed as sensors (S1 and S2). The input signals (five cycles tone burst) are generated by using a LabVIEW-based application with a NI USB 6353 National Instruments hardware, and a power amplifier EL 1225 Mide QuicPack. An oscilloscope DSO7034B Keysight is employed to measure the signals from the actuator and sensors.

Figure 14 – (a) Schematic view and (b) photographs of the experimental setup (measurements in cm).

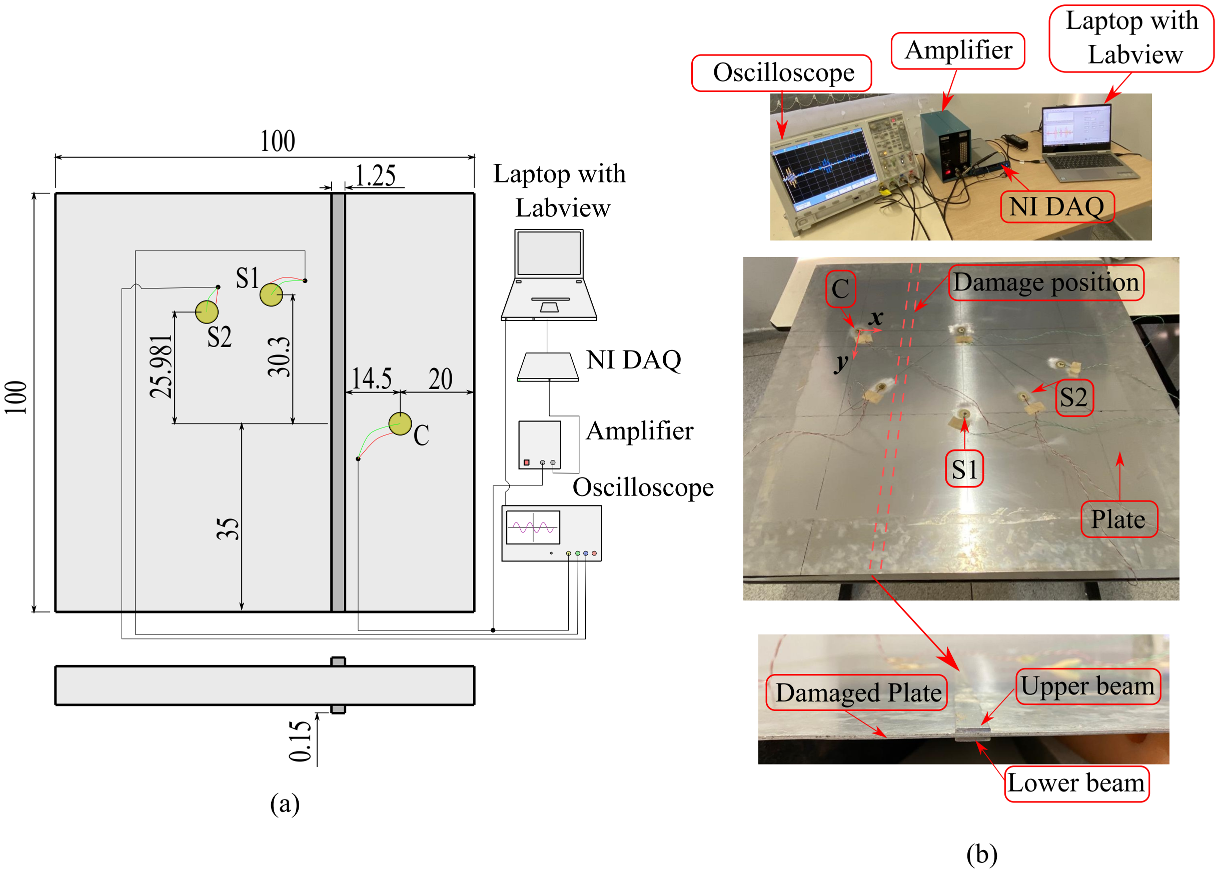

Source: elaborated by the author.

Considering the geometric center of the actuator at the origin of the coordinate system (x axis positive direction to the left-hand side and y direction up), the angles for the sensors S1 and S2 correspond to 45^o and 29.92^o in relation to the positive x axis, respectively. The symmetrical damage is created by two aluminum beams coupled to the faces of the plate (see their position in Fig. 14). Their geometric and physical properties are $1000 \times 12.5 \times 1.5$ mm, $\bar{E}_p = 70$ MPa and $\bar{\rho}_p = 2600$ kg/m^3. A double-sided adhesive tape model 430 of thickness 0.115 mm from Adelbras® was used to couple the beams to the plate. Note that the damaged section in this case is composed by two different materials, and because of this the Equivalent Cross Section Method is employed to compute resulting properties for the damaged section (HIBBELER, 2010). Figure 15 presents an illustrative representation of two different materials, ‘‘a’’ and ‘‘b’’, with cross sections S_m and S_n, Young's modulus E_m and E_n, and densities ρ_m and ρ_n. They have the same strain ε, but different stresses (σ_m,σ_n). ‘‘c’’ is the equivalent material, and let F_{eq} be the equivalent force applied in the cross section of material ‘‘c’’, where $F_{eq} = S_{eq}\sigma_{eq}$. It corresponds to the sum of forces in both materials, i.e., $F_{eq} = F_m + F_n$. In addition, considering the Hooke's

Law for mechanical stresses ($\sigma = E\varepsilon$), and the equivalent area $S_{eq} = S_m + S_n$, it is possible to obtain

$$E_{eq} = E_o = \frac{E_m S_m + E_n S_n}{S_m + S_n}. \tag{45}$$

The mass of the material "c" is given by the sum of masses "a" and "b" ($m_o = m_m + m_n$), and its equivalent density is given by

$$\rho_{eq} = \rho_o = \frac{\rho_m S_m + \rho_n S_n}{S_m + S_n}. \tag{46}$$

Then, Equations (45) and (46) are used to determine the properties of the damaged section.

Figure 15 – Schematic representation of an equivalent section (material "c") from a damaged section composed by two different materials ("a" and "b").

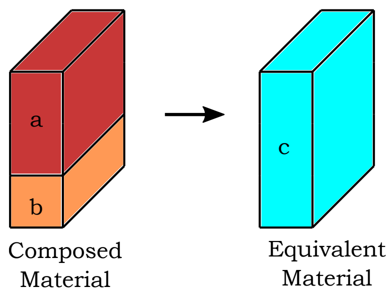

Source: elaborated by the author.

Note that the created damage corresponds to the local cross-section increasing, instead of reduction. This is a convenient strategy due to its relative simplicity to be obtained. Similar approach has been employed in the literature, as presented by Gonsalez *et al.* (2015) and Hou *et al.* (2020) for example. The main point of the equivalence between reduction or increase the local mass is that the optimal frequencies for damage detection are equals for both of them, although the wave amplitude ratios are different (compare Figure 16(a) and 16(b) for the same $l_x/\lambda_{l(p)}$). Figure 16 shows the magnitudes of the reflected (Fig. 16a) and transmitted (Fig. 16b) wave amplitude ratios, respectively by dashed and continuous lines. The mass increasing is obtained by considering $h = 1.5$, whereas $h = 0.5$ is used for the mass reduction in the damaged section. Then, both strategies are equivalent to each other for the proposal in this chapter. In practice, the methodology presented herein can be used for both configurations, such that a mass addition is represented by $h > 1$, whereas a mass subtraction corresponds to $h < 1$, and the optimal frequencies are equal to each other for both ones, as presented in Figure 16.

Figure 16 – Magnitude of the (a) reflected and (b) transmitted wave amplitude ratios obtained for $4l_x \tan(\theta) \leq r_{()} < 6l_x \tan(\theta)$, considering $\theta = 60^o$: Mass reduction by $h = 0.5$ (dashed-line) and mass increase by $h = 1.5$ (continuous line).

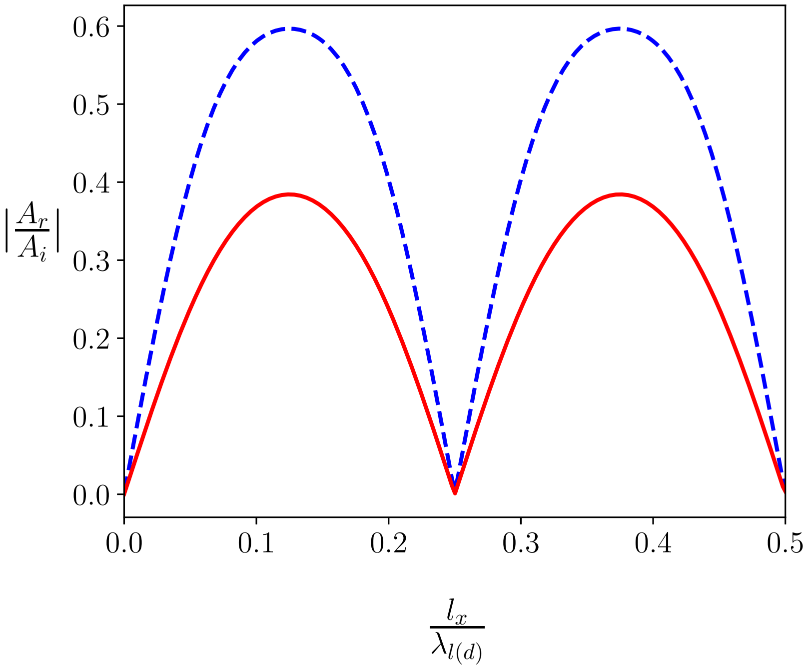

(a) Reflected wave amplitude ratio

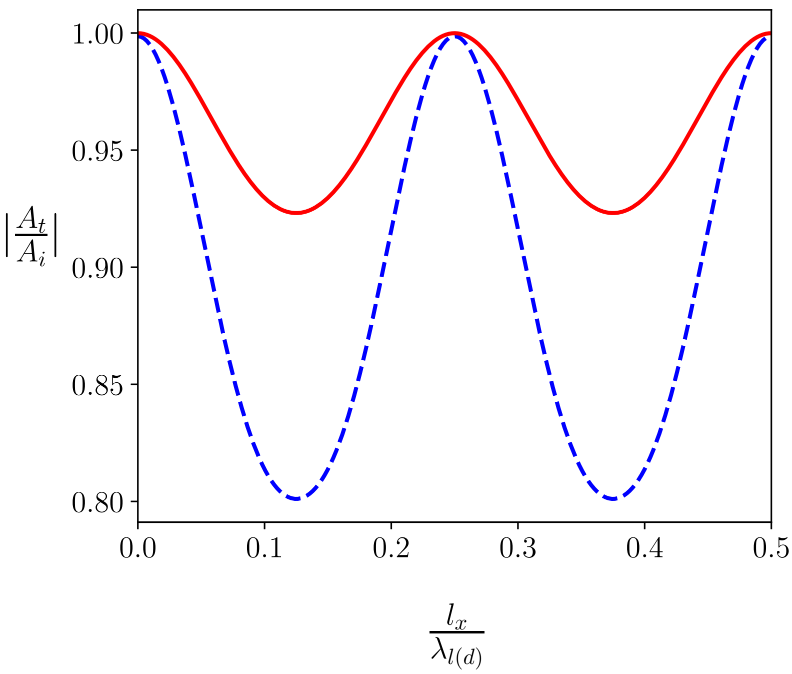

(b) Transmitted wave amplitude ratio

Source: elaborated by the author.

The resulting damaged section is composed by two different materials (from the plate and beams), and its equivalent physical properties are obtained by using the approach introduced previously, from which $E_d = E_{eq} = 69.67$ MPa and $\rho_d = \rho_{eq} = 2636.67$ kg/m^3. The double-sided adhesive tapes are not taken into account to obtain this equivalent damaged section due to their small effect on these properties. The double-sided adhesive tape has Young's modulus $E_b = 10$ MPa, material density $\rho_b = 1000$ kg.m^{-3} and thickness $h_b = 0.115$ mm. Then, if they are considered with the plate and beams to define the equivalent damaged section, its equivalent properties are equal to $\tilde{E}_{eq} = 69.66$ MPa and $\tilde{\rho}_{eq} = 2636.58$ kg.m^{-3}. On the other hand, neglecting them, the equivalent properties of the damaged section are equal to $E_{eq} = 69.67$ MPa and $\tilde{\rho}_{eq} = 2636.67$ kg.m^{-3}, which allows one to show the small influence of the double-sided adhesive tape. In addition, note that a good agreement is observed when comparing experimental and theoretical results.

The sensors radii are $r_{S1} = r_{S2} = 9.7$ mm and the damage length is $l_x = 12.5$ mm, which allows one to verify that both sensors S1 and S2 capture just the first wave packet from their respective angle $\theta_1^{(\,)}$ because $r_{S1} < 2l_x \tan(\theta_1^{(S1)}) = 25$ mm and $r_{S2} < 2l_x \tan(\theta_1^{(S2)}) = 14.40$ mm, where $\theta_1^{(S1)} = 45^o$ and $\theta_1^{(S2)} = 29.92^o$ (i.e., from the angles of the waves coming from the actuator directly to the respective sensors S1 and S2). The resulting wave (Eq. 40) is obtained by considering the second wave packet propagating in the direction of the angle $\theta_2^{(\,)}$, such that $\theta_2^{(S2)} < \theta_1^{(S2)}$ and $\theta_2^{(S1)} < \theta_1^{(S1)}$ and $\theta_2^{(S2)} = 28.6^o$ and $\theta_2^{(S1)} = 42.4^o$. The angles were obtained from the drawing using a software CAD. In this case, healthy and damaged sections of the plate have different physical properties, then it is necessary to compute the angle of propagation inside the damage by using the Snell-Descartes' law. In addition, Eqs. (25) and (24) have to be used to compute the wave amplitude ratios of the wave packets. Figure 17(a) shows the damage index to demonstrate that the experimental resulting wave in the sensor S1 is accurately predicted from Equation (40). The experimental results[1] are presented through the symbol $\Diamond$ and the corresponding theoretical results are shown through the symbol $\square$. On the other hand, the theoretical prediction fails if more wave packets are considered for the sensor S1, as shown through the symbols $\triangledown$ and $\circ$, respectively corresponding to $\theta = 45^o$ and $\theta = 42.4^o$. Similar conclusions are obtained from the sensor S2 for $l_x/\lambda_p \geq 0.35$, as shown in Fig. 17(b).

[1]These experimental data correspond to the reference signals, which are arbitrarily defined as the first measurement for each frequency.

Figure 17 – Damage Index $\bar{R}$ computed using: the reference experimental results (symbol $\Diamond$); proposed approach [Equation 40] (symbol $\square$); and theoretical prediction considering infinite wave packets arriving at the sensor, in which a) $\theta = 45^o$ (symbol $\triangledown$) or $\theta = 42.4^o$ (symbol $\circ$), and b) $\theta = 29.92^o$ (symbol $\triangledown$) or $\theta = 28.6^o$ (symbol $\circ$).

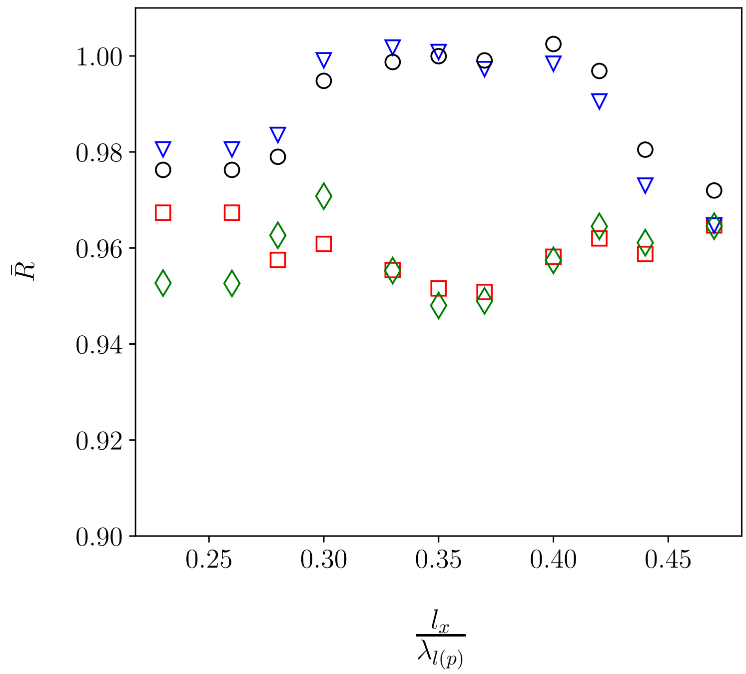

(a) Sensor S1

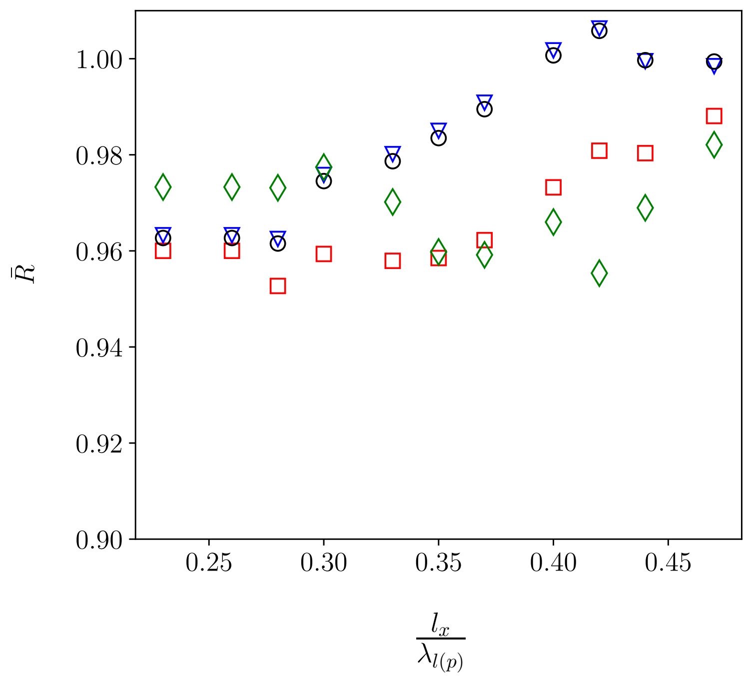

(b) Sensor S2

Source: elaborated by the author.

The experimental signals were measured by S1 for the healthy and damaged structures at the frequencies from 100 kHz up to 200 kHz, corresponding to the range $0.20 < l_x/\lambda_{l(p)} < 0.50$. The first measured signal for the healthy condition is used as reference to compute the damage index. Figures 18 and 19 show the longitudinal waves measured by using the sensor S1 respectively for both healthy and damaged conditions. Note that a 5 cycles tone burst at the frequency 160 kHz is used. Figure 20 presents the magnitude of these signals in the frequency domain, from which different magnitude can be noted when comparing the healthy and damaged conditions. Figure 21 presents the boxplot for these data, in which the outliers are omitted for easier viewing. A horizontal blue dashed line indicates the global threshold for all frequencies investigated, and then the results above it correspond to the healthy condition. On the other hand, the damage is detected for all signals obtained for the damaged structure - see the results below the threshold line. Similar results are found from the sensor S2, as shown in Figure 22.

Figure 18 – Longitudinal waves in the time domain measured by sensor 1 for the healthy plate, considering as input a 5 cycles tone burst at the frequency 160 kHz.

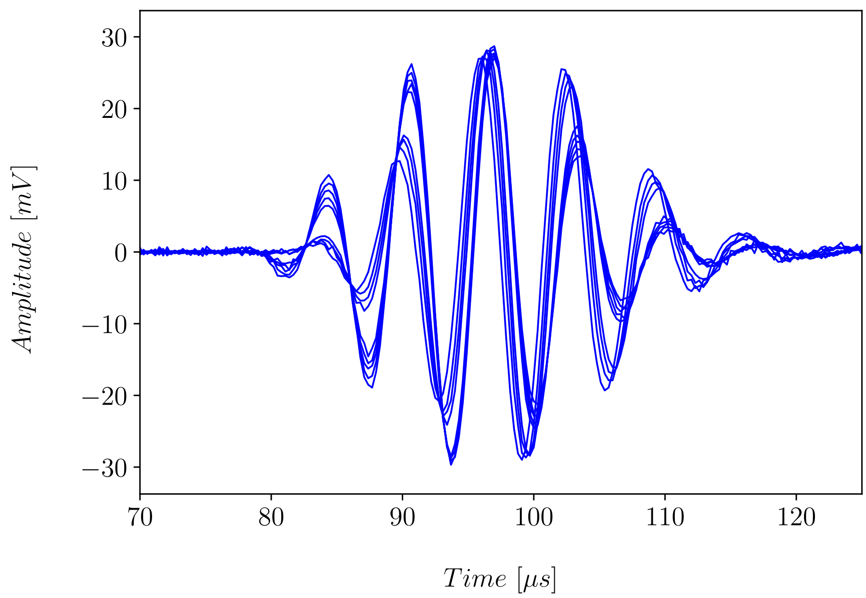

Source: elaborated by the author.

Figure 19 – Longitudinal waves in the time domain measured by sensor 1 for the damaged plate, considering as input a 5 cycles tone burst at the frequency 160 kHz.

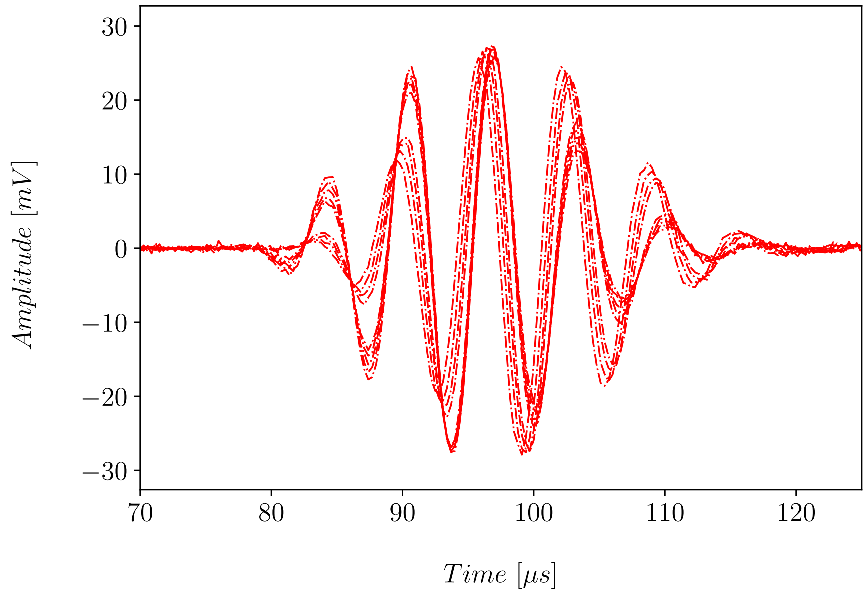

Source: elaborated by the author.

Figure 20 – Magnitude in the frequency domain of the measured signals by sensor 2 for the healthy (continuous lines) and damaged structure (dash-dotted lines), considering as input a 5 cycles tone burst at the frequency 160 kHz. There are 10 signal for each condition.

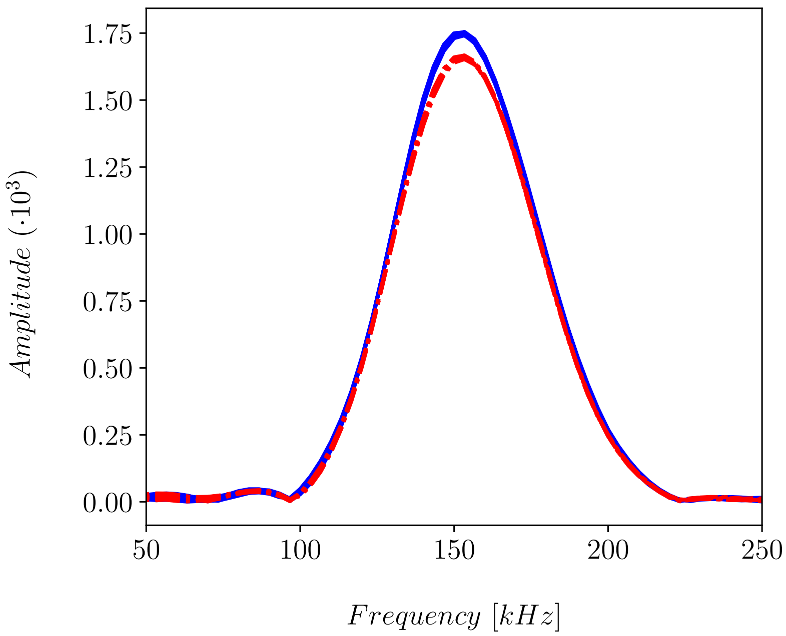

Source: elaborated by the author.

Figure 21 – Sensor 1: boxplot of the damage index $\bar{R}$ and threshold (dashed-line) $\bar{R}_l = 0.99$. Damage detected for all frequencies (below the threshold line).

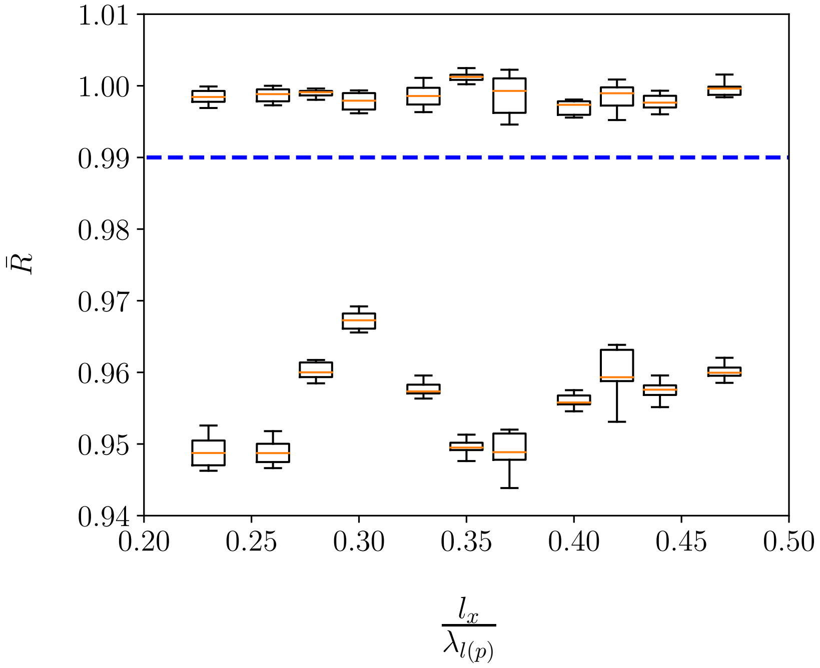

Source: elaborated by the author.

Figure 22 – Sensor 2: boxplot of the damage index $\bar{R}$ and threshold (dashed-line) $\bar{R}_l = 0.99$. Damage detected for all frequencies (below the threshold line).

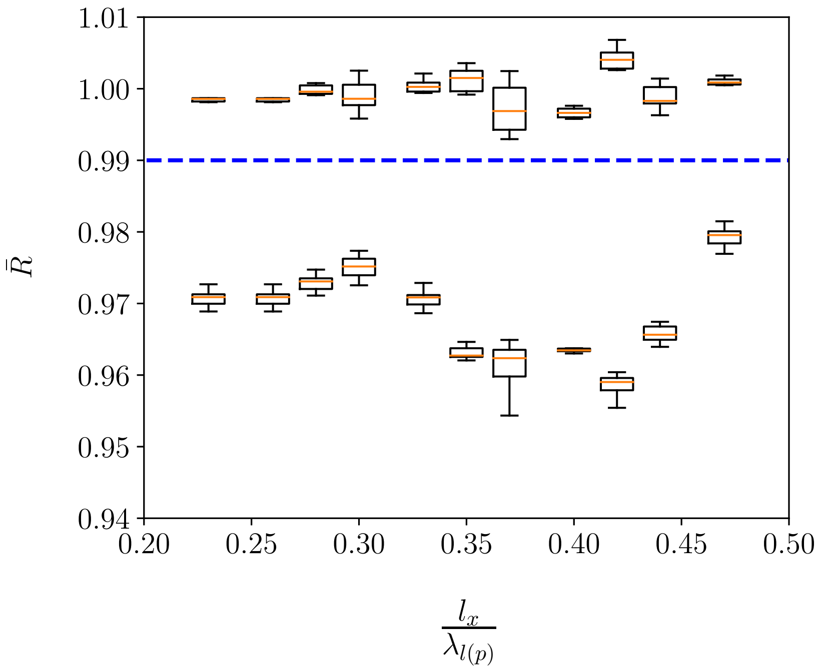

Source: elaborated by the author.

This approach can not be applied to composite-like structures. However, a few works presented in the literature have addressed the problems shown in this chapter, such as the oblique incidence of longitudinal waves into symmetrical damages and how these waves interact with this type of discontinuity for oblique incidence. In addition, analytical equations to compute optimal frequencies for damage detection based on longitudinal waves are also introduced, which can help the SHM analyst during a damage detection campaign based on wave propagation.

2.6 FINAL REMARKS

This chapter presented an investigation into the scattering of longitudinal waves in plates with symmetric damage. A model was presented to describe each wave packet for the transmitted and reflected waves using an oblique incident wave directed to the damaged section. It is demonstrated that the maximum amplitude of reflected wave does not depend on the angle of incidence. However, the incident angle changes the frequencies at which the maximum amplitude occurs. This also corresponds to the minimum amplitudes of the transmitted wave, which are also independent of the angle of incidence.

The results show that transmitted waves are only slightly affected by the damage for low damage depth (i.e., $(1 - h) < 0.2$), where h is the ratio between the damaged and undamaged thickness of the plate. In addition, the first wave packet for the transmitted wave is much larger than the following packets. On the other hand, the first and second wave packets for the reflected wave also indicate the presence of damage, mainly for $(1 - h) < 0.4$. These characteristics can be strategically considered to define the size of the sensors for SHM procedures.

The sensor size can be defined for each damage width l_x which the SHM system needs to detect. In typical practical applications of SHM, such as damage detection in an aeronautical structure, the damage to be detected is previously defined by the SHM analyst. Thus, the optimal configuration can be determined by using this proposed approach in terms of frequency range and sensor size. Considering a circular sensor used to measure the reflected wave (see point e in Fig. 3), its radius is determined to be $r_L < 2l_x \tan(\theta)$. This size allows one to measure the first wave packet separately from the other packets. The obtained wave can be used to estimate the damage depth $(1 - h)$ because the plate thickness can be determined. This is a very convenient approach for practical applications, and an optimal frequency does not need to be considered to excite the structure. If the SHM system requires the use of sensors with radii $r \geq 2l_x \tan(\theta)$, the resulting measurements contain more than one wave packet. The resulting wave amplitude also depends on the excitation frequency.

The damage depth $(1-h)$ can be easily estimated from the first reflected wave packet. If the sensor radius is $r_L < 2l_x \tan(\theta)$, the plate thickness h_d in the damaged section is determined in terms of the plate thickness h_p. The proposed approach is relatively insensitive to noise in the output signals and hence provides a promising approach for the design of SHM applications for detecting damage in plate-like structures.

The proposed approach is demonstrated by experimental data obtained from a circular actuator. The transducer generates radial waves in all the directions of the plate, as previously noted in the literature. The results show that the sensors responses are well described by the sum of two wave packets propagating in two different directions. These directions are determined herein by the angles θ_1 (for the first wave packet) and θ_2 (for the second one) since the radii are $r_{()} < 2l_x \tan(\theta_1)$, where $\theta_1 > \theta_2$. A threshold is proposed based on a damage index and the index allows one to detect the damage from a set of signals measured for an unknown structural condition. A single threshold is presented for simplicity, but in practice it is computed for each frequency of interest. Boxplot is used, and the procedure involves to measure a set of signals also for describing the healthy condition, before monitoring the structure, which allows one to establish an interesting approach for damage detection based on wave propagation.

An asymmetrical damage is more often observed in comparison with the symmetrical shape. However, it is important to understand how longitudinal waves interact with symmetrical damage to have a better understanding of the asymmetrical case. In addition, despite its apparent simplicity, the symmetrical damage allows one to obtain the optimal frequencies for damage detection that are close to those observed for asymmetrical damages, as shown in reference (LOPES *et al.*, 2022). Then, the SHM analyst can use the equations presented herein to predict optimal frequencies for both types of damage, if there is a low level of asymmetry. In the sense of external effects, such as temperature, on the choice of the location and size of the sensors, further studies can be carried out to investigate their influence.

3 FLEXURAL WAVES WITH OBLIQUE INCIDENCE

This chapter presents an approach to investigate flexural wave scattering into symmetrical damage of a thin plate considering oblique incidence. Numerical simulations are carried out and the results show that the sensor size determines the number of wave packets collected according to the damage length and the incidence angle. Experimental tests are presented considering radial wave propagating created by a circular actuator and they are compared with the theoretical results. The findings contribute to SHM systems based on flexural wave propagation used to detect damage in plate-like structures and improve the current state of the art in wave propagation SHM by investigating the effects of different excitation frequencies and the influence of the damage parameters and sensor sizing on the resulting waves.

3.1 FLEXURAL WAVE PROPAGATION IN THIN PLATES

Consider an infinitesimal element with thickness h_p on the x-y plane, as shown in Figure 23. The Young‘s modulus is E_p, density is ρ_p and the Poison‘s coefficient is ν_p. The infinitesimal element has area $dxdy$ with forces and bending moments applied, such that M_x and M_y are bending moments, M_{xy} and M_{yx} are twisting moments and Q_x and Q_y are shear forces.

Consider $w = w(x, y, t)$ the transversal displacement at the point (x, y) of the element shown in Figure 23, the slope along the x direction is $\theta_x = \frac{\partial w}{\partial x}$ and $\theta_y = \frac{\partial w}{\partial y}$ along the y direction. The moments and forces are $M_x = -D_p\left(\frac{\partial^2 w}{\partial x^2} + \nu_p \frac{\partial^2 w}{\partial y^2}\right)$, $M_y = -D_p\left(\frac{\partial^2 w}{\partial y^2} + \nu_p \frac{\partial^2 w}{\partial x^2}\right)$, $M_{xy} = M_{yx} = -(1-\nu_p) D_p \frac{\partial^2 w}{\partial x \partial y}$, $Q_x = -D_p\left(\frac{\partial^3 w}{\partial x^3} + \frac{\partial^3 w}{\partial x \partial y^2}\right)$ and $Q_y = -D_p\left(\frac{\partial^3 w}{\partial y^3} + \frac{\partial^3 w}{\partial x^2 \partial y}\right)$, where $D_p = \frac{E_p h_p^3}{12(1-\nu_p^2)}$ is the flexural rigidity of bending stiffness. The shear forces V_x and V_y in the x and y directions are given by $V_x = Q_x - \frac{\partial M_{xy}}{\partial y} = -D_p\left(\frac{\partial^3 w}{\partial x^3} + (2-\nu_p)\frac{\partial^3 w}{\partial x \partial y^2}\right)$ and $V_y = Q_y - \frac{\partial M_{yx}}{\partial y} = -D_p\left(\frac{\partial^3 w}{\partial y^3} + (2-\nu_p)\frac{\partial^3 w}{\partial x^2 \partial y}\right)$, respectively (GRAFF, 1991; GIURGIUTIU, 2014a). Applying the Newton’s second law in the infinitesimal element from Figure 23, it

Figure 23 – Infinitesimal element with area $dxdy$ and thickness h_p on the x-y plane with moments and forces.

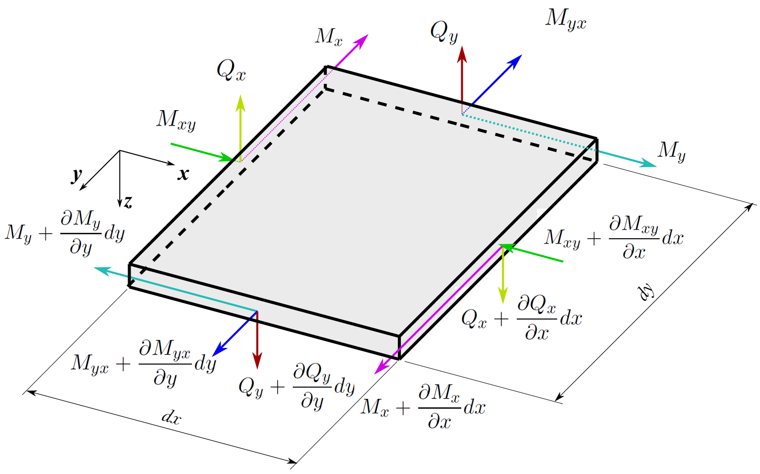

Source: elaborated by the author.

is possible to obtain

$$Q_x dy - \left(Q_x + \frac{\partial Q_x}{\partial x} dx\right) dy + Q_y dx - \left(Q_y + \frac{\partial Q_y}{\partial y} dy\right) dx = \rho_p h_p \; dx \; dy \; \frac{\partial^2 w}{\partial t^2} \tag{47}$$

$$\left(M_y + \frac{\partial M_y}{\partial y} dy\right) dx - M_y dx - M_{xy} dy + \left(M_{xy} + \frac{\partial M_{xy}}{\partial x} dx\right) dy - Q_y \; dx \; dy = 0 \tag{48}$$

$$\left(M_x + \frac{\partial M_x}{\partial x} dx\right) dy - M_x dy - M_{yx} dx + \left(M_{yx} + \frac{\partial M_{yx}}{\partial y}\right) dx - Q_x \; dx \; dy = 0. \tag{49}$$

The Equations (47) to (49) can be rewritten as follows

$$\frac{\partial Q_x}{\partial x} + \frac{\partial Q_y}{\partial y} = \rho_p h_p \frac{\partial^2 w}{\partial t^2} \tag{50}$$

$$Q_y = \frac{\partial M_y}{\partial y} + \frac{\partial M_{xy}}{\partial x} \tag{51}$$

$$Q_x = \frac{\partial M_x}{\partial x} + \frac{\partial M_{xy}}{\partial y}. \tag{52}$$

Replacing Equations (51) and (52) into (50), it is possible to obtain the equation of motion for flexural waves, such that

$$D_p\left(\nabla^4 + \frac{\rho_p h_p}{D_p}\frac{\partial^2}{\partial t^2}\right)w(x,y,t) = 0 \tag{53}$$

where $\nabla^4 = \left(\frac{\partial^4}{\partial x^4} + 2\frac{\partial^4}{\partial x^2 \partial y^2} + \frac{\partial^4}{\partial y^4}\right)$. In particular for a harmonic motion, Equation (53) can be rewritten by

$$D_p\left(\nabla^4 - k_f^4\right)w(x,y,k_{f(p)}) = 0 \tag{54}$$

where $k_f = \sqrt{\omega}\sqrt[4]{\frac{\rho_p h_p}{D_p}}$ is the flexural wavenumber. $k_{f(p)} \equiv k_f$ is computed by considering the physical and geometrical properties of the undamaged region of the plate. Let $\bar{w} = Ae^{-i(k_x x + k_y y)}$ be the solution, and replacing it into the equation of motion, the obtained equation is $k_x^4 + 2k_x^2k_y^2 + k_y^4 = k_{f(p)}^4$. In this case, equations $(k_x^2 + k_y^2) = k_{f(p)}^2$ and $-(k_x^2 + k_y^2) = k_{f(p)}^2$ are obtained, once $(k_x^2 + k_y^2)^2 = (k_{f(p)}^2)^2$. Considering a wave propagating in the y positive direction, the equations $k_{x1} = \sqrt{k_{f(p)}^2 - k_y^2}$, $k_{x2} = -\sqrt{k_{f(p)}^2 - k_y^2}$, $k_{x3} = i\sqrt{k_{f(p)}^2 + k_y^2}$ and $k_{x4} = -i\sqrt{k_{f(p)}^2 + k_y^2}$ can be derived, which allows one to write the solution for the equation of motion as follows: $\bar{w}(x,y,\omega) = A_1e^{-i(k_{x3}x + k_y y)} + A_2e^{-i(k_{x4}x + k_y y)} + A_3e^{-i(k_{x2}x + k_y y)} + A_4e^{-i(k_{x1}x + k_y y)}$. Replacing k_{x1} to k_{x4} into this last equation, the transversal displacement is written by $\bar{w}(x,y,\omega) = A_1e^{(\bar{k}_x x - ik_y y)} + A_2e^{(-\bar{k}_x x - ik_y y)} + A_3e^{i(k_x x - k_y y)} + A_4e^{i(-k_x x - k_y y)}$, where $i = \sqrt{-1}$, $k_x = \sqrt{k_{f(p)}^2 - k_y^2}$, $\bar{k}_x = \sqrt{k_{f(p)}^2 + k_y^2}$ and with $k_y = k_{f(p)}\sin(\alpha)$ (GRAFF, 1991; CUENCA, 2009; GOLATO; DEMIRLI; SANTHANAM, 2014). A_1 and A_2 indicate the wave amplitudes propagating in the y positive direction, and attenuating in the x negative and positive directions, respectively. A_3 and A_4 are wave amplitudes propagating in y positive direction, respectively with x negative and positive directions. Figure 24 illustrates these described wave amplitudes from an arbitrary point o, which can be conveniently defined as the origin of the coordinate system, and an angle α in relation to the x axis.

In addition, $\bar{\theta}_x(x,y,k_{f(p)})$, $\bar{M}_x(x,y,k_{f(p)})$ and $\bar{V}_x(x,y,k_{f(p)})$ are determined by using $\bar{w}(x,y,\omega)$, such as

$$\begin{aligned}
\bar{\theta}_x(x,y,\omega) &= A_1\bar{k}_x e^{\bar{k}_x x - ik_y y} - A_2\bar{k}_x e^{-\bar{k}_x x - ik_y y} + A_3 ik_x e^{i(k_x x - k_y y)} - A_4 ik_x e^{i(-k_x x - k_y y)} \\
\bar{M}_x(x,y,\omega) &= -A_1Je^{\bar{k}_x x - ik_y y} - A_2Je^{-\bar{k}_x x - ik_y y} + A_3Ke^{i(k_x x - k_y y)} + A_4Ke^{i(-k_x x - k_y y)} \\
\bar{V}_x(x,y,\omega) &= -A_1Pe^{\bar{k}_x x - ik_y y} + A_2Pe^{-\bar{k}_x x - ik_y y} + A_3Ne^{i(k_x x - k_y y)} - A_4Ne^{i(-k_x x - k_y y)}
\end{aligned} \tag{55}$$

where $J = D_p\left(\bar{k}_x^2 - k_y^2\nu_p\right)$, $K = D_p\left(k_x^2 + k_y^2\nu_p\right)$, $P = D_p\bar{k}_x\left(\bar{k}_x^2 + k_y^2\left(\nu_p - 2\right)\right)$ and $N =$

Figure 24 – Flexural waves with amplitudes A_4 and A_3 that propagate in the quadrants I and II, respectively. A_1 and A_2 correspond to the wave amplitudes propagating in the y positive direction, attenuating in the left and right hand sides of the y direction.

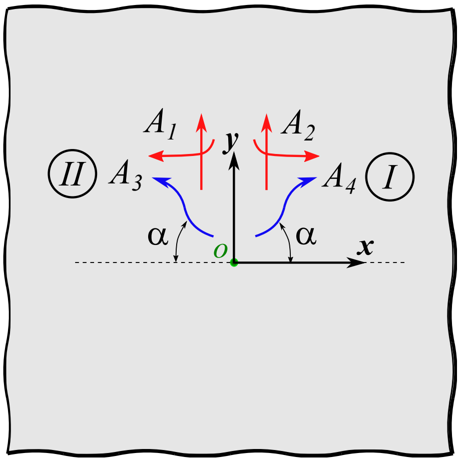

Source: elaborated by the author.

$iD_p k_x\left(k_x^2 - k_y^2\left(\nu_p - 2\right)\right)$. It is convenient to define the states vector $\mathbf{h}(x, y, \omega) = \{\bar{w} \;\; \bar{\theta}_x \;\; \bar{M}_x \;\; \bar{V}_x\}^T$ for any point (x, y) on the plate, and it is rewritten by $\mathbf{h}(x, y, \omega) = \mathbf{H}(\omega)\mathbf{T}(x, y, \omega)\mathbf{a}(\omega)$, such that

$$\mathbf{H}(\omega) = \begin{bmatrix} 1 & 1 & 1 & 1 \\ \bar{k}_x & -\bar{k}_x & ik_x & -ik_x \\ -J & -J & K & K \\ -P & P & N & -N \end{bmatrix} \tag{56}$$

$$\mathbf{T}(x, y, \omega) = diag\left(e^{\bar{k}_x x - ik_y y} \quad e^{-\bar{k}_x x - ik_y y} \quad e^{i(k_x x - k_y y)} \quad e^{i(-k_x x - k_y y)}\right) \tag{57}$$

$$\mathbf{a}(\omega) = \{A_1 \quad A_2 \quad A_3 \quad A_4\}^T \tag{58}$$

where $\mathbf{H}(\omega)$ is the transformation matrix, $\mathbf{T}(x, y, \omega)$ is the spatial transformation matrix and $\mathbf{a}(\omega)$ is the wave amplitudes vector.

3.2 TRANSMITTED AND REFLECTED WAVE COEFFICIENTS DUE TO CROSS-SECTION CHANGE

This section presents the coefficients of transmitted and reflected waves considering a reduction or increase of a symmetric cross-section change along the y direction. Consider a flexural wave incoming in a symmetrical cross-section change reduction shown in Figure 25(a). The incident wave propagates in the x and y positive directions with a wave amplitude A_{4i} to achieve the point q. Due to the interaction with the cross-section change, transmitted (A_4^q) and reflected (A_3^q) flexural waves are created at this point. The state vector is $\mathbf{h}_p^q = \mathbf{h}_d^q$, where $\mathbf{h}_p^q = \mathbf{H}_p\mathbf{a}_p^q$, such that $\mathbf{H}_p$ represents the transformation matrix (Equation 56) for the undamaged plate. The wave amplitude vector is $\mathbf{a}_p^q = \{A_1^q\ 0\ A_3^q\ A_{4i}^q\}^T$, and similarly, $\mathbf{h}_d^q = \mathbf{H}_d\mathbf{a}_d^q$, such that $\mathbf{H}_d$ is the transformation matrix for the damaged section of the plate (i.e., using h_d) and $\mathbf{a}_d^q = \{0\ A_2^q\ 0\ A_4^q\}^T$. Rearranging these equations to write $\mathbf{a}_{out} = \mathbf{Z}_r\mathbf{a}_{in}$, such that $\mathbf{a}_{out} = \{A_1^q\ A_2^q\ A_3^q\ A_4^q\}^T$, $\mathbf{a}_{in} = \{0\ 0\ 0\ A_{4i}^q\}^T$ and $\mathbf{Z}_r = \mathbf{X}_r^{-1}\mathbf{Y}_r$. The matrices $\mathbf{X}_r$ and $\mathbf{Y}_r$ are given by

Figure 25 – (a) Thin plate with reduction of symmetrical cross-section in the y direction and generated wave amplitudes considering incidence of flexural wave with amplitude A_{4i}^q at the point q. (b) Thin plate with increase of symmetrical cross-section in the y direction and generated wave amplitudes considering incidence of flexural wave (A_{4i}^r) and effect of an attenuating wave ($\bar{A}_2^r$) in the x positive direction at the point r.

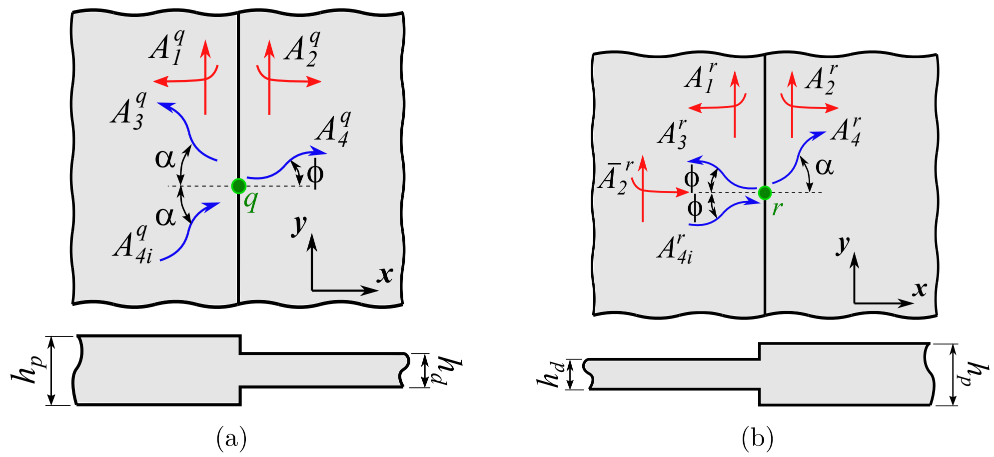

Source: elaborated by the author.

$$\mathbf{X}_r = \left[(\mathbf{H}_p|_1)\ \ (-\mathbf{H}_d|_2)\ \ (\mathbf{H}_p|_3)\ \ (-\mathbf{H}_d|_4)\right] \tag{59}$$

$$\mathbf{Y}_r = \left[(\mathbf{H}_d|_1)\ \ (-\mathbf{H}_p|_2)\ \ (\mathbf{H}_d|_3)\ \ (-\mathbf{H}_p|_4)\right] \tag{60}$$

where $|_z$ indicates the z-th column of the represented matrix ($z = 1, \ldots, 4$) and r indicates the cross-section reduction. The coefficients of cross-section reduction for transmitted and reflected waves are respectively given by $R_t = A_4^q/A_{4i}^q$ and $R_r = A_3^q/A_{4i}^q$, and they can be conveniently used to investigate interaction of the flexural wave with damage such as introduced in the following sections.

On the other hand, consider the cross-section increasing shown in Figure 25(b). Two waves are incoming at the point r: the flexural wave A_{4i}^r and the flexural wave $(\bar{A}_2^r)$ that propagates to the y positive direction and attenuates in the x positive direction. Transmitted (A_4^r) and reflected (A_3^r) flexural waves are created at the point r. The wave $\bar{A}_2^r$ is created at the point $(r-1)$ of coordinates (x_{r-1}, y_{r-1}), such that $x_{r-1} < x_r$ and $y_{r-1} \leq y_r$. Similarly to the cross-section reduction, the state vector at the point r is $\mathbf{h}_d^r = \mathbf{h}_p^r$, where $\mathbf{h}_d^r = \mathbf{H}_d\mathbf{a}_d^r$ and $\mathbf{h}_p^r = \mathbf{H}_p\mathbf{a}_p^r$, such that $\mathbf{a}_d^r = \{A_1^r\ \bar{A}_2^r\ A_3^r\ A_{4i}^r\}^T$ and $\mathbf{a}_p^r = \{0\ A_2^r\ 0\ A_4^r\}^T$. In this case, $\mathbf{a}_{out} = \{A_1^r\ A_2^r\ A_3^r\ A_4^r\}^T$ and $\mathbf{a}_{in} = \{0\ \bar{A}_2^r\ 0\ A_{4i}^r\}^T$, and they are related by $\mathbf{a}_{out} = \mathbf{Z}_i\mathbf{a}_{in}$, where $\mathbf{Z}_i = \mathbf{X}_i^{-1}\mathbf{Y}_i$, such that $\mathbf{X}_i$ and $\mathbf{Y}_i$ are given by

$$\mathbf{X}_i = [(\mathbf{H}_d|_1)\ \ (-\mathbf{H}_p|_2)\ \ (\mathbf{H}_d|_3)\ \ (-\mathbf{H}_p|_4)] \tag{61}$$

$$\mathbf{Y}_i = \left[(\mathbf{H}_p|_1)\ \ (-\mathbf{H}_d|_2)\ \ (\mathbf{H}_p|_3)\ \ (-\mathbf{H}_d|_4)\right]. \tag{62}$$

The coefficients of the cross-section increasing for the transmitted and reflected waves are given by $I_t^{r(r-1)} = A_4^r/A_{4i}^r$ and $I_r^{r(r-1)} = A_3^r/A_{4i}^r$, respectively, which allows one to obtain the following equations

$$I_r^{r(r-1)} = Z_i^{(32)}\frac{\bar{A}_2^r}{A_{4i}^r} + Z_i^{(34)} \tag{63}$$

$$I_t^{r(r-1)} = Z_i^{(42)}\frac{\bar{A}_2^r}{A_{4i}^r} + Z_i^{(44)} \tag{64}$$

where $Z_i^{(mn)}$ is the element of the matrix $\mathbf{Z}_i$ in the row m and column n. Note the attenuating wave influence on the coefficients, such that the ratio is given by $\frac{\bar{A}_2^r}{A_{4i}^r} = \frac{C_{exp}}{C_p}\frac{e^{-\bar{k}_x^d\bar{x}_r - ik_y^d\bar{y}_r}}{e^{i(-k_x^d\bar{x}_r - k_y^d\bar{y}_r)}}$, with $C_{exp} = \frac{\bar{A}_2^{(r-1)}}{A_i^{(r-1)}}$ and $C_p = \frac{A_{4i}^{(r-1)}}{A_i^{(r-1)}}$, where $A_i^{(r-1)}$ indicates the incident wave amplitude at the point $(r-1)$ that generated the wave amplitudes $\bar{A}_2^r$ and $\bar{A}_{4i}^r$, written at the point $(r-1)$ respectively by $\bar{A}_2^{(r-1)}$ and $A_4^{(r-1)}$. In addition, $\bar{x}_r = x_r - x_{r-1}$, $\bar{y}_r = y_r - y_{r-1}$ and $\bar{k}_x^d = \sqrt{(\bar{k}_x^d)^2 + (k_y^d)^2}$.

Consider the case of cross-section change increasing along the y direction and a flexural wave (A_{3i}^s) incidence, which propagates in the x positive and y negative directions. The influences of an attenuating wave in the x negative direction and flexural waves propagating along the cross-section change are considered, as shown in Figure 26(a). The point s coordinates are (x_s, y_s), in which transmitted (A_3^s) and reflected (A_4^s) flexural waves are generated, and the wave amplitudes A_1^s and A_2^s propagate in the y positive direction, but attenuating respectively in the x negative and positive directions. Also, at the point s, there are the wave amplitudes $\tilde{A}_1^s$ and $\tilde{A}_2^s$ propagating in the y positive direction, but attenuating in the negative and positive directions of x, which are generated at a point with x coordinate equal to point s, but y coordinate less than point s. Amplitude $\bar{A}_1^s$ corresponds to the wave amplitude that propagates in the y positive direction and attenuates in the x negative direction, which is generated at the point $(s-1)$ with coordinates (x_{s-1}, y_{s-1}), such that $x_{s-1} > x_s$ and $y_{s-1} \leq y_s$.

Figure 26 – (a) Thin plate with symmetrical cross-section change reduction along the y direction if a flexural wave with amplitude A_{3i}^s is incident at the point s. At the same point, the effects of attenuating wave $\bar{A}_1^s$ in the x negative direction and propagating waves along the y directions are considered. (b) Thin plate with cross-section change increasing along the y direction and the amplitudes generated due to flexural wave incidence with amplitude A_{4i}^t at the point t, in addition to presence of attenuating wave in the x positive direction $(\bar{A}_2^t)$ and propagating waves along the cross-section change.

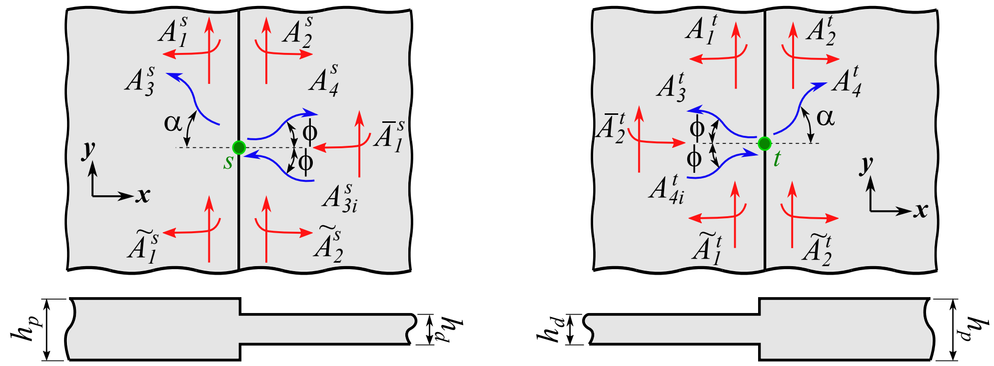

(a) (b)

Source: elaborated by the author.

At the point s, $\mathbf{h}_d^s = \mathbf{h}_p^s$, where $\mathbf{h}_d^s = \mathbf{H}_d \mathbf{a}_d^s$ and $\mathbf{h}_p^s = \mathbf{H}_p \mathbf{a}_p^s$, such that $\mathbf{a}_p^s = \{\check{A}_1^s\ 0\ A_3^s\ 0\}^T$ and $\mathbf{a}_d^s = \{\bar{A}_1^s\ \check{A}_2^s\ A_{3i}^s\ A_4^s\}^T$. In this case, $\check{A}_1^s = A_1^s + \tilde{A}_1^s$ and $\check{A}_2^s = A_2^s + \tilde{A}_2^s$. Based on these equations, it is possible to obtain $\mathbf{a}_{out} = \mathbf{Z}_{ii}\mathbf{a}_{in}$, where $\mathbf{a}_{out} = \{\check{A}_1^s\ \check{A}_2^s\ A_3^s\ A_4^s\}^T$, $\mathbf{a}_{in} = \{\bar{A}_1^s\ 0\ A_3^s\ 0\}^T$ and $\mathbf{Z}_{ii} = [\mathbf{X}_{ii}]^{-1}\mathbf{Y}_{ii}$, such that

$$\mathbf{X}_{ii} = \left[(-\mathbf{H}_p|_1)\ \ (\mathbf{H}_d|_2)\ \ (-\mathbf{H}_p|_3)\ \ (\mathbf{H}_d|_4) \right] \tag{65}$$

$$\mathbf{Y}_{ii} = \left[(-\mathbf{H}_d|_1)\ \ (\mathbf{H}_p|_2)\ \ (-\mathbf{H}_d|_3)\ \ (\mathbf{H}_p|_4) \right]. \tag{66}$$

The coefficients for transmitted $(I_t^{s(s-1)} = A_3^s/A_{3i}^s)$ and reflected $(I_r^{s(s-1)} = A_4^s/A_{3i}^s)$ waves can be written as follows

$$I_r^{s(s-1)} = Z_{ii}^{(41)} \frac{\bar{A}_1^s}{A_{3i}^s} + Z_{ii}^{(43)} \tag{67}$$

$$I_t^{s(s-1)} = Z_{ii}^{(31)} \frac{\bar{A}_1^s}{A_{3i}^s} + Z_{ii}^{(33)}. \tag{68}$$

The amplitude ratio is given by $\frac{\bar{A}_1^s}{A_{3i}^s} = \frac{C_{exn}}{C_r} \frac{e^{+\bar{k}_x^d \bar{x}_s - ik_y^d \bar{y}_s}}{e^{i(+k_x^d \bar{x}_s - k_y^d \bar{y}_s)}}$, where $C_{exn} = \frac{\bar{A}_1^{(s-1)}}{A_i^{(s-1)}}$ and $C_r = \frac{A_3^{(s-1)}}{A_i^{(s-1)}}$, such that $A_i^{(s-1)}$ shows the wave amplitude that generates the waves with amplitudes $\bar{A}_1^{(s-1)}$ and $A_3^{(s-1)}$ at the point $(s-1)$. In addition, $\bar{x}_s = (x_s - x_{s-1})$ and $\bar{y}_s = (y_s - y_{s-1})$.

On the other hand, different effects are observed if the incident wave A_{4i}^t propagates in the x and y positive directions, and the attenuating wave that affects the interaction attenuates in x positive direction, the wave amplitude of this last one is equal to $\bar{A}_2^t$, as shown in Figure 26(b). The point t coordinates are (x_t, y_t), and the transmitted and reflected waves amplitudes are represented respectively by A_4^t and A_3^t. The wave with amplitude $\bar{A}_2^t$ is generated at a point with coordinates (x_{t-1}, y_{t-1}), where $x_t > x_{t-1}$ and $y_t \geq y_{t-1}$. The effects of the propagating waves along y direction and attenuation in the x negative $(\tilde{A}_1^t)$ and positive $(\tilde{A}_2^t)$ directions amplitudes are considered at the point t.

At the point t, $\mathbf{h}_d^t = \mathbf{h}_p^t$, where $\mathbf{h}_d^t = \mathbf{H}_d \mathbf{a}_d^t$ and $\mathbf{h}_p^t = \mathbf{H}_p \mathbf{a}_p^t$, with $\mathbf{a}_d^t = \{\check{A}_1^t \; \bar{A}_2^t \; A_3^t \; A_4^t\}^T$ and $\mathbf{a}_p^t = \{0 \; \check{A}_2^t \; 0 \; A_{4i}^t\}^T$. In this particular case, $\check{A}_1^t = A_1^t + \tilde{A}_1^t$ and $\check{A}_2^s = A_2^s + \tilde{A}_2^s$. Using these presented equations, it is obtained $\mathbf{a}_{out} = \mathbf{Z}_i \mathbf{a}_{in}$, where $\mathbf{a}_{out} = \{\check{A}_1^t \; \check{A}_2^t \; A_3^t \; A_4^t\}^T$ and $\mathbf{a}_{in} = \{0 \; \bar{A}_2^t \; 0 \; A_4^t\}^T$. Then, the transmitted $(I_t^{t(t-1)} = A_4^t / A_{4i}^t)$ and reflected $(I_r^{t(t-1)} = A_3^t / A_{4i}^t)$ wave coefficients can be determined as follows

$$I_r^{t(t-1)} = Z_i^{(32)} \frac{\bar{A}_2^t}{A_{4i}^t} + Z_i^{(34)} \tag{69}$$

$$I_t^{t(t-1)} = Z_i^{(42)} \frac{\bar{A}_2^t}{A_{4i}^t} + Z_i^{(44)} \tag{70}$$

where the amplitude ratio is given by $\frac{\bar{A}_2^t}{A_{4i}^t} = \frac{C_{exp}}{C_p} \frac{e^{-\bar{k}_x^d \bar{x}_t - ik_y^d \bar{y}_t}}{e^{i(-k_x^d \bar{x}_t - k_y^d \bar{y}_t)}}$, in which C_{exp} and C_p are computed for the point $(t-1)$, and $\bar{x}_t = x_t - x_{t-1}$ and $\bar{y}_t = y_t - y_{t-1}$.

3.3 FLEXURAL WAVE SCATTERING IN THIN PLATES WITH SYMMETRICAL DAMAGE

Similarly to Section 2.3, a local thickness reduction is considered to represent the damage, as presented in Figure 3.

3.3.1 Wave Scattering due to Oblique Incident Wave Propagating in the x and y Positive Directions

Consider the plate with a symmetrical damage described by thickness h_d, width $l_x < L_x$ and length $L_{y(d)} \leq L_y$, such that $l_x << L_{y(d)}$ - see Figure 3. In this case, damaged and undamaged sections of the plate have the same physical properties. At the point p is considered an excitation which generates flexural waves that propagate to the point q with an angle α in relation to the x axis. Due to the interaction between flexural wave and damage at the point q, a reflected flexural wave is created and it propagates to the point e. At this location is considered a circular (fictitious) sensor with radius r_L. The first reflected flexural wave packet is obtained at this point. Similarly, at the point a, and considering a sensor radius r_R, the first transmitted flexural wave packet is captured after propagating from r to a.

The transmitted flexural wave at the point q propagates to the point r with angle $\phi < \alpha$, since the propagation velocity inside the damage is different from the velocity in the healthy section. These velocities can be related to each other by using the Snell-Descartes' Law $c_d \sin(\alpha) = c_p \sin(\phi)$, where c_p and c_d are respectively the wave velocities in the healthy and damaged sections of the plate. In addition, note that $\phi = \arcsin(\sqrt{h}\sin(\alpha))$, and the relation between these angles for different h is shown in Figure 27. Note that the angle ϕ is smaller than or equal to the angle α regardless of the ratio h. At the point r is generated a reflected wave and it propagates to the point s, as illustrated in Figure 4, and the first transmitted wave packet propagates to the point a. The incident wave at the point s generates additional wave packets, including the reflected flexural wave to the left hand-side and the second transmitted wave packet that propagates to the point t. This behavior repeats to generate additional waves packets, including the second transmitted flexural wave packet that propagates to the point b - see Figure 4. Then, at the points u and v are verified the third reflected and transmitted wave packets, which respectively propagate to the points g and f of the plate.

Figure 27 – Angle ϕ in terms of α for different thickness ratio h of damages. $h = 1$ (continuous line), $h = 0.75$ (dashed line), $h = 0.5$ (dash-dotted line) and $h = 0.25$ (dotted line).

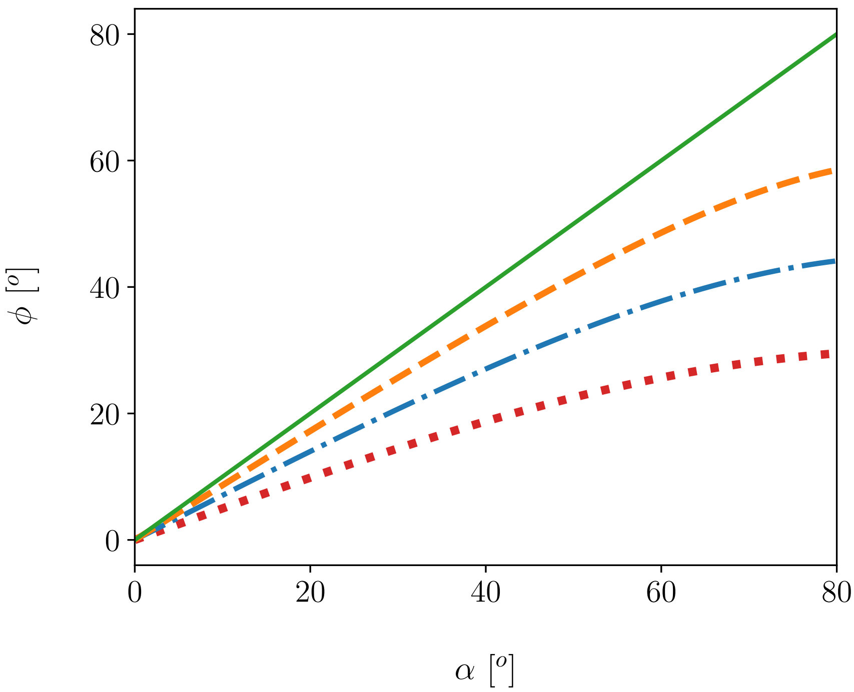

Source: elaborated by the author.

At the points r, s, t, u and v are observed additional waves besides the transmitted and reflected wave packets. At the point r, there is an effect of attenuation in the x positive direction from the point q that propagates in the y positive direction along the damage. On the other hand, at the point s there are attenuating waves created at the point q that propagate to the point s, in addition to the influence of the attenuating wave in the x negative direction generated in r and propagating in the y positive direction. Figure 28 shows a zoomed view of the damage width l_x and the corresponding waves at the points q to t with propagation angles α and ϕ, respectively outside and inside the damage. Note that $A^j_{()}$ indicates the wave amplitude at the point j, $\bar{A}^j_{()}$ is the attenuating wave amplitude generated at the previous point (considering the propagation direction) and $\tilde{A}^j_{()}$ is the propagating wave amplitude in the y direction and attenuating in the x direction. Note that this last one is created at each corresponding point below (in the y direction). In addition, A^j_r and A^j_t are respectively the flexural wave amplitudes of the reflected and transmitted wave packets at the point j.

Figure 28 – Zoomed view of the damage width and the corresponding wave amplitudes for each point q, r, s and t.

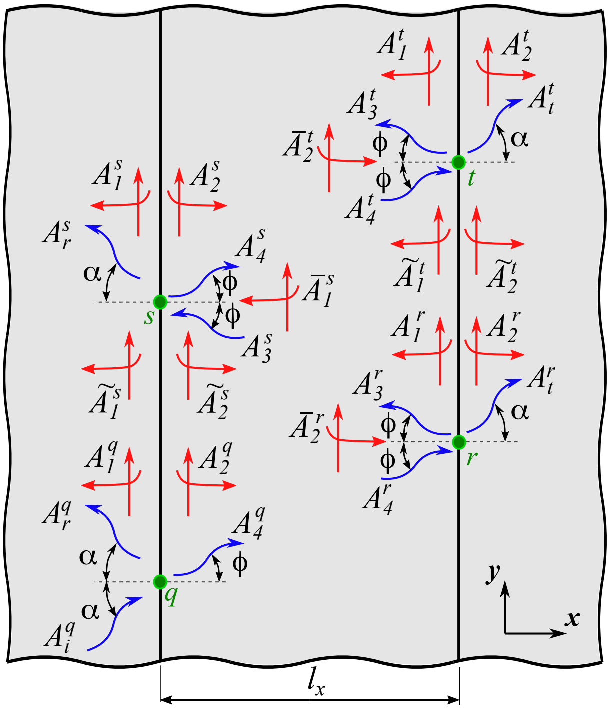

Source: elaborated by the author.

Consider the plate presented in the Figure 4 and a flexural wave generated at the point p with amplitude A_i which propagates to the point q with an angle α in relation to the x direction, the amplitude of the first wave packet that arrives at the point e is given by $\frac{A_r^e}{A_i} = \frac{A_r^e}{A_r^q}\frac{A_r^q}{A_i^q}\frac{A_i^q}{A_i}$, where $A_r^q \equiv A_3^q$ and $A_i^q \equiv A_4^q$. The ratios of amplitude $\frac{A_r^e}{A_r^q}$ and $\frac{A_i^q}{A_i}$ can be obtained by using the spatial transformation matrix elements (Equation 57), where $\frac{A_r^e}{A_r^q} = T_{2b}$ and $\frac{A_i^q}{A_i} = T_{1b}$ such that $T_{1b} = e^{i(-k_x^p d_{x1} - k_y^p d_{y1})}$ and $T_{2b} = e^{i(+k_x^p(-d_{x2}) - k_y^p d_{y2})}$. The wavenumbers k_x^p and k_y^p correspond respectively to the x and y directions. Note that they are computed by using the properties of the healthy section of the plate, where $k_x^p = k_{f(p)}\cos(\alpha)$ and $k_y^p = k_{f(p)}\sin(\alpha)$. $\frac{A_r^q}{A_i^q}$ is computed by using the coefficient R_r. Then, the flexural wave amplitude which arrives at the point a is given by

$$\frac{A_r^e}{A_i} = R_r E_1 \tag{71}$$

where $E_1 = e^{i[-k_x^p(d_{x1}+d_{x2}) - k_y^p(d_{y1}+d_{y2})]}$. The flexural wave amplitude at the point a is $\frac{A_t^{1a}}{A_i} = \frac{A_t^a}{A_t^r}\frac{A_t^r}{A_4^r}\frac{A_4^r}{A_4^q}\frac{A_4^q}{A_i^q}\frac{A_i^q}{A_i}$, where $\frac{A_t^a}{A_t^r} = T_{3b} = e^{i(-k_x^p d_{x3} - k_y^p d_{y3})}$. Similarly, $\frac{A_4^r}{A_4^q} = T_{1d}$, with $T_{1d} = e^{i(-k_x^d l_x - k_y^d l_y)}$ for $l_y = l_x \tan(\phi)$. In this case, $k_x^d = k_{f(d)}\cos(\phi)$ and $k_y^d = k_{f(d)}\sin(\phi)$, such that $k_{f(d)}$ indicates the flexural wavenumber for the damaged section of the plate. In addition, $\frac{A_t^r}{A_4^r} = I_t^{rq}$ and $\frac{A_4^q}{A_i^q} = R_t$, such that I_t^{rq} is the transmitted flexural wave coefficient of the section h_d for the section h_p considering the attenuation effect created in the previous point, and R_t is the transmitted flexural wave coefficient for a wave incidence in the section h_p of the plate. Then, the amplitude of the first transmitted wave packet is given by

$$\frac{A_t^a}{A_i} = R_t I_t^{rq} E_2 E_3 \tag{72}$$

where $E_2 = e^{i(-k_x^d l_x - k_y^d l_y)}$ and $E_3 = e^{i[-k_x^p (d_{x1}+d_{x3}) - k_y^p (d_{y1}+d_{y3})]}$.

The amplitude of the second reflected flexural wave packet at the point g is given by $\frac{A_r^f}{A_i} = \frac{A_r^2}{A_r^s}\frac{A_r^s}{A_3^s}\ \frac{A_3^s}{A_3^r}\frac{A_3^r}{A_4^r}\frac{A_4^r}{A_4^q}\frac{A_4^q}{A_i^q}\frac{A_i^q}{A_i}$, with $\frac{A_r^f}{A_r^s} = T_{2b}$ and $\frac{A_3^s}{A_3^r} = T_{2d}$, where $T_{2d} = e^{i[+k_x^d(-l_x) - k_y^d l_y]}$. $\frac{A_r^s}{A_3^s} = I_t^{sr}$ indicates the transmitted flexural wave coefficient at the point s considering incidence of a flexural wave A_3^s and influence of the attenuating wave A_1^r in the x negative direction created at the point r. $\frac{A_3^r}{A_4^r} = I_r^{rq}$ corresponds to the reflected flexural wave coefficient for flexural wave incidence at the point r and influence of attenuating wave A_2^q generated at the point q. Considering the presented relations, the amplitude ratio $\frac{A_r^{2e}}{A_i}$ is rewritten by

$$\frac{A_r^f}{A_i} = R_t I_r^{rq} I_t^{sr} E_2^2 E_1. \tag{73}$$

Similarly, the third transmitted flexural wave packet is $\frac{A_r^g}{A_i} = \frac{A_r^g}{A_r^u}\frac{A_r^u}{A_3^u}\frac{A_3^u}{A_3^t}\frac{A_3^t}{A_4^t}\frac{A_4^t}{A_4^s}\frac{A_4^s}{A_3^s}\frac{A_3^s}{A_3^r}\frac{A_3^r}{A_4^r}\frac{A_4^r}{A_4^q}\frac{A_4^q}{A_i^q}\frac{A_i^q}{A_i}$, where $\frac{A_r^g}{A_r^u} = T_{2b}$, $\frac{A_3^u}{A_3^t} = T_{2d}$ and $\frac{A_4^t}{A_4^s} = T_{1d}$. Similar to the second wave packet, $\frac{A_r^u}{A_3^u} = I_t^{ut}$, $\frac{A_3^t}{A_4^t} = I_r^{ts}$ and $\frac{A_4^s}{A_3^s} = I_r^{sr}$. Then, $\frac{A_r^g}{A_i}$ is written as follows:

$$\frac{A_r^g}{A_i} = R_t I_r^{rq} I_r^{sr} I_r^{ts} I_t^{ut} E_2^4 E_1. \tag{74}$$

The amplitude $\frac{A_t^b}{A_i}$ (point b in Figure 4) is determined by $\frac{A_t^b}{A_i} = \frac{A_t^b}{A_t^t}\frac{A_t^t}{A_4^t}\frac{A_4^t}{A_4^s}\frac{A_4^s}{A_3^s}\frac{A_3^s}{A_3^r}\frac{A_3^r}{A_4^r}\frac{A_4^r}{A_4^q}\frac{A_4^q}{A_i^q}\frac{A_i^q}{A_i}$, where $\frac{A_t^b}{A_t^t} = T_{3b}$ and $\frac{A_t^t}{A_4^t} = I_t^{ts}$, which allows one to write the following equation

$$\frac{A_t^b}{A_i} = R_t I_r^{rq} I_r^{sr} I_t^{ts} E_2^3 E_3. \tag{75}$$

In addition, the amplitude ratio $\frac{A_t^c}{A_i}$ of the third transmitted wave packet (at the point c) is given by $\frac{A_t^c}{A_i} = \frac{A_t^c}{A_t^v}\frac{A_t^v}{A_4^v}\frac{A_4^v}{A_4^u}\frac{A_4^u}{A_3^u}\frac{A_3^u}{A_3^t}\frac{A_3^t}{A_4^t}\ \frac{A_4^t}{A_4^s}\frac{A_4^s}{A_3^s}\frac{A_3^s}{A_3^r}\frac{A_3^r}{A_4^r}\frac{A_4^r}{A_4^q}\frac{A_4^q}{A_i^q}\frac{A_i^q}{A_i}$, where $\frac{A_t^c}{A_t^v} = T_{3b}$, $\frac{A_t^{3v}}{A_4^v} = I_t^{vu}$ and $\frac{A_4^v}{A_4^u} = T_{1d}$, and these equations can be rearranged to write the following equation

$$\frac{A_t^c}{A_i} = R_t I_r^{rq} I_r^{sr} I_r^{ts} I_r^{ut} I_t^{vu} E_2^5 E_3. \tag{76}$$

Based on Equations (71), (73) and (74), the amplitude ratios of the first three reflected wave packets that arrive at the points e to g are respectively given by

$$\left.\frac{A_r}{A_i}\right|_{(1)} = R_r E_1 \tag{77}$$

$$\left.\frac{A_r}{A_i}\right|_{(2)} = R_t I_r^{rq} I_t^{sr} E_1 E_2^2 \tag{78}$$

$$\left.\frac{A_r}{A_i}\right|_{(3)} = R_t I_r^{rq} I_r^{sr} I_r^{ts} I_t^{ut} E_1 E_2^4. \tag{79}$$

On the other hand, the amplitude ratios of the first three transmitted waves $\frac{A_t^1}{A_i}$, $\frac{A_t^2}{A_i}$ and $\frac{A_t^3}{A_i}$ arriving respectively at the points a to c can be written by using the Equations (72), (75) and (76), such that

$$\left.\frac{A_t}{A_i}\right|_{(1)} = R_t I_t^{rq} E_2 E_3 \tag{80}$$

$$\left.\frac{A_t}{A_i}\right|_{(2)} = R_t I_r^{rq} I_r^{sr} I_t^{ts} E_2^3 E_3 \tag{81}$$

$$\left.\frac{A_t}{A_i}\right|_{(3)} = R_t I_r^{rq} I_r^{sr} I_r^{ts} I_r^{ut} I_t^{vu} E_2^5 E_3. \tag{82}$$

Considering these equations, the n-th reflected wave packet can be determined as follows

$$\left.\frac{A_r}{A_i}\right|_{(n)} = R_t \left[\prod_{l=r}^{j} I_r^{l(l-1)}\right] I_t^{(j+1)j} E_2^{(2n-2)} E_1 \tag{83}$$

and the n-th transmitted wave packet is given by

$$\left.\frac{A_t^n}{A_i}\right|_{(n)} = R_t \left[\prod_{l=r}^{j} I_r^{l(l-1)}\right] I_t^{(j+1)j} E_2^{(2n-1)} E_3 \tag{84}$$

where n corresponds to n-th packet for $n > 1$. l and j indicate the points of the plate where there is cross-section change, such that $(j+1)$ is the point where the wave packet moves from the damaged section to the healthy section of the plate. Also, $(l-1)$ represents the point before the point l, and j the point before the point $(j+1)$.

3.3.2 Resulting Wave due to Circular Flexural Wave Propagation

Similarly to Section 2.3.2, a circular actuator creates radial wave propagation in a plate, as illustrated in Figure 29, in which an actuator placed at the point p creates radial waves with amplitude A_i in the x-y plane (SHEN; GIURGIUTIU, 2016). A circular sensor with radius r_R is placed at the point a, which captures the wave front created by the actuator for an angle range that depends on its size. The reference line indicates the direction along the centers of actuator and sensor, and it has an angle α_1 in relation to the x axis. The angle range that arrives in the sensor has the same wave amplitude, and it is used to compute the output voltage obtained by the sensor (YEUM; SOHN; IHN, 2011).

Figure 29 – Thin plate with a circular actuator placed at the point p, which is responsible to create circular waves with amplitude A_i in all the directions of the x-y plane. At the point a is placed a circular sensor of radius equal to r_R that captures the wave front with main angle α_1 in relation to the x axis.

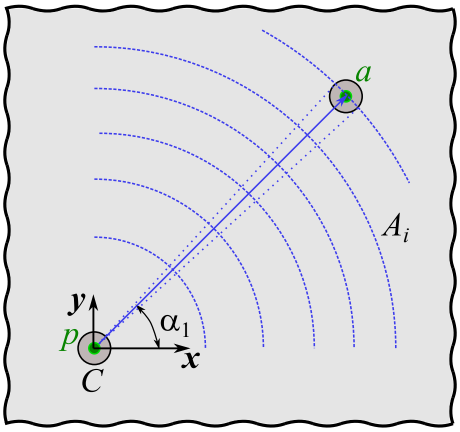

Source: elaborated by the author.

Figure 30(a) shows a thin plate with symmetrical damage of length l_x in the x direction and the first two packets of reflected and transmitted waves which propagate with angle α_1. $A_r|_{()}^{\alpha_1}$ and $A_t|_{()}^{\alpha_1}$ represent respectively wave amplitudes for the reflected and transmitted waves, where the subscripts indicate the packet number. In this case, the sensors have radii smaller than $2l_x \tan(\phi_1)$, where ϕ_1 is obtained with the Snell-Descartes's Law, which allows one to capture just the first transmitted and reflected wave packets.

For a circular actuator, the waves propagate in all directions of the x-y plane and the sensors capture waves coming from different angles, i.e., a range of angle according to their size. Figure 30(b) illustrates some directions for a circular sensor which captures the transmitted wave packets. The schematic representation shows that the sensor captures the first wave packet with amplitude $A_t|_1^{\alpha_1}$, the second wave packet $(A_t|_2^{\alpha_2})$ that propagates with angle α_2 and a third wave packet ($A_t|_3^{\alpha_3}$) that propagates with angle α_3, such that $\alpha_3 < \alpha_2 < \alpha_1$. Due to its relative low amplitude, the fourth packet can be neglected. Then, the resulting wave captured by the sensor can be accurately represented as a sum of the first three wave packets, which propagate with angles α_1, α_2 and α_3, respectively. The wave amplitudes can be computed by using Equations (80) to (82). The transmitted resulting wave captured by the sensor is obtained by Equation (85), where $A_t|_c$ is the transmitted resulting wave amplitude considering circular transducers. The angles α_1 to α_3 are determined based on the relative positions between actuator and sensor, and the following equation can be used if, and only if, $r_{()} < 2l_x \tan(\phi_1)$.

Figure 30 – (a) Thin plate with symmetrical damage of length l_x in the x axis. Points a and b are where the first and second packets of amplitudes $A_t|_1^{\alpha_1}$ and $A_t|_2^{\alpha_1}$ arrive, respectively. At the points e and f the first two reflected wave packets with amplitudes $A_r|_1^{\alpha_1}$ and $A_r|_2^{\alpha_1}$ respectively arrive. (b) Wave packets with amplitudes $A_t|_1^{\alpha_1}$. $A_t|_2^{\alpha_2}$ and $A_t|_3^{\alpha_3}$ arrive at the point a.

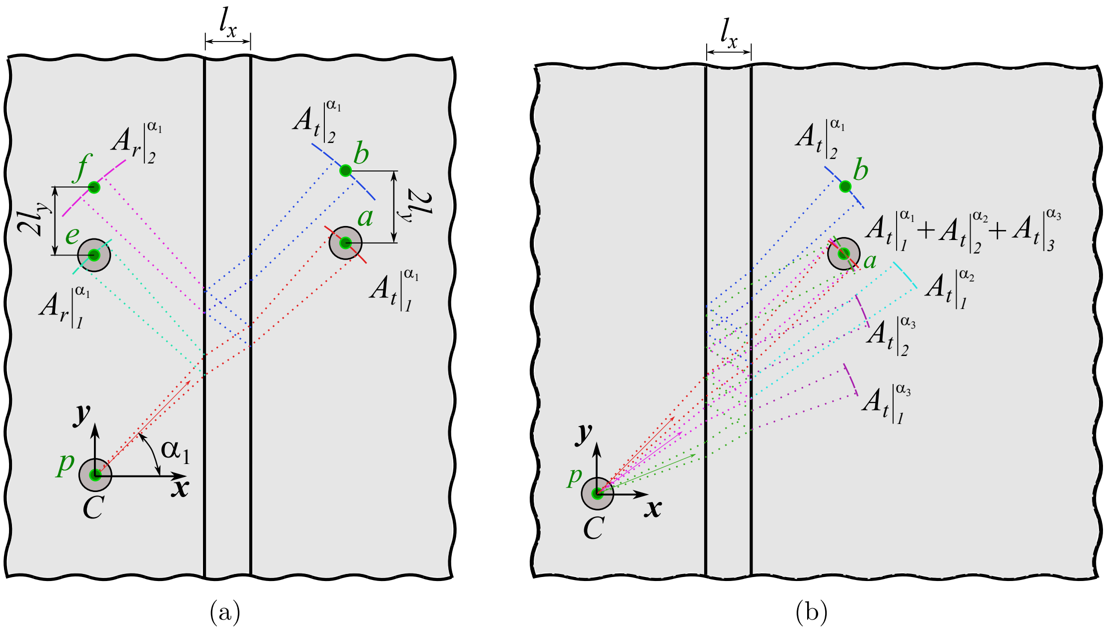

Source: elaborated by the author.

$$\left.\frac{A_t}{A_i}\right|_c = \left.\frac{A_t}{A_i}\right|_1^{\alpha_1} + \left.\frac{A_t}{A_i}\right|_2^{\alpha_2} + \left.\frac{A_t}{A_i}\right|_3^{\alpha_3}. \tag{85}$$

3.4 RESULTS AND DISCUSSION

This section presents the results to demonstrate the proposed approach. An aluminum plate with L_x = 100 cm and L_y = 100 cm is considered, such that E_p = 69 MPa, ρ_p = 2710 kg/m^3, h_p = 2 mm, l_x = 4 mm, $d_{x1} = d_{x2} = d_{x3}$ = 10 cm and ν_p = 0.33.

Figures 31(a) and 31(b) present the resulting transmitted ($|A_t/A_i|$) and reflected ($|A_r/A_i|$) wave amplitude ratios in relation to the ratio $l_x/\lambda_{f(d)}$, where $\lambda_{f(d)}$ is computed with the properties of the damaged section. These results are particular to $\alpha = 0$, and consequently $d_{y1} = d_{y2} = d_{y3} = 0$. The first peaks and valleys for which the variations in wave amplitude ratios are highest and verified for $\frac{l_x}{\lambda_{f(d)}} = \frac{h}{4}$. The other peaks and valleys are obtained for $\frac{l_x}{\lambda_{f(d)}} = \frac{6p-7+4h}{12}$ ($p = 2,\ 3,\ 4, \ldots$). Based on these equations, the optimal frequencies to detect symmetrical damage using flexural waves with perpendicular incidence are determined, such that their value for the first peaks and valleys is equal to $f_{opt}^{f} = \frac{\pi h^2 h_d}{8 l_x^2}\sqrt{\frac{E_d}{12\rho_d(1-\nu_d^2)}}$ Hz, and $f_{opt}^{f} = \frac{\pi(6p-7+4h)^2 h_d}{72 l_x^2}\sqrt{\frac{E_d}{12\rho_d(1-\nu_d^2)}}$ (in Hertz) for the others, where superscript p indicates the peak or valley number. Figures 31(a) and 31(b) show that the amplitude variations obtained for the reflected waves at these frequencies are higher than those for the transmitted waves. This result confirms that the pulse-echo configuration is a more interesting strategy to detect damage in this considered condition.

Figure 31 – Magnitude of the (a) transmitted ($|A_t/A_i|$) and (b) reflected ($|A_r/A_i|$) wave amplitude ratios obtained for different damage depth in relation to the ratio $l_x/\lambda_{f(d)}$, where: $h = 1$ (continuous line), $h = 0.5$ (dotted line), $h = 0.7$ (dash-dotted line) and $h = 0.8$ (dashed line). $\alpha = 0$.

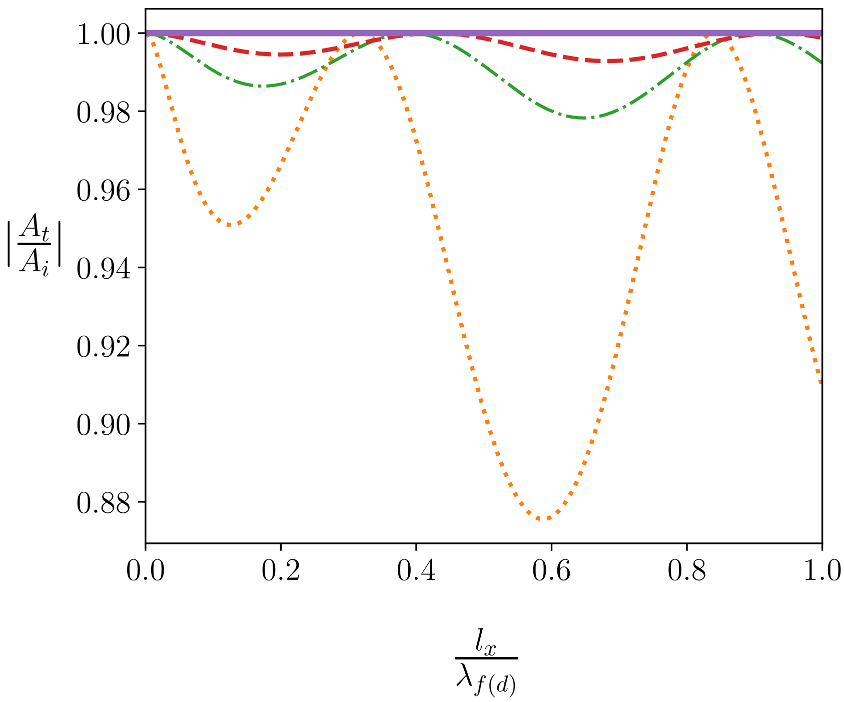

(a)

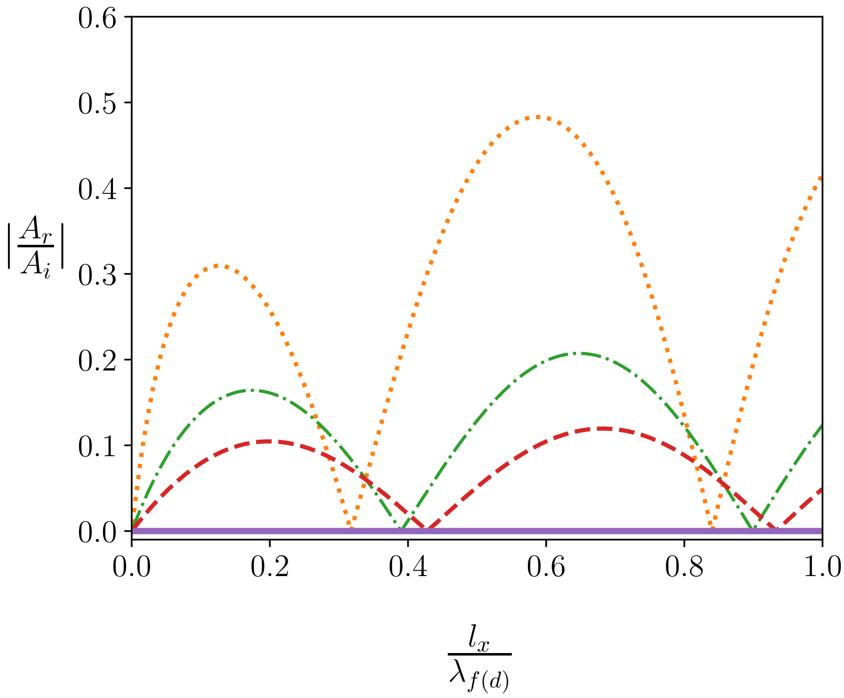

(b)

Source: elaborated by the author.

If the actuator is not horizontally aligned with the sensor S_r and vertically distant from the sensor S_l, the vertical distances d_{y1}, d_{y2} and d_{y3} are not zero and the angle is $\alpha \neq 0$, and the sensors capture different wave packets according to their sizes. Figures 32 and 33 respectively show the reflected and transmitted wave amplitudes for two different values of α considering two sensors sizes. Note that there is a change in the optimal frequencies in relation to α, which demonstrates the importance of strategically choosing the relative position between actuator and sensors. In addition, note that for low damage depth, the influence of the third wave packet is low for both transmitted and reflected waves, that is, the resulting wave amplitudes are approximately equal to the sum of the first two wave packets for low damage depths.

Figure 32 – Magnitude of the reflected wave amplitude ratio obtained for $2l_x \tan(\phi) \leq r_L < 4l_x \tan(\phi)$ (continuous line) and $4l_x \tan(\phi) \leq r_L < 6l_x \tan(\phi)$ (dotted line): (a) $\alpha = 30°$ and (b) $\alpha = 15°$. The symbol $\times$ indicates $l_x/\lambda_{f(d)}$ for the optimum frequencies f^f_{opt}.

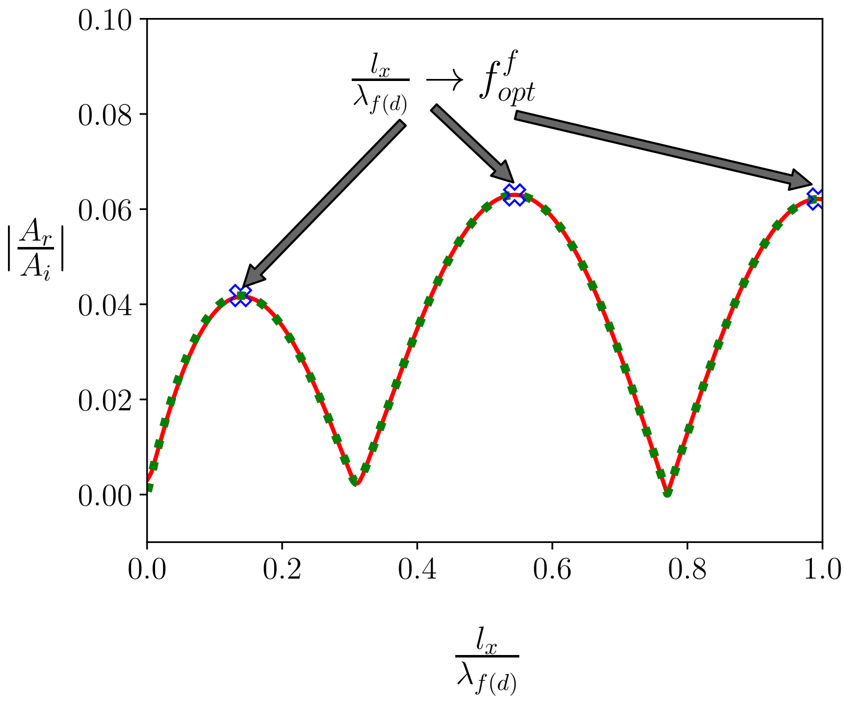

(a) $\alpha = 30°$

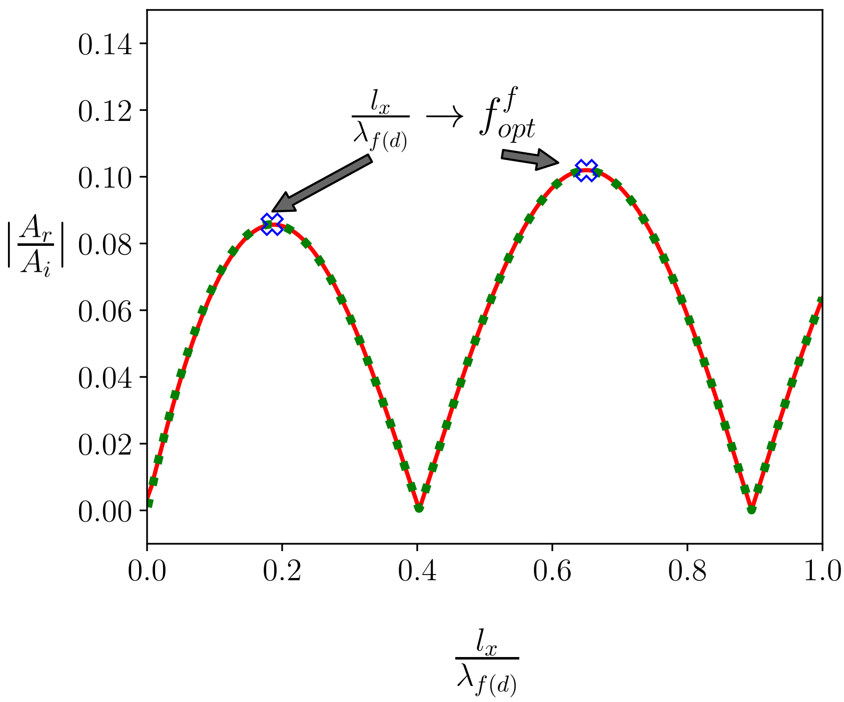

(b) $\alpha = 15°$

Source: elaborated by the author.

Figure 33 – Magnitude of the transmitted wave amplitude ratio obtained for $2l_x \tan(\phi) \leq r_R < 4l_x \tan(\phi)$ (continuous line) and $4l_x \tan(\phi) \leq r_R < 6l_x \tan(\phi)$ (dotted line): (a) $\alpha = 30°$ and (b) $\alpha = 15°$. The symbol × indicates $l_x/\lambda_{f(d)}$ for the optimum frequencies f^f_{opt}.

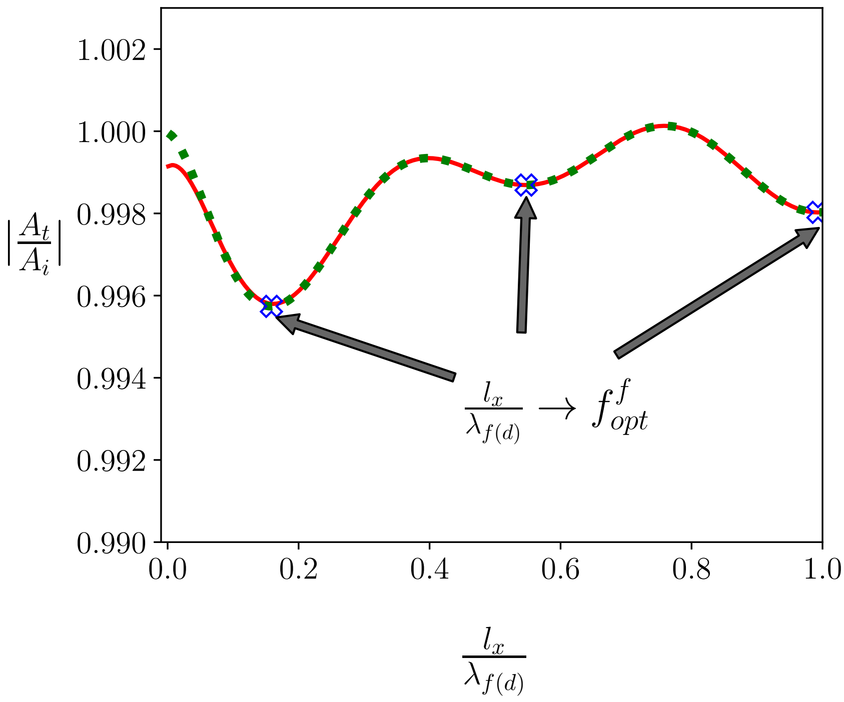

(a) $\alpha = 30°$

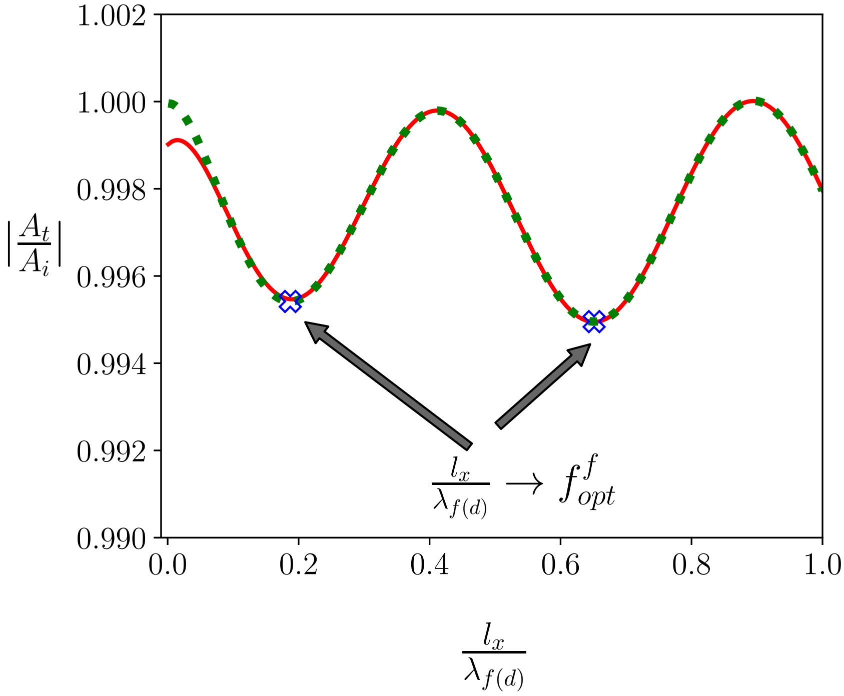

(b) $\alpha = 15°$

Source: elaborated by the author.

Figures 34(a) and 34(b) show the ratios $l_x/\lambda_{f(d)}$ corresponding to the first two peaks of the resulting reflected wave amplitude ratios, which are computed for a sensor with radius $4l_x \tan(\phi) \leq r_L < 6l_x \tan(\phi)$ in relation to α for three different values of h. These results show that the corresponding optimal frequencies change in terms of the incidence angle α. Figure 34(a) shows that the optimal frequencies decrease for $\alpha < 50^o$ until achieving the valley near $\alpha = 50^o$. Similar results are obtained for the second peak and the first valley of the resulting transmitted wave amplitude ratio, as shown in Figures 34(b) and 34(c). Then, the use of an angle $\alpha < 50^o$ contributes to consider higher frequencies in the type of damage detection.

Figure 34 – Ratio $\frac{l_x}{\lambda_{f(d)}}$ obtained for the optimal frequencies of the (a) first and (b) second peaks of the resulting reflected wave amplitude ratio and (c) for the optimal frequencies of the first valley of the resulting transmitted wave amplitude ratio considering $4l_x \tan(\phi) \leq r_L < 6l_x \tan(\phi)$ as a function of α for different values of h, where $h = 0.7$ ($\triangledown$), $h = 0.8$ ($\square$) and $h = 0.9$ ($\circ$).

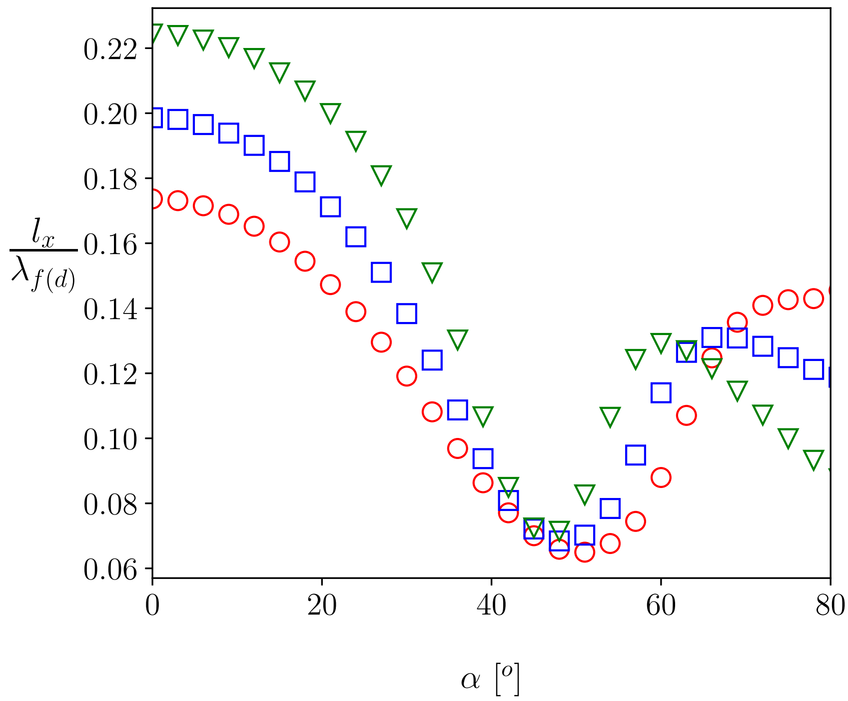

(a)

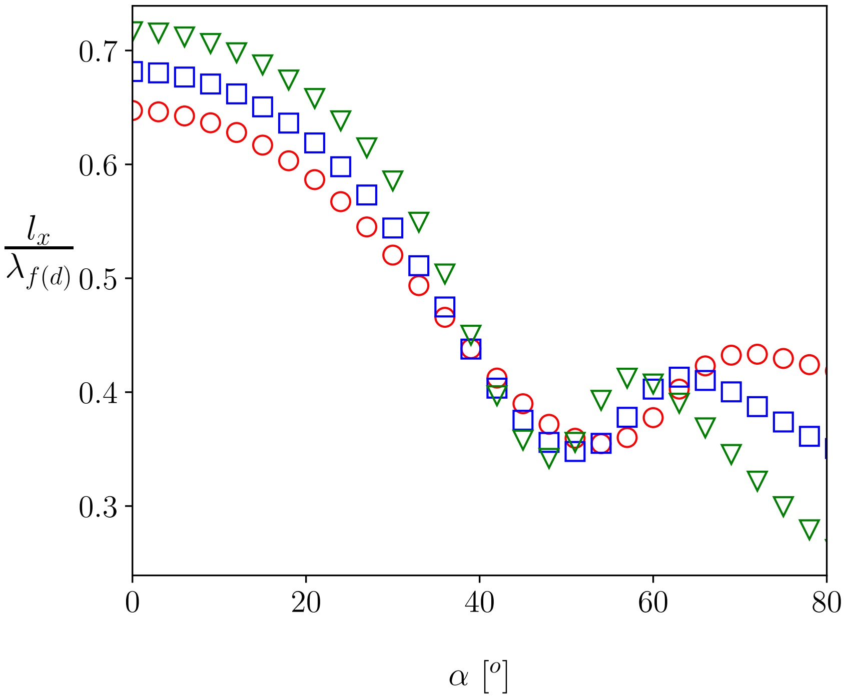

(b)

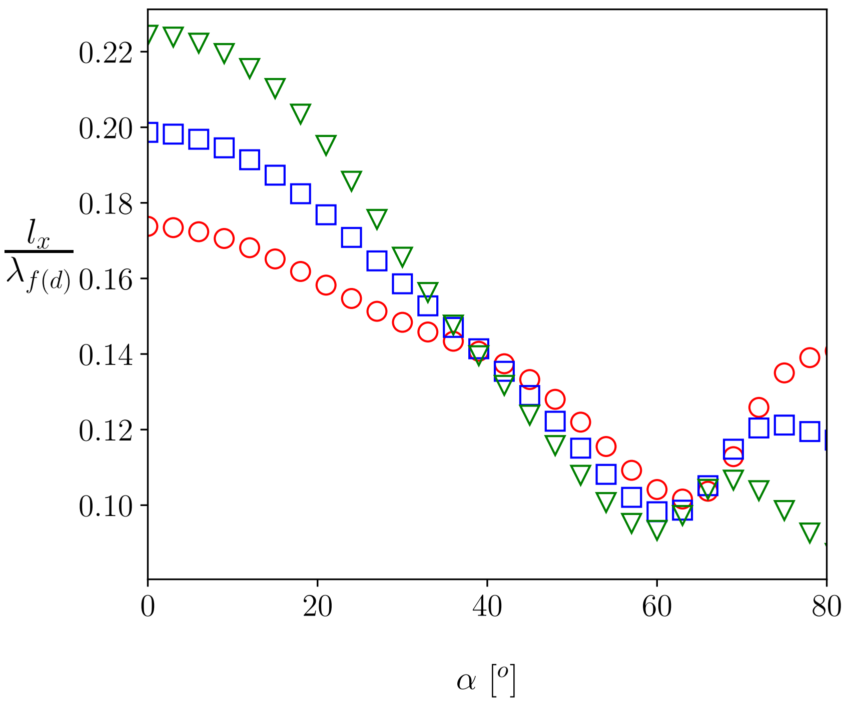

(c)

Source: elaborated by the author.

3.4.1 EXPERIMENTAL TESTS

Experimental tests are carried out by considering the aluminum plate previously presented in Section 2.5. Figure 35 presents a schematic view and photographs of the experimental setup. Two circular piezoelectric transducers (type disc bender with ceramic diameters equal to 19.4 mm and overall thickness of 0.45 mm) are coupled to the surface of the plate. Piezoelectric C works as actuator and S as sensor. The input signal is generated by the NI USB 6353 from National Instruments coupled to a power amplifier EL 1225 from Mide QuicPack. An oscilloscope DSO7034B from Keysight is used to measure the signals from the transducers, and the input signal is a 5 cycles tone burst.

Similarly to Section 2.5, the symmetrical damage is created in the plate by conveniently considering an equivalence in terms of the damage effect on the propagating waves and of defining the optimal frequencies. The final changed section, which corresponds to the damaged region of the plate, is described by equivalent properties, such that $E_d = E_{eq} = 69.7$ MPa and $\rho_d = \rho_{eq} = 2636.67$ kg/m^3 (see Section 2.5 for details).

Figure 35 – (a) Schematic view and (b) photographs of the experimental setup (dimensions in cm).

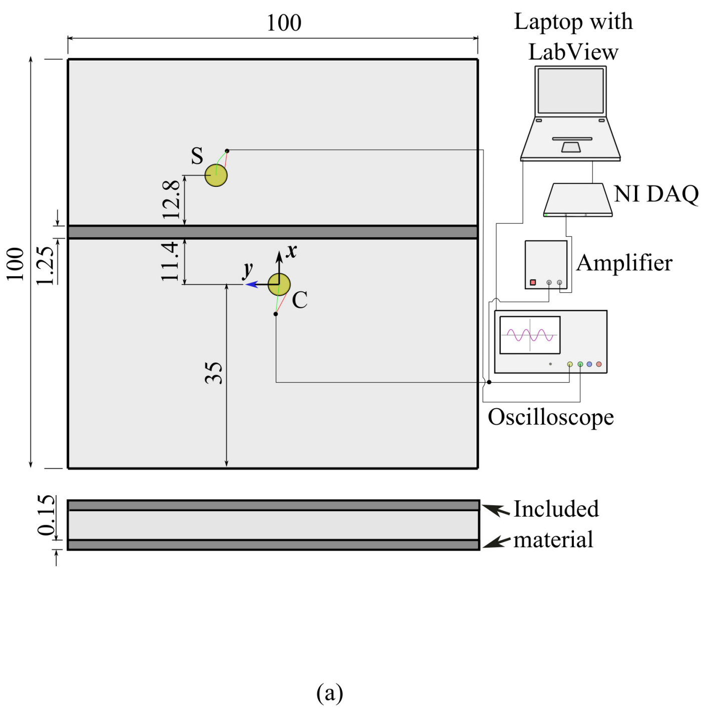

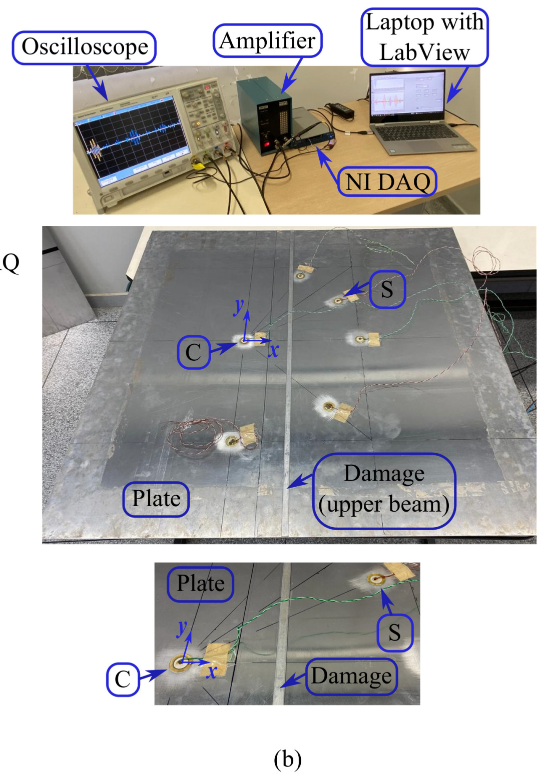

Source: elaborated by the author.

The circular actuator creates radial flexural waves radially in the plate, as presented in section 3.3.2. Considering the geometric center of the actuator as origin of the coordinate system, as presented in Figure 35, it is obtained $\alpha_1 = 28^o$, $\alpha_2 = 24.8$ and $\alpha_3 = 21.5^o$. These angles are obtained from the corresponding drawing using a software CAD. The sensor S radius is $r_S = 9.7$ mm and the damage length is $l_x = 12.5$ mm. Then, this sensor captures the first wave packet coming from the actuator for α_1 ($r_S < 2l_x \tan(\phi_1^{(S)}) = 33.64$ mm). In addition, the sensor captures the second and third wave packets propagating with α_2 and α_3, and then the resulting wave can be approximately determined through Equation (40). Figure 36 presents the index $\bar{R}$ computed from the experimental data and show it in comparison with the theoretical transmitted resulting wave (Equation 84) when the three first wave packets are summed for α_1, and for the transmitted resulting wave (Equation 85) for α_1 to α_3. Note that there is an interesting agreement between experimental and theoretical results. The experimental results are shown in Figure 36 using box plots. Each box is obtained by considering seven measured signals, and higher accuracy is verified at the frequencies 140 kHz ($l_x/\lambda_{f(p)} = 1.23$), 150 kHz ($l_x/\lambda_{f(p)} = 1.27$), 160 kHz ($l_x/\lambda_{f(p)} = 1.31$) and 170 kHz ($l_x/\lambda_{f(p)} = 1.35$) in comparison with the higher frequencies 230 kHz ($l_x/\lambda_{f(p)} = 1.57$) and 240 kHz ($l_x/\lambda_{f(p)} = 1.61$).

Figure 36 – $\bar{R}$ index obtained for: experimental data (box plot), transmitted resulting wave when the first three wave packets are summed considering $\alpha = 28^o$ (dashed line) and for radial wave propagation with Equation (40) for $\alpha_1 = 28^o$, $\alpha_2 = 24.8^o$ and $\alpha_3 = 21.5^o$ (continuous line).

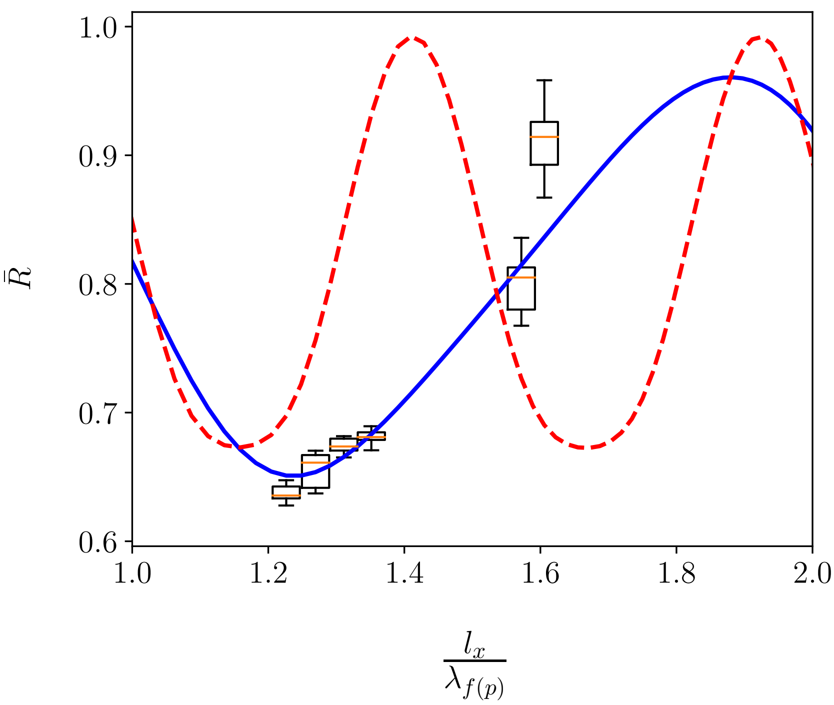

Source: elaborated by the author.

Figure 37 presents $\bar{R}$ computed for both configurations considering as reference one signal for each frequency. The limit value is $\bar{R}_l = 0.95$, which is equal to the lower value obtained for the plate without damage. The (blue) boxes are above the limit values, which indicates a threshold line, and they are close to the value 1. On the other hand, the (red) boxes are below the threshold line. The indexes obtained for $l_x/\lambda_{f(p)} = 1.61$ and $l_x/\lambda_{f(p)} = 1.57$ are bigger than those indexes obtained for the frequencies close to the optimal frequency (as shown in Figure 36). Figures 38 and 39 show the flexural waves collected using the sensor S for healthy and damaged plate, respectively. In both cases, a tone burst of 5 cycles and center frequency of 150 kHz is used. Figure 40 presents the magnitude of these signals in the frequency domain. These results demonstrate that the optimal frequencies are the most interesting choice to detect this type of damage. Lopes *et al.* (2022) noted that the optimal frequencies obtained for symmetrical damages are similar to those observed for asymmetrical damages with same damage severity when considering plate-like structures and perpendicular incidence of flexural wave, specially in the cases of low damage depth, even with the presence of longitudinal waves that are generated due to the damage asymmetry. Then, the approach proposed herein can also be applied in SHM applications involving damage detection with small asymmetry.

Figure 37 – $\bar{R}$ index calculated for: healthy (blue boxes) and damaged (red boxes) plates. Dashed line represents the threshold $\bar{R}_l = 0.95$.

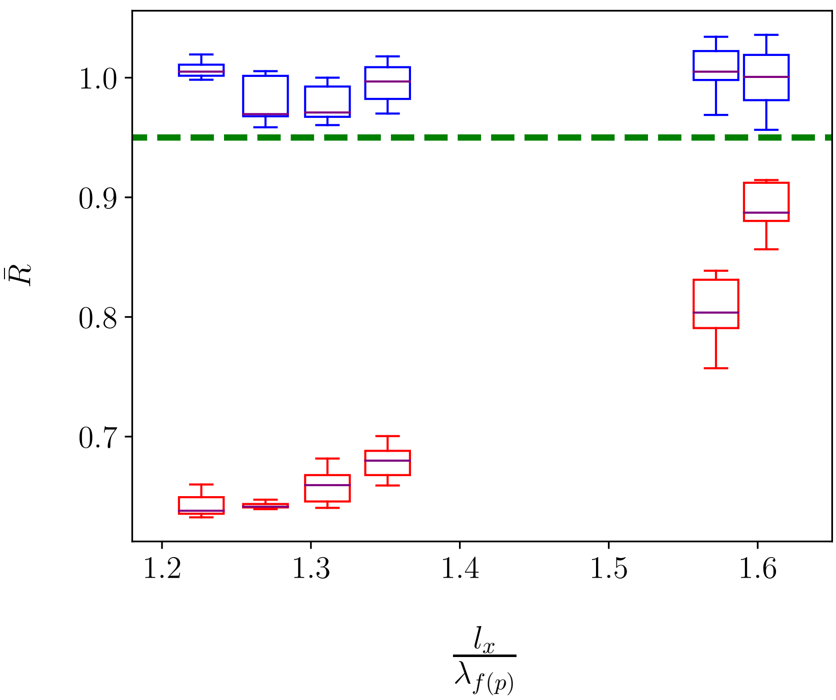

Source: elaborated by the author.

Figure 38 – Flexural waves in the time domain collected for structure without symmetrical damage using the sensor S considering as input a tone burst of 5 cycles and center frequency of 150 kHz.

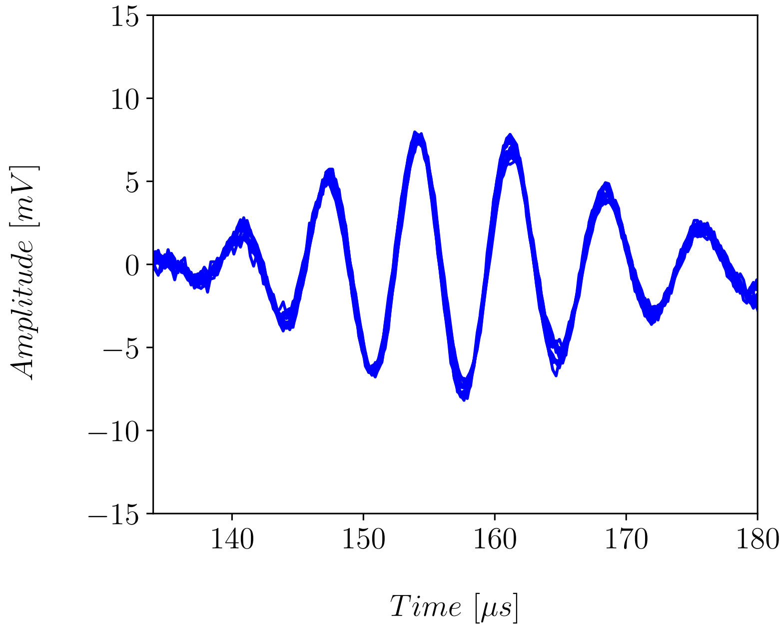

Source: elaborated by the author.

Figure 39 – Flexural waves in the time domain collected for structure with symmetrical damage using the sensor S considering as input a tone burst of 5 cycles and center frequency of 150 kHz.

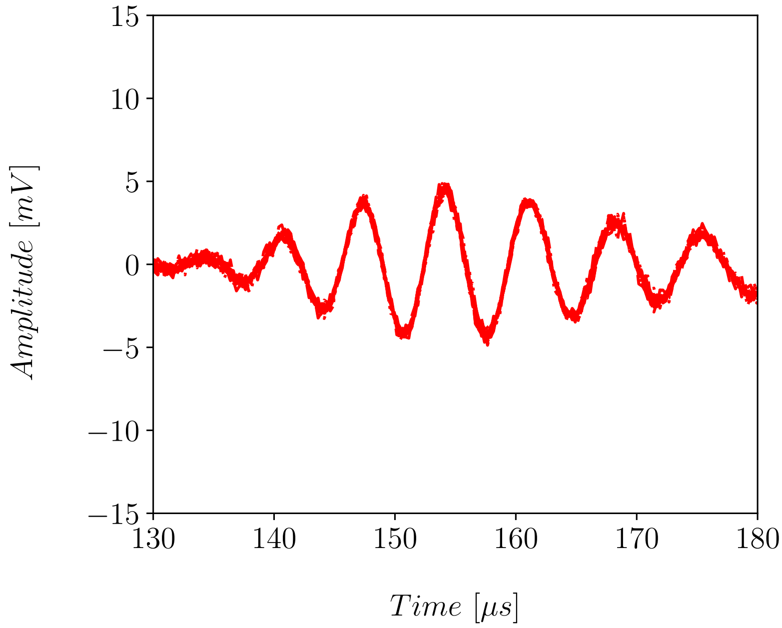

Source: elaborated by the author.

Figure 40 – Magnitude in the frequency domain of the signals collected for healthy (continuous lines, from Fig. 18) and damaged (dash-dotted lines, from Figure39) plate using the sensor S2, considering as input a tone burst of 5 cycles and center frequency of 150 kHz.

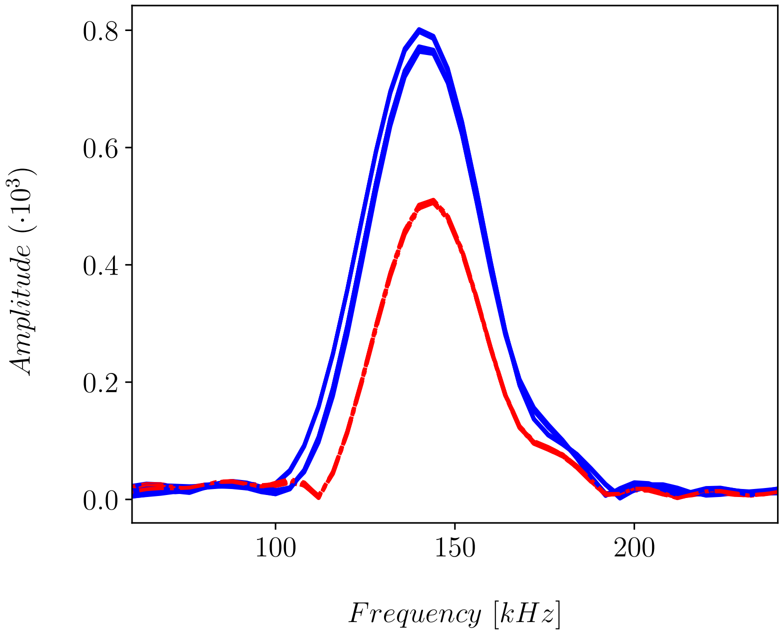

Source: elaborated by the author.

3.5 FINAL REMARKS

This chapter presented an investigation into the scattering of flexural waves in plates with symmetric damage. A model was presented to describe each wave packet for the transmitted and reflected flexural waves considering an oblique incidence in the damaged section. It is demonstrated that the incidence angle affects the wave amplitudes and the optimal frequencies of both transmitted and reflected resulting waves.

The results show that the number of packets captured by the sensors depends on the length of the damage l_x and the radius of the sensor $r_{()}$. If $r_{()} < 2l_x \tan(\phi)$, where ϕ is the angle of wave propagation inside the damage, sensors capture just the first wave packets. However, if $2l_x \tan(\phi) \leq r_{()} < 4l_x \tan(\phi)$, the resulting waves obtained by the sensors correspond to the sum of the first two wave packets. Then, there is an effect of the incidence angle on the resulting waves, changing the wave amplitudes and the optimal frequencies. if the sensors radii are $4l_x \tan(\phi) \leq r_{()} < 6l_x \tan(\phi)$, the resulting wave is composed of the first three wave packets, but the final result is similar to that one obtained for $2l_x \tan(\phi) \leq r_{()} < 4l_x \tan(\phi)$. This finding shows a lower influence of the third wave packet for small damage depth.

Experimental tests were carried out on an aluminum plate to demonstrate the proposed methodology considering radial wave propagation with circular actuator and sensor. The results show that the resulting wave can be approximately determined through the sum of the first wave packet propagating with angle α_1, the second wave packet with angle α_2 and the third wave packet obtained for α_3, where $\alpha_1 > \alpha_2 > \alpha_3$, if the sensor radius is equal to $r_{()} < 2l_x \tan(\phi_1)$. Therefore, considering circular wave, the resulting wave is determined by different wave packets coming from different angles according to the relative position between actuator, damage and sensor. Based on experimental data, the damage can be determined by using the proposed index $\bar{R}$, which represents a ratio between the maximum amplitude obtained for signal measured for an unknown structural condition in the frequency domain, and another one for the baseline condition. Using the data obtained for undamaged plate with sensor S from Figure 35, the threshold $\bar{R}_l = 0.95$ is determined. However, further researches can be done to investigate how the best strategies to define the threshold to avoid false alarms in terms of damage detection.

4 CIRCULAR PIEZOELECTRIC TRANSDUCERS FOR SHM

This chapter investigates longitudinal and flexural waves for applications using circular piezoelectric transducers bonded to thin plates. The methodology allows one to obtain optimal frequencies to create and capture both types of waves and understand the influence of the geometric characteristics of these transducers on the damage detection. Numerical simulations are carried out to show that a change in the parameters of the piezoelectric transducers can maximize the waves amplitudes incoming at the sensor. Results from experimental tests are presented to demonstrate the proposed methodology. New equations are introduced and they compute output voltage and determine optimal frequencies to monitor the structure. The findings contribute to establishing a more efficient design of a damage detection process involving plate-like structures in SHM systems based on wave propagation.

According to Raghavan and Cesnik (2005), radial waves can be created in plates, which propagate with the same amplitude A_r for all directions of the plate, as illustrated in Figure 41. The displacements for longitidunal and flexural waves can be written as follows

$$u_r(r,\omega) = A_l e^{-ik_l r} \quad \text{and} \quad w_r(r,\omega) = A_f e^{-ik_f r} \tag{86}$$

where u_r is the radial displacement for longitudinal wave and w_r the radial transversal displacement for flexural wave. A_l and A_f indicate the longitudinal and flexural wave amplitudes for radial wave propagation, respectively. $r = \sqrt{x^2 + y^2}$ is the radius in relation to the source of waves.

Figure 41 – Thin plate with circular piezoelectric transducer generating a radial wave with amplitude A_r in all directions.

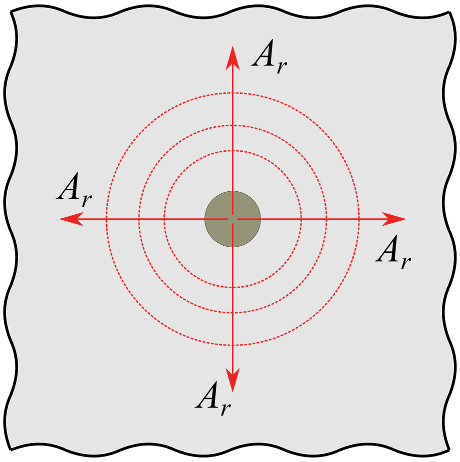

Source: elaborated by the author.

For longitudinal wave propagation, the line radial force is given by (GIURGIUTIU, 2014b)

$$F_r(r,\omega) = \frac{E_p h_p}{(1-\nu_p^2)} \left(\frac{du_r(r,\omega)}{dr} + \nu_p \frac{u_r(r,\omega)}{r} \right). \tag{87}$$

Due to the flexural wave propagation, a radial bending M_r is generated in the middle plane of plate, and it is given by (GIURGIUTIU, 2014b; UGURAL, 2017)

$$M_r(r,\omega) = -D_p \left(\frac{d^2 w_r(r,\omega)}{dr^2} + \nu_p \frac{dw_r(r,\omega)}{dr} \right). \tag{88}$$

Longitudinal and flexural waves correspond to the in-plane and out-of-plane vibrations of the plate, and they are related to the distribution of the displacement along the plate thickness. For the longitudinal wave, the displacements are uniform along the thickness. On the other hand, a linear distribution of the displacement across the thickness of the plate is considered for flexural wave propagation (GIURGIUTIU, 2014a). For a low-frequency range and a thin plate, they respectively correspond to the S_0 and A_0 Lamb Wave modes, as presented by Giurgiutiu (2014c).

4.1 CIRCULAR PIEZOELECTRIC TRANSDUCER BONDED TO THE PLATE

Consider circular piezoelectric transducers to create and capture waves in a SHM application. The input voltage $V_{in}(\omega)$ applied to the circular piezoelectric transducer (actuator) bonded to the plate creates a wave in the host structure with amplitude A_r

and it is captured at a point where a circular piezoelectric sensor is placed on the plate. Due to the direct piezoelectric effect, the wave amplitude is converted to the output voltage $V_{out}(\omega)$ at the sensor, and the measured signal is used to evaluate the structural condition in terms of damage detection. Figure 42 illustrates the host plate and the described process. Additional details are presented in Figure 43, in which F_a is the line force applied on the plate by the PZT actuator and M_a is the bending moment created due to the applied force. According to Giurgiutiu (2014d), when a circular PZT is bonded to a plate, the stress-strain relations in cylindrical coordinates are given by

$$\begin{aligned}\sigma_r^a(r,\omega) &= \frac{E_a}{1-\nu_a^2}\left(\frac{du_a(r,\omega)}{dr}+\nu_a\frac{u_a(r,\omega)}{r}\right)-\frac{(1+\nu_a)}{1-\nu_a^2}E_a\varepsilon_{ISA}\\ \sigma_\theta^a(r,\omega) &= \frac{E_a}{1-\nu_a^2}\left(\nu_a\frac{du_a(r,\omega)}{dr}+\frac{u_a(r,\omega)}{r}\right)-\frac{(1+\nu_a)}{1-\nu_a^2}E_a\varepsilon_{ISA}\end{aligned} \tag{89}$$

where ε_{ISA} is the induced strain equal to $\varepsilon_{ISA} = -(d_{31}^a V_{in})/h_a$ and σ_r^a and σ_θ^a are the stresses of the actuator. Considering the stress σ_r^a, it is possible to obtain the line radial force with the following equation $F_a = \int_0^{h_a}\sigma_r^a dz$, which allows one to write the following equations

$$F_r^l(r,\omega) = \frac{E_a h_a}{1-\nu_a^2}\left(\frac{du_a(r,\omega)}{dr}+\nu_a\frac{u_a(r,\omega)}{r}\right)+\frac{(1+\nu_a)}{1-\nu_a^2}E_a d_{31}^a V_{in} \tag{90}$$

$$F_r^f(r,\omega) = -\frac{E_a h_a^2}{2(1-\nu_a^2)}\left(\frac{d^2w_a(r,\omega)}{dr^2}+\frac{\nu_a}{r}\frac{dw_a(r,\omega)}{dr}\right)+\frac{(1+\nu_a)}{1-\nu_a^2}E_a d_{31}^a V_{in} \tag{91}$$

where F_r^l and F_r^f are the line radial forces obtained for longitudinal and flexural wave propagation, respectively. If the actuator has radius r_a, this force for longitudinal wave is given by Equation (92). This consideration of force applied to the edge of the actuator is associated to the pin-force model presented in different works, such as Xu and Giurgiutiu (2007), Yu *et al.* (2008), Ende and Lammering (2009), Huang, Song and Wang (2010), Lin and Giurgiutiu (2012) and Shen and Giurgiutiu (2014). It depends on the bonding condition between piezoelectric transducer and host structure. Giurgiutiu (2005) introduces that a thin bonding layer of high stiffness between the piezoelectric transducer and host structure produces a concentration of force over the infinitesimal area of the PZT ends and the ideal bonding between PZT and structure can be employed. However, if the thickness of the bonding layer increases, the transfer of the interfacial shear is observed over the span of the PZT, besides the PZT ends. However, for these cases, Santoni *et al.* (2007) indicate that a shorter length of the PZT by percentage can be employed to consider the pin-force model. Despite its simplicity, the pin-forced model has been compared to other models and it has presented good accuracy, mainly for high shear modulus of the bonding layer and low excitation frequencies, as shown by Yu, Bottai-Santoni and Giurgiutiu (2010) and Kapuria and Agrahari (2018).

Figure 42 – Frontal view of circular piezoelectric transducers bonded to the plate and working as actuator and sensor. The V_{in} is applied to the actuator, generating a wave with amplitude A_r that propagates to the sensor, which obtains the output voltage V_{out}.

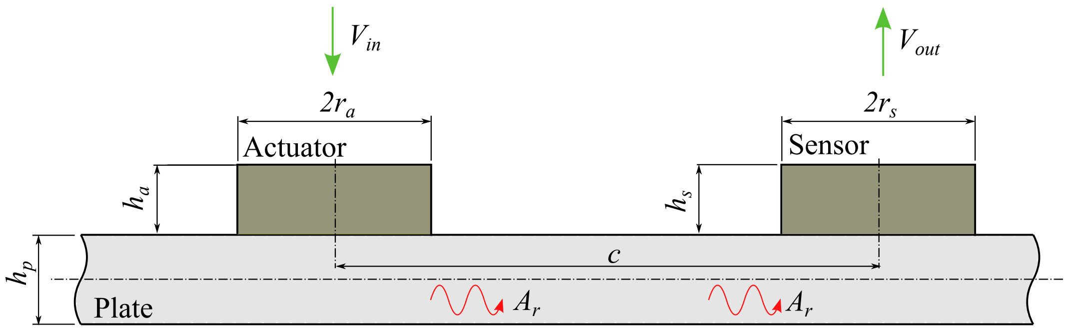

Source: elaborated by the author.

Figure 43 – Forces and moments applied to the plate due to the coupling between a circular piezoelectric transducer and the host structure when an input voltage V_{in} is applied.

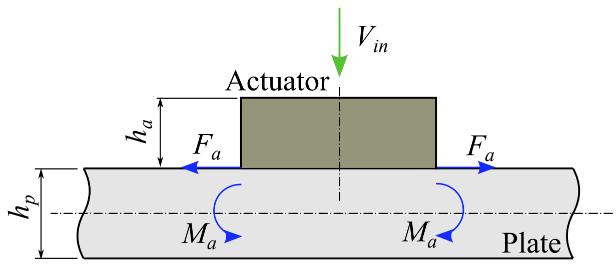

Source: elaborated by the author.

$$F_a^l(r = r_a, \omega) = \frac{E_a h_a}{(1 - \nu_a^2)} \left(\frac{du_a(r_a, \omega)}{dr} + \nu_a \frac{u_a(r_a, \omega)}{r} \right) + \frac{(1 + \nu_a)}{1 - \nu_a^2} E_a d_{31}^a V_{out} \tag{92}$$

where d_{31}^a is the induced strain coefficient of the actuator, $u_a(r_a, \omega)$ is the radial displacement of the circular piezoelectric transducer edge for longitudinal wave propagation, E_a is the Young's modulus, ρ_a is the density material and ν_a is the Poison's coefficient of the actuator.

In addition, the radial bending $M_a(r_a, \omega)$ for the flexural wave propagation is given by $M_a(r_a, \omega) = \frac{h_p}{2} F_a^f(r_a, \omega)$, where $F_a^f(r_a, \omega)$ is given by Equation (91) for $r = r_a$. Note that $u_a(r_a, \omega) = u_r(r_a, \omega)$ and $w_a(r_a, \omega) = w_r(r_a, \omega)$ can be considered due to the mechanical coupling between the circular PZT and the plate. Considering the displacements from

Equation (86), it is possible to obtain the following equations

$$F_a(r_a,\omega) = \frac{E_a h_a}{(1-\nu_a^2)}\frac{A_l}{r_a}e^{-ik_l r_a}(\nu_a - ik_l r_a) + \frac{(1+\nu_a)}{1-\nu_a^2}E_a d_{31}^a V_{in} \tag{93}$$

$$M_a(r_a,\omega) = \frac{h_p}{4r_a}\frac{E_a h_a^2}{(1-\nu_a^2)}k_f A_f e^{-ik_f r_a}(k_f r_a + i\nu_a) + \frac{h_p}{2}\frac{(1+\nu_a)}{(1-\nu_a^2)}E_a d_{31}^a V_{in}. \tag{94}$$

Then, the wave amplitudes for longitudinal and flexural wave radial propagation can be determined in terms of the input voltage V_{in} by the following equations

$$\frac{A_l}{V_{in}} = -\frac{E_a d_{31}^a r_a\left(\nu_p^2-1\right)(\nu_a+1)\,e^{ik_l r_a}}{E_p h_p(\nu_a^2-1)(ik_l r_a - \nu_p) - E_a h_a\left(\nu_p^2-1\right)(ik_l r_a - \nu_a)} \tag{95}$$

$$\frac{A_f}{V_{in}} = -\frac{2E_a d_{31}^a h_p r_a(\nu_a+1)\,e^{ik_f r_a}}{k_f\left(4D_p(\nu_a^2-1)(k_f r_a + i\nu_p) + E_a h_p h_a^2(k_f r_a + i\nu_a)\right)}. \tag{96}$$

4.1.1 Sensor

Figure 44(a) presents the top view of a thin plate with two circular piezoelectric transducers placed on its surface. The first one is the actuator C placed at the point a to create radial waves. The sensor S placed at the point b captures part of them according to its dimension (RAGHAVAN; CESNIK, 2005; YEUM; SOHN; IHN, 2011). Figure 44(b) shows geometric parameters involving both actuator and sensor and their relative positions. c is the distance between the centers of the transducers and r_s is the sensor radius. According to Lin and Yuan (2001), the sensor output voltage $V_{out}(\omega)$ is given by

$$V_{out} = \frac{d_{31}^s E_s h_s}{4K_3\varepsilon_0(\pi r_s)^2(1-\nu_s)}\iint_{S_s}\left(\frac{du_r^s}{dr} + \frac{u_r^s}{r}\right) r\,dr\,d\theta \tag{97}$$

where K_3 is the relative dielectric constant, $\varepsilon_0 = 8.85\cdot 10^{-12}$ F.m^{-1}, S_s is the surface area of the sensor, E_s and ν_s are respectively the Young's modulus and Poison's coefficient of the sensor, u_r^s is the displacement of the sensor and d_{31}^s its induced strain coefficient. Considering that c is greater than r_s such that $\cos(\theta_r) \cong 1-\theta_r^2/2$, Equation (97) is rewritten by considering $\theta_r \cong \sqrt{\frac{r_s^2-(c-r)^2}{cr}}$, as noted by Yeum, Sohn and Ihn (2011). Then,

Figure 44 – (a) Thin plate with one circular piezoelectric transducer generating a radial wave and another one capturing the waves. (b) Distances and parameters relation both actuator and sensor.

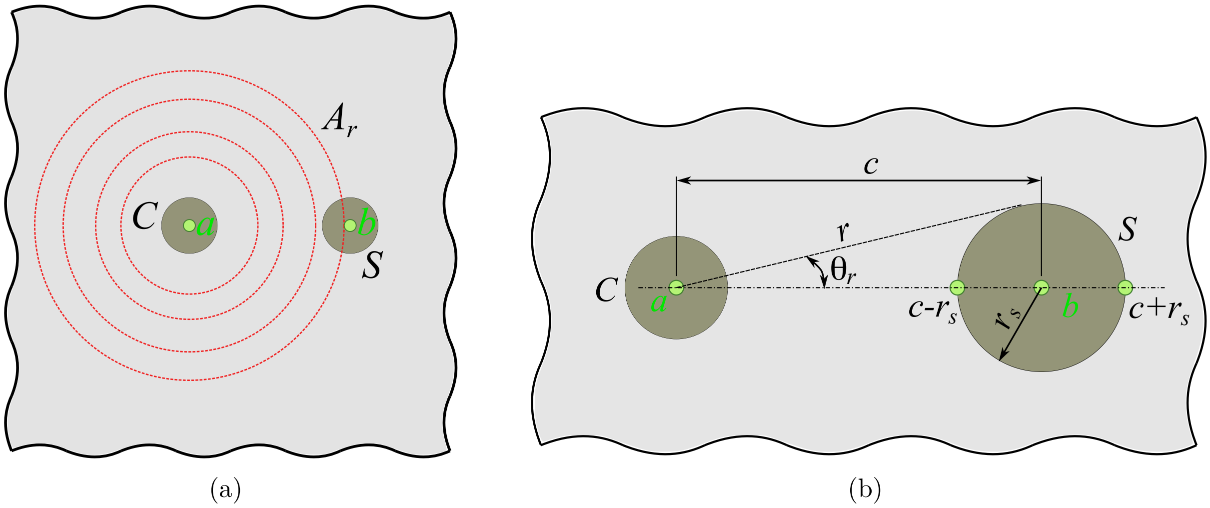

Source: elaborated by the author.

$$V_{out} = \frac{d_{31}^s E_s h_s}{2K_3\varepsilon_0(\pi r_s)^2(1-\nu_s)} \int_{c-r_s}^{c+r_s} \left(r\frac{du_r^s}{dr} + u_r^s \right) \sqrt{\frac{r_s^2-(c-r)^2}{cr}}dr. \tag{98}$$

For the longitudinal radial wave propagation $u_r^s = u_r$, the following equation is obtained

$$V_{out}^l = \frac{d_{31}^s E_s h_s A_l}{2K_3\varepsilon_0(\pi r_s)^2(1-\nu_s)} \int_{c-r_s}^{c+r_s} (1-ik_l r)e^{-ik_l r} \sqrt{\frac{r_s^2-(c-r)^2}{cr}}dr. \tag{99}$$

Substituing Equation (95) into Equation (99), the relation between V_{out}^l and V_{in} is given by

$$\frac{V_{out}^l}{V_{in}} = -\frac{E_a E_s d_{31}^a d_{31}^s h_s r_a \left(\nu_p^2-1\right)(\nu_a+1)e^{ik_l r_a}}{2\pi^2 K_3 \epsilon_0 r_s^2 (1-\nu_s)\left(E_p h_p (\nu_a^2-1)(ik_l r_a-\nu_p) - E_a h_a\left(\nu_p^2-1\right)(ik_l r_a-\nu_a)\right)} I_l \tag{100}$$

where $I_l = \int_{c-r_s}^{c+r_s} (1-ik_l r)e^{-ik_l r} \sqrt{\frac{r_s^2-(c-r)^2}{cr}}dr$.

For the flexural radial wave propagation, the displacement is given by $u_r^s = -z\frac{dw_r}{dr}$ (UGURAL, 2017). Substituing this displacement into Equation (98) for $z = \frac{h_p}{2}$, the output voltage is given by

$$V_{\text{out}}^f = \frac{d_{31}^s E_s h_s h_p k_f A_f}{4K_3\varepsilon_0(\pi r_s)^2(1-\nu_s)} \int_{c-r_s}^{c+r_s} (k_f r + i)e^{-ik_f r} \sqrt{\frac{r_s^2-(c-r)^2}{cr}}dr. \tag{101}$$

Substituing Equation (96) into Equation (101), the relation between input and output voltages for flexural wave is given by

$$\frac{V_{out}^{f}}{V_{in}} = -\frac{E_a E_s d_{31}^{s} d_{31}^{a} h_p^2 h_s r_a \left(\nu_a + 1\right) e^{ik_f r_a}}{2\pi^2 K_3 \epsilon_0 r_s^2 \left(1 - \nu_s\right) \left(4 D_p \left(\nu_a^2 - 1\right) \left(k_f r_a + i\nu_p\right) + E_a h_p h_a^2 \left(k_f r_a + i\nu_a\right)\right)} I_f \tag{102}$$

where $I_f = \int_{c-r_s}^{c+r_s} (k_f r + i) e^{-ik_f r} \sqrt{\frac{r_s^2 - (c-r)^2}{cr}} dr$. The total output voltage at the sensor is given by $V_{out} = V_{out}^{f} + V_{out}^{l}$, which allows one to write the following equation

$$\frac{V_{out}}{V_{in}} = -\frac{L_a L_s Q}{2\pi^2} \left(\frac{e^{ik_l r_a}}{X_l} I_l + \frac{e^{ik_f r_a}}{X_f} I_f \right) \tag{103}$$

where $X_l = \frac{E_p h_p (\nu_a^2 - 1)(ik_l r_a - \nu_p) - E_a h_a (\nu_p^2 - 1)(ik_l r_a - \nu_a)}{\nu_p^2 - 1}$ and $X_f = \frac{4 D_p (\nu_a^2 - 1)(k_f r_a + i\nu_p) + E_a h_p h_a^2 (k_f r_a + i\nu_a)}{h_p^2}$. In addition, $L_a = E_a d_{31}^{a} (\nu_a + 1)$, $L_s = E_s d_{31}^{s} / (K_3 \epsilon_0 (1 - \nu_s))$ and $Q = h_s r_a / r_s^2$. For the input voltage applied at the center of the actuator, $e^{ik_l r_a} = e^{ik_f r_a} = 1$. Figure 45 shows the phase velocities for longitudinal and flexural waves and also the phase velocities obtained for the S_0 and A_0 Lamb wave modes (RAGHAVAN; CESNIK, 2005; GIURGIUTIU, 2003). Note that both flexural wave and the A_0 Lamb wave mode have similar phase velocities for low-frequency range. The observed difference $f h_p > 0.1$ implies small delay in the time domain, which can be corrected by considering the term $I_c = e^{-ic(\tilde{k}_f - k_f)}$ (where $\tilde{k}_f$ is the wavenumber of the A_0 Lamb wave mode) to compute part of the Equation (103) relative to the flexural wave propagation. In practice, this term translate the flexural wave back to the origin of the coordinate system and then translate it forward in the time domain with the phase velocity of the A_0 Lamb wave mode without changing the wave amplitude. This is a convenient procedure to obtain a more accurate theoretical prediction in the time domain in comparison with the experimental results. Figure 46 presents the flexural waves obtained before and after applying the introduced term I_c, highlighting its effect on the time domain.

Figure 45 – Phase velocities obtained for longitudinal (continuous line, green) and flexural (dashed line, blue) and also for the S_0 (dotted line, pink) and A_0 (dash-dotted line) Lamb Wave modes.

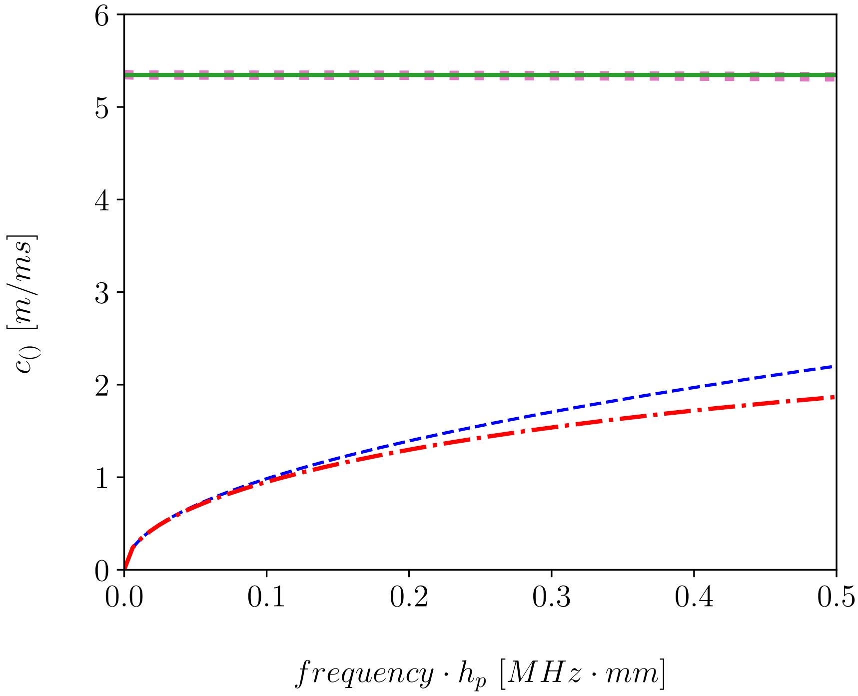

Source: elaborated by the author.

Figure 46 – Flexural waves in time obtain obtained before (dash-dotted line, green) and after (continuous line, red) applying the factor I_c.

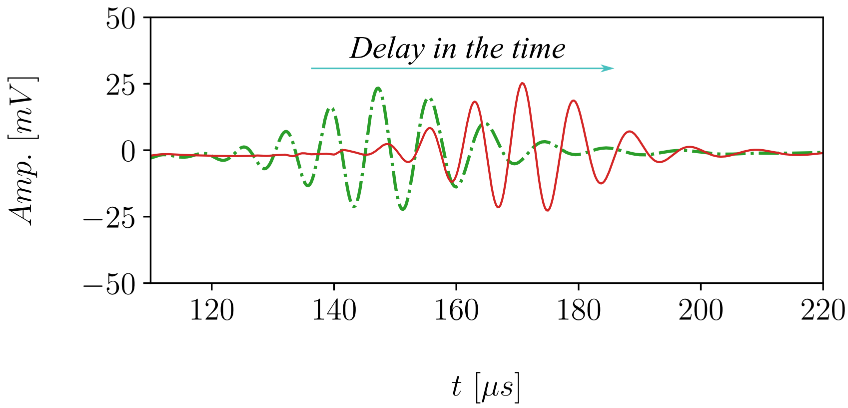

Source: elaborated by the author.

4.2 RESULTS AND DISCUSSION

This section presents numerical and experimental results to demonstrate the proposed approach. An aluminum plate with h_p = 1.5 mm and physical properties ρ_p = 2710 kg/m^3, E_p = 69 MPa, ν_p = 0.33 is considered. Two circular piezoelectric transducers are considered on the plate to work as actuator and sensor, as presented in Figure 42. Their physical and geometrical properties are $E_a = E_s = 50$ MPa, $d_{31}^s = d_{31}^a = -400 \cdot 10^{-12}$ m/V, $\nu_s = \nu_a = 0.36$ and $\rho_a = 7800$ kg/m^3.

Figures 47(a) and 47(b) show respectively the magnitudes of the electrical voltage obtained for the longitudinal and flexural waves considering different sensor radii. This relation assumes the minimum values if $r_s/\lambda_{()} = \frac{(0.22+m)}{2}$, where $m = 1, 2, 3, ...$ Then, the corresponding frequencies are not recommended to be considered when establishing a SHM process due to the low wave amplitudes incoming at the sensor. On the other hand, $r_s/\lambda_{()} = 0.15$ (the first peaks) and $r_s/\lambda_{()} = \frac{(n-0.3)}{2}$ (the other peaks), where $n = 2, 3, ...$, indicate the frequencies more convenient to monitore the structure because they are associated to the maximum local wave magnitudes, corresponding to the optimal frequencies to create longitudinal and flexural waves when using circular piezoelectric transducers. These frequencies are respectively given by $f_o^{l(1)} = \frac{0.15}{r_s}\sqrt{\frac{E_p}{\rho_p(1-\nu_p^2)}}$ [Hz] and $f_o^{l(n)} = \frac{(n-0.3)}{2r_s}\sqrt{\frac{E_p}{\rho_p(1-\nu_p^2)}}$ [Hz] for the longitudinal waves and by $f_o^{f(1)} = 2\pi h_p\left(\frac{0.15}{r_s}\right)^2\sqrt{\frac{E_p}{12\rho_p(1-\nu_p^2)}}$ [Hz] and $f_o^{f(n)} = 2\pi h_p\left(\frac{(n-0.3)}{2r_s}\right)^2\sqrt{\frac{E_p}{12\rho(1-\nu_p^2)}}$ [Hz] for the flexural waves.

Figure 47 – Magnitudes of the output and input voltage ratios ($|V_{out}/V_{in}|$) for (a) longitudinal and (b) flexural waves in terms of the sensor radius r_s and the wavelength $\lambda_{()}$ ratio (where l indicates the longitudinal wave and f the flexural one) for different values of actuator radius r_a. $r_a/r_s = 0.5$ (continuous line, red), $r_a/r_s = 1$ (dash-dotted line, blue) and $r_a/r_s = 2$ (dashed line, green). Symbols $\diamond$, $\square$ and $\bigcirc$ indicate the maximum local magnitudes obtained at the peaks for $r_a/r_s = 0.5$, $r_a/r_s = 1$ and $r_a/r_s = 2$, respectively.

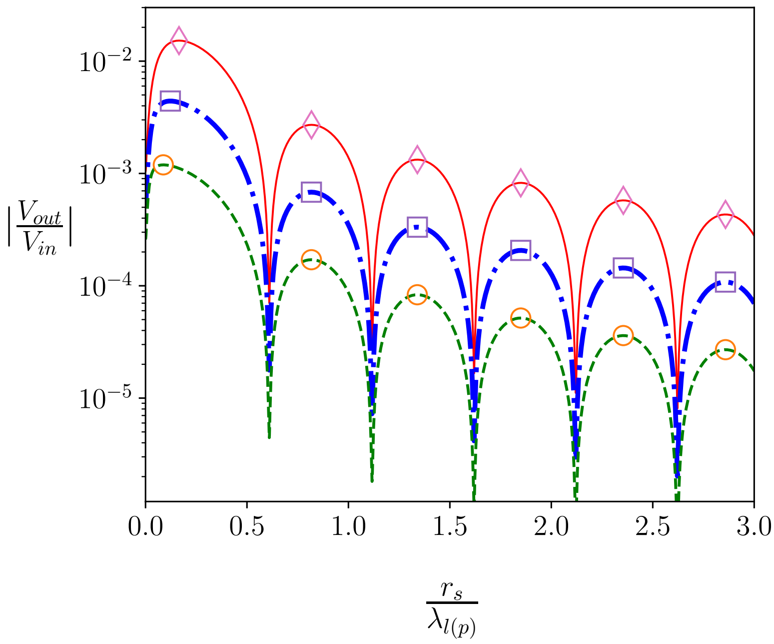

(a) Longitudinal wave

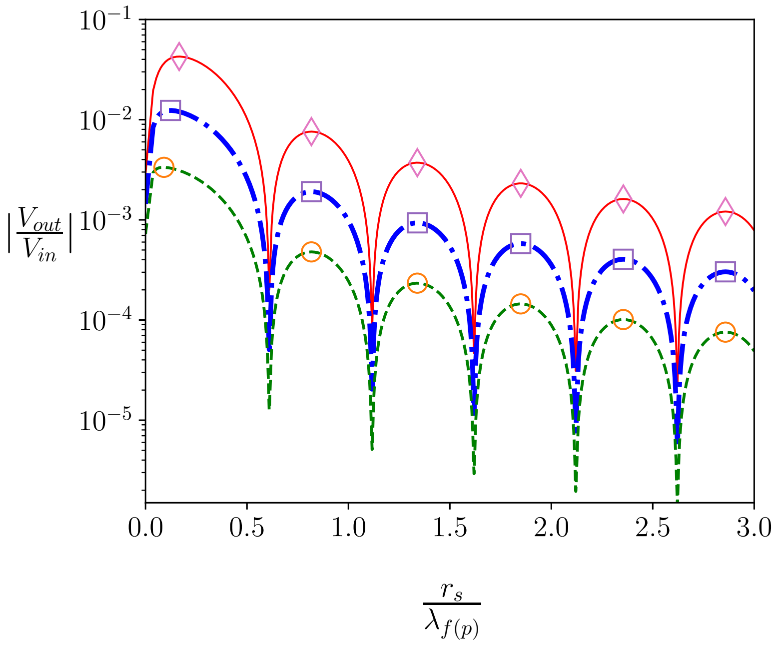

(b) Flexural wave

Source: elaborated by the author.

Maximum magnitudes can be found when considering the frequencies for different peaks, and they are presented in Figures 48(a) and 48(b) for the first four peaks and different ratios between the circular piezoelectric transducers radii. Note that the first peak has the highest magnitudes in respect to the ratio r_a/r_s, indicating that the first optimal frequency is the best option to create and measure waves for damage detection. In addition, to maximize the amplitudes at the sensor, the strategy is to decrease the actuator radius or increase the sensor radius, i.e., decrease the ratio r_a/r_s.

Figure 48 – Maximum magnitudes of the output and input voltage ratios ($|V_{out}/V_{in}|_{max}$) obtained at the first four peaks for (a) longitudinal and (b) flexural waves in terms of the ratios of the sensor r_s and actuator r_a radii. Continuous line (green) indicates the results for the first peak, dashed (red) line for the second peak, dash-dotted (blue) line for the third peak and dotted (black) line for the fourth one.

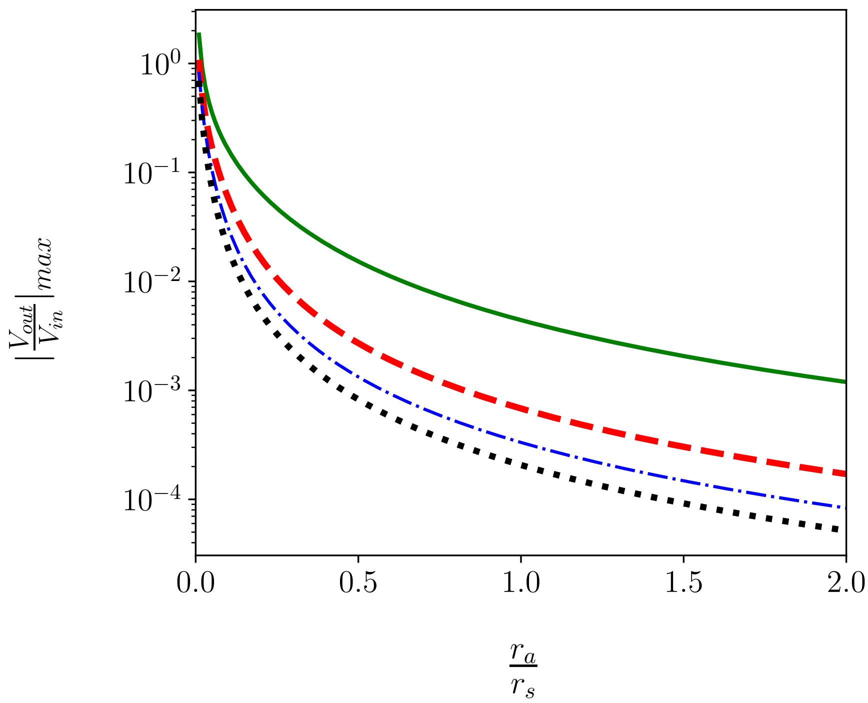

(a) Longitudinal wave

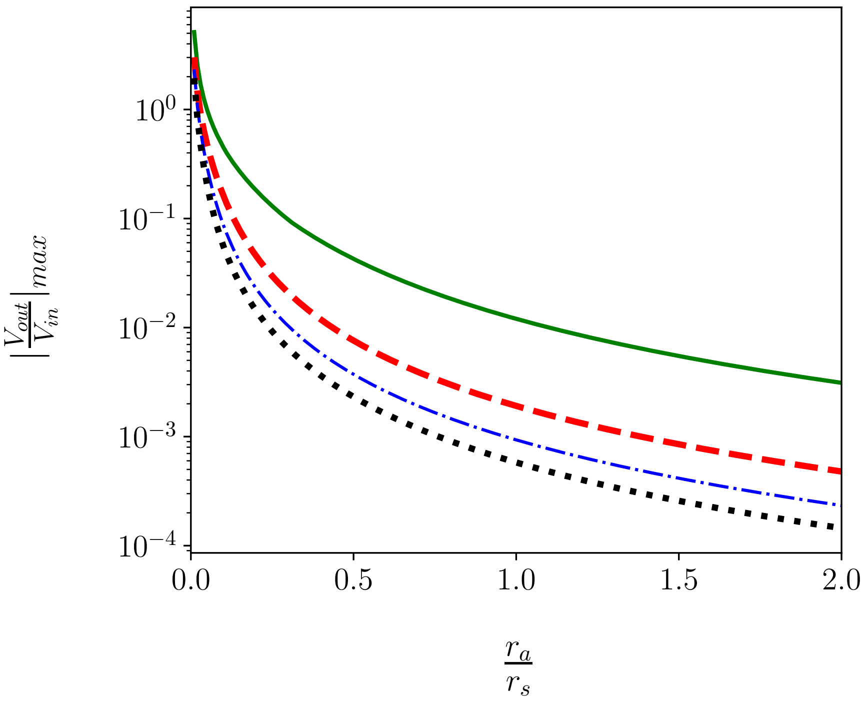

(b) Flexural wave

Source: elaborated by the author.

Figures 49(a) and 49(b) present the magnitudes of the amplitudes obtained for different ratios between the sensor and actuator thicknesses for constant piezoelectric transducers radii. At the optimal frequencies, maximum magnitudes are found at the peaks, which are presented in Figures 50(a) and 50(b) for the first four peaks in terms of the ratio h_s/h_a. Note that the highest maximum local amplitude is achieved for the first peak, which is the best option to create and capture longitudinal and flexural waves. In this case, a decrease in the actuator thickness or increase in the sensor thickness maximizes the magnitude $|V_{out}/V_{in}|$, which is a good strategy for establishing practical SHM applications.

Figure 49 – Magnitudes of the output and input voltage ratios ($|V_{out}/V_{in}|$) for (a) longitudinal and (b) flexural waves in terms of the sensor radius r_s and the wavelength $\lambda_{()}$ ratio (where l indicates the lonfitudinal wave and f the flexural one) for different values of actuator thickness h_s. $h_s/h_a = 0.5$ (continuous line, red), $h_s/h_a = 1$ (dash-dotted line, blue) and $h_s/h_a = 2$ (dashed line, green). Symbols $\diamond$, $\square$ and $\bigcirc$ indicate the maximum magnitudes obtained at the peaks for $h_s/h_a = 0.5$, $h_s/h_a = 1$ and $h_s/h_a = 2$, respectively.

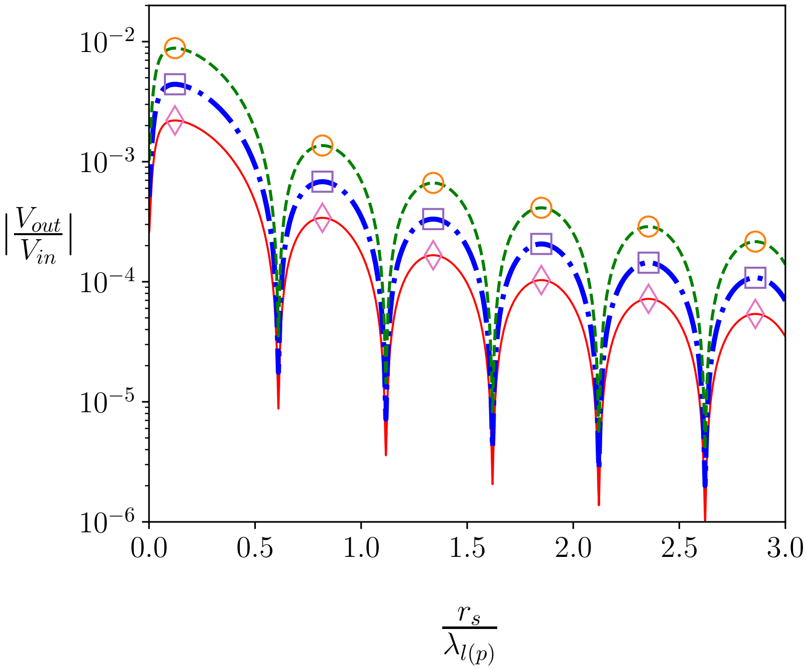

(a) Longitudinal wave

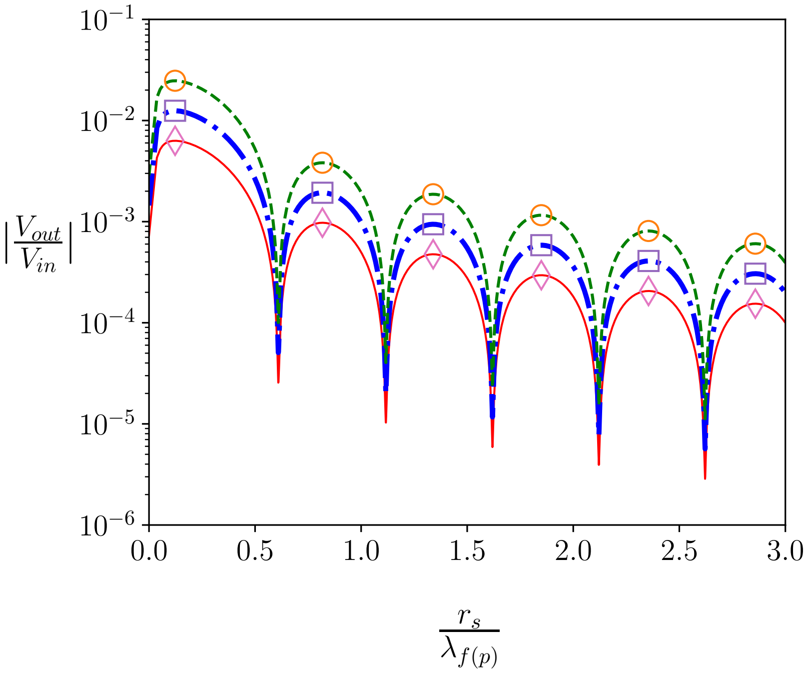

(b) Flexural wave

Source: elaborated by the author.

Figure 50 – Maximum magnitudes of the output and input voltage ratios ($|V_{out}/V_{in}|_{max}$) obtained at the 4 first peaks for (a) longitudinal and (b) flexural waves in terms of the sensor h_s and actuator h_a thicknesses ratio. Continuous line (green) indicates the results for the first peak, dashed (red) line for the second peak, dash-dotted (blue) line for the third peak and dotted (black) line for the fourth one.

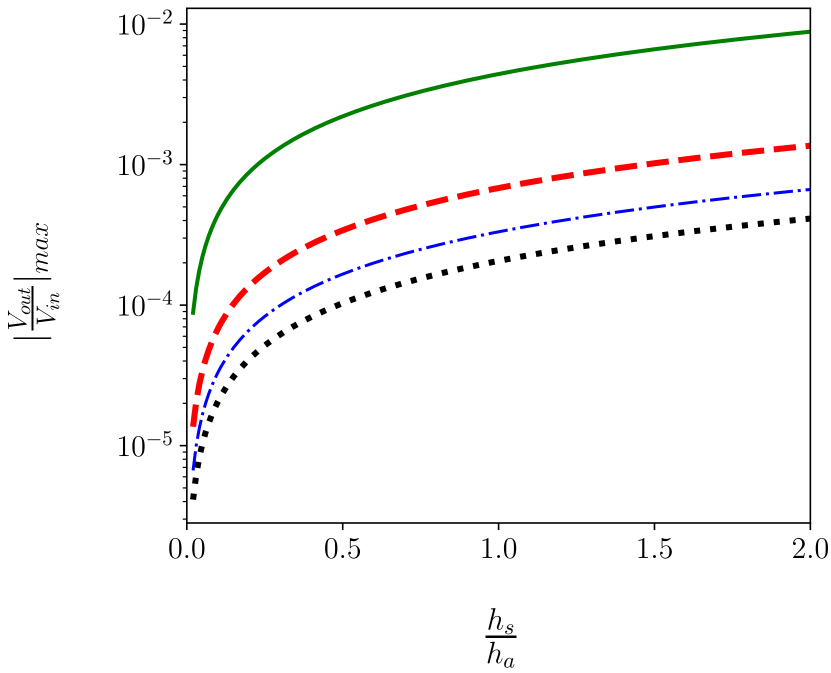

(a) Longitudinal wave

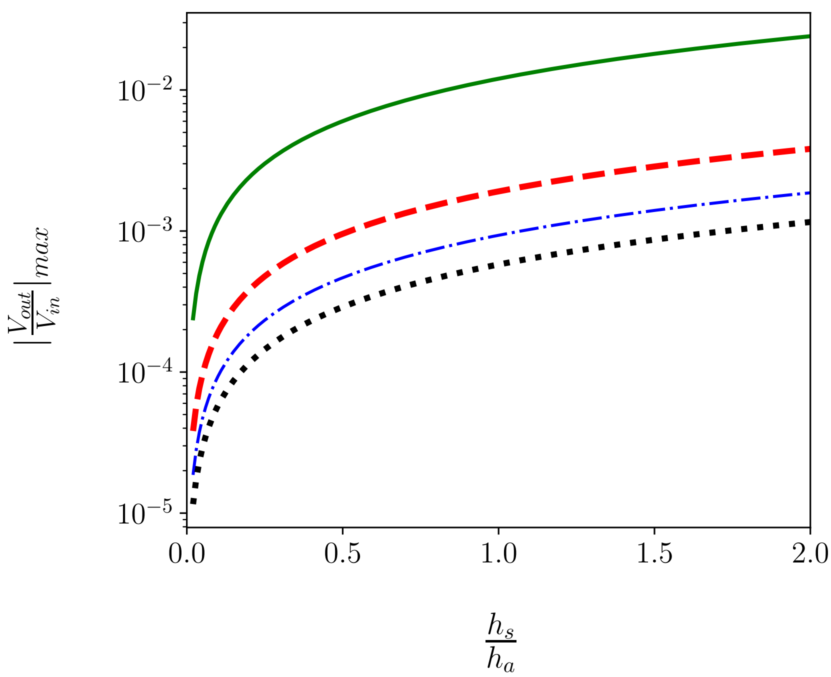

(b) Flexural wave

Source: elaborated by the author.

Figures 51(a) and 51(b) show the magnitudes $|V_{out}/V_{in}|$ respectively for longitudinal and flexural waves when considering different values of c, which corresponds to the distance between the piezoelectric transducers. The changes in c do not affect the maximum amplitudes, and a decrease in c/r_a increases the magnitudes $|V_{out}/V_{in}|$ at the frequencies corresponding to the valleys of the curves. On the other hand, for flexural waves, if $c_s/r_a > 40$, the magnitude $|V_{out}/V_{in}|_{min}$ does not change significantly and it is approximately a constant value for all peaks. These results demonstrate that the relation between the input and output voltage from circular PZT transducers is not sensitive to the ratio c/r_a.

Figure 51 – Magnitudes of the output and input voltage ratios ($|V_{out}/V_{in}|$) for (a) longitudinal and (b) flexural waves in terms of the sensor radius r_a and the wavelength $\lambda_{()}$ ratio (where l indicates the longitudinal wave and f the flexural one) for different distances c. c/r_a = 5 (continuous line, red), c/r_a = 50 (dot-dashed line, green) and c/r_a = 100 (dashed line, blue).

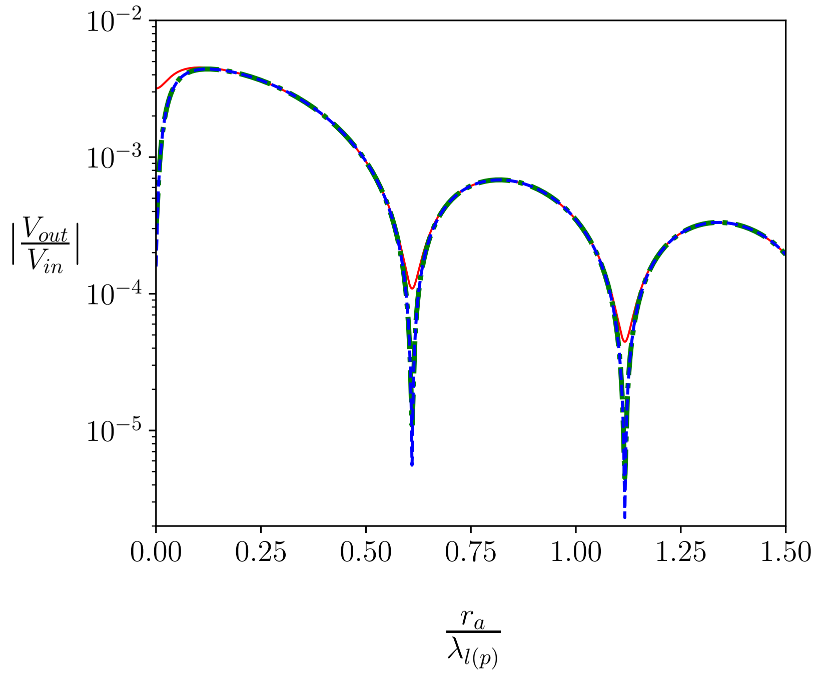

(a) Longitudinal wave

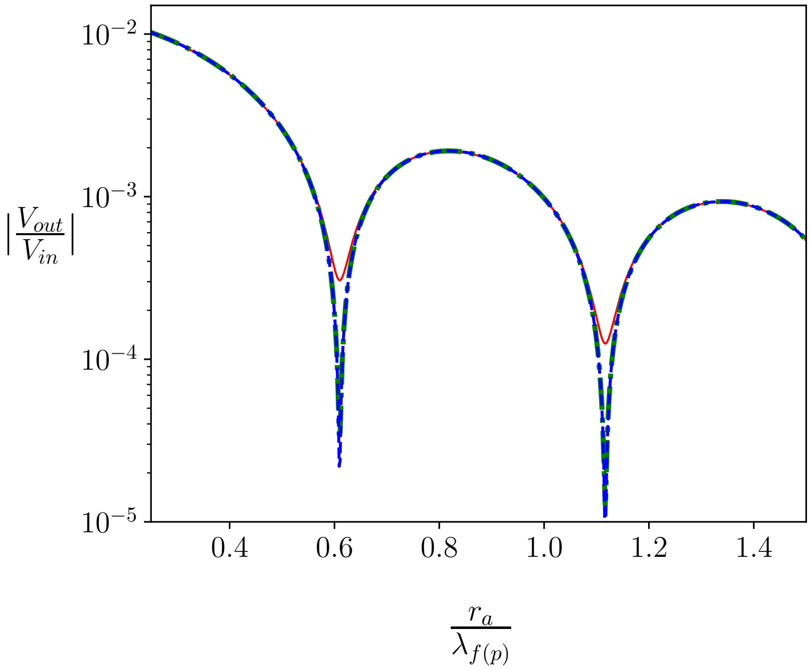

(b) Flexural wave

Source: elaborated by the author.

4.3 EXPERIMENTAL TESTS

Experimental tests were carried out on an aluminum plate with dimensions 1000 mm x 1000 mm x 1.5 mm. Figure 52 presents a schematic view and photographs from the experimental setup used in the tests. Two circular piezoelectric transducers (type disc bender) are bonded to the surface of the plate. Circular piezoelectric transducer C is employed as actuator and S as sensor. The properties for the plate and piezoelectric transducers are presented in Table 1. The input signal is generated by the NI USB 6353 from National Instruments coupled to a power amplifier EL 1225 from Mide QuicPack. An oscilloscope DSO7034B Keysight is employed to measure the signals from the actuator and sensor. A LabVIEW-based application is used to generate input signals with a tone burst with 5 cycles for pre-defined frequencies.

Table 1 – Geometrical and physical properties of the plate and circular piezoelectric transducers.

	$E_{()}$ [Mpa]	$\rho_{()}$ [kg/m^3]	$\nu_{()}$	$r_{()}$ [mm]	$h_{()}$ [mm]	$d_{31}^{()}$ [m/V]	K_3
Plate	69	2710	0.33	-	1.5	-	-
Actuator (C)	50	7800	0.36	9.7	0.23	-400 $\cdot 10^{-12}$	3800
Sensor (S)	50	7800	0.36	9.7	0.23	-400 $\cdot 10^{-12}$	3800

Figure 52 – (a) Schematic view and (b) photographs from the experimental setup (dimensions in cm).

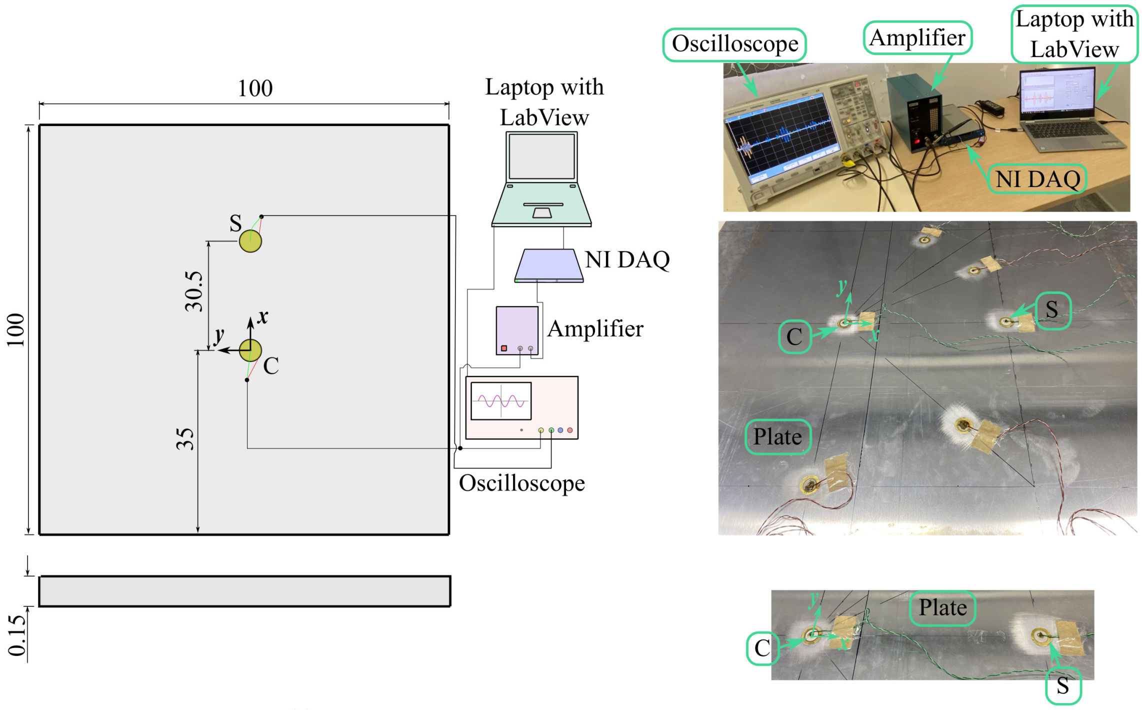

(a) (b)

Source: elaborated by the author.

Input signals are generated by burst tones centered at the frequencies 130 kHz, 160 kHz, 180 kHz and 190 kHz. The Fourier Transform is used to obtain the waves in the frequency domain. The relations between output and input voltages are computed for each frequency. Figure 53 shows these ratios for longitudinal and flexural waves in terms of the relation $r_s/\lambda_{()}$ for the experimental signals in comparison with the corresponding theoretical values computed by Equation (103). The optimal frequency for the first peak of longitudinal wave is equal to $f_o^{l(1)}$ = 82.7 kHz, and the optimal frequency for the second peak of flexural wave is equal to $f_o^{f(2)}$ = 111.7 kHz. For both types of waves, these frequencies are in the range defined by a peak and the first valley in the right-hand side of the curve, which explains the decrease in the wave amplitudes with an increase in frequency. Note that the experimental tests were carried out at no optimal frequencies due to the plate dimensions. At an optimal frequency, the boundary reflected waves are verified at the same time interval at which the flexural and longitudinal waves are observed, and their effects on the measured wave introduce an additional challenge to compare the theoretical and experimental results. Figure 53 shows that frequency 190 kHz is better to create longitudinal waves than flexural waves. Considering $R = |V^l_{out}/V^f_{out}|$, the values of this index R computed with the experimental data for 130, 160, 180 and 190

kHz are equal to 3.16, 4.72, 5.71 and 6.62, respectively, which allows one to observe that even with smaller amplitude compared to the longitudinal wave obtained at 130 kHz, the longitudinal wave at 190 kHz has higher amplitude in comparison to the flexural wave at this frequency, as shown in Figure 54(d). The experimental relation between output and input voltages is different from zero because the experimental input signal used contains energy in a frequency band, as presented by Lopes, Gonsalez-Bueno and Bueno (2022). Figure 54 shows the experimental and theoretical longitudinal and flexural waves in the time domain for the analyzed frequecies and the corresponding indices R computed for each frequency. Note that there is a good agreement between the results. The results in the time domain reveal an accurate theoretical prediction for 160 kHz when considering the longitudinal wave. They show that the flexural wave has an almost zero amplitude at the frequency of 190 kHz.

Figure 53 – Magnitudes of the output and input voltage ratios ($|V_{out}/V_{in}|$) for longitudinal (dashed line) and flexural (continuous line) waves [obtained with Equation (103)] in terms of the sensor radius r_a and the wavelength $\lambda_{()}$ ratio for each wave (where l indicates the longitudinal wave and f the flexural one). Symbols □ and ◇ indicate the experimental results obtained for longitudinal and flexural waves when frequencies are equal to 130 kHz ($r_a/\lambda_{l(p)}$ = 0.24 and $r_a/\lambda_{f(p)}$ = 0.92), 160 kHz ($r_a/\lambda_{l(p)}$ = 0.29 and $r_a/\lambda_{f(p)}$ = 1.02), 180 kHz ($r_a/\lambda_{l(p)}$ = 0.33 and $r_a/\lambda_{f(p)}$ = 1.08) and 190 kHz ($r_a/\lambda_{l(p)}$ = 0.35 and $r_a/\lambda_{f(p)}$ = 1.11).

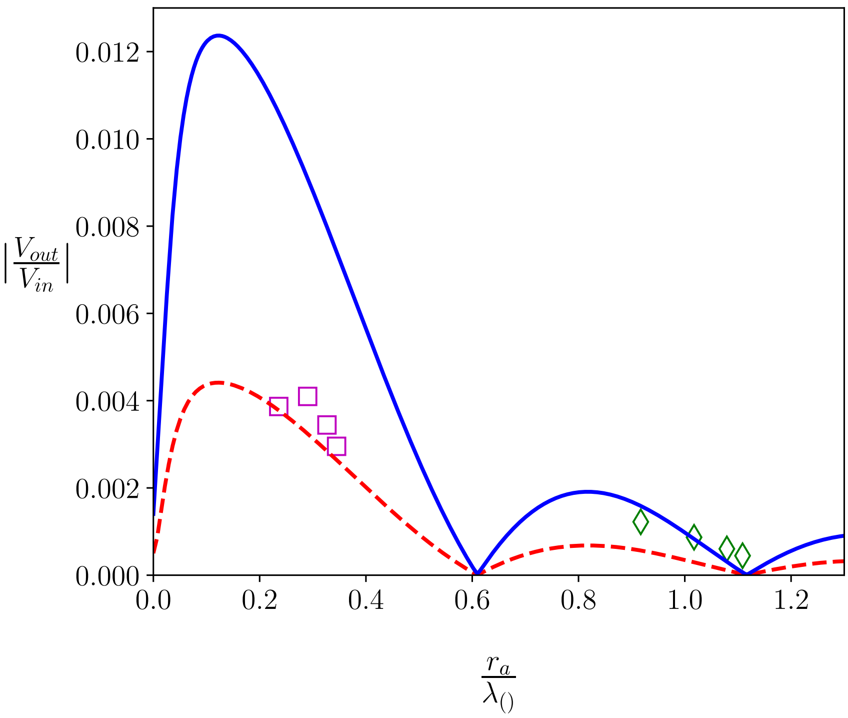

Source: elaborated by the author.

Figure 54 – Wave amplitudes obtained experimentally (continous line, blue) and analytically (dashed line, red) with Equation (103) for 130 kHz, 160 kHz, 180 kHz and 190 kHz. Rectangles (dotted line, green) and ellipses (dash-dotted line, yellow) highlight the longitudinal and flexural waves, respectively. R represents the ratios between experimental magnitudes of longuitudinal and flexural waves obtained from Figure 53.

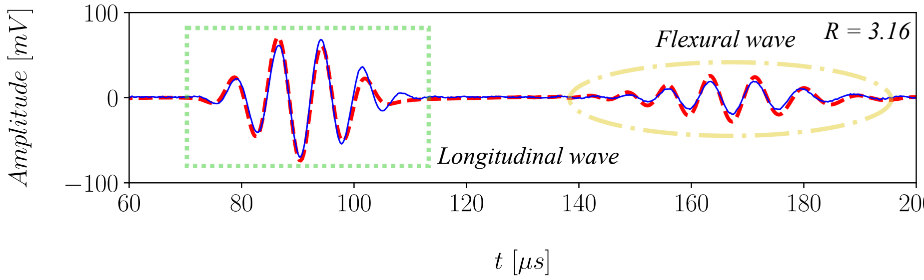

(a) 130 kHz

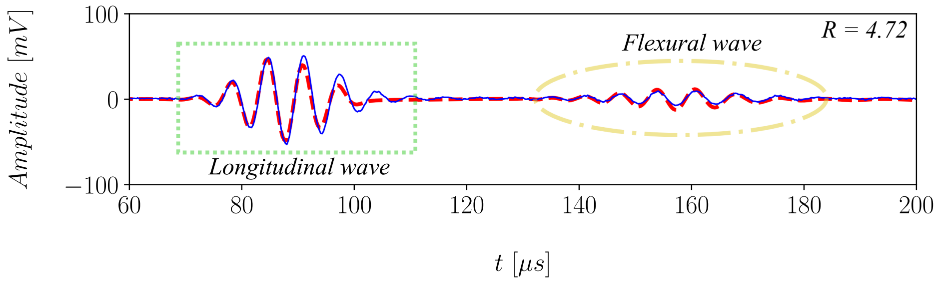

(b) 160 kHz

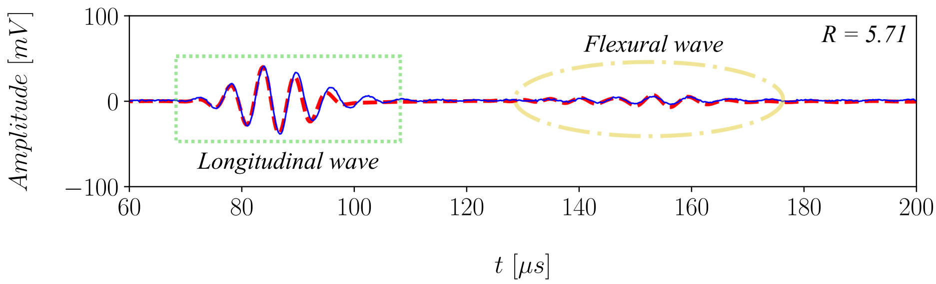

(c) 180 kHz

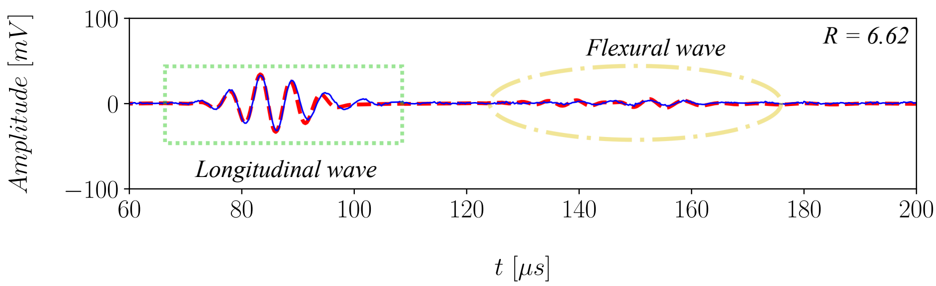

(d) 190 kHz

Source: elaborated by the author.

4.4 FINAL REMARKS

The present chapter introduced an approach to determine longitudinal and flexural wave amplitudes when using circular piezoelectric transducers bonded to thin plates. The proposal demonstrates that there are optimal frequencies to create and measure longitudinal and flexural waves, whereas there are other frequencies for which the sensor obtains zero amplitude. Thus, the frequency of excitation affects the SHM systems in terms of damage detection. The results show that the SHM analyst needs to define the optimal frequencies according to the physical properties of the circular piezoelectric transducers.

At the optimal frequencies the highest magnitudes of the ratio between output and input voltages are observed. The first peak corresponds to the highest amplitudes, and an increase in the ratio between actuator and sensor radii causes a decrease in the magnitudes of the waves amplitudes incoming at the sensor. It is shown that a change in the thicknesses of the circular piezoelectric transducers does not change the optimal frequencies, but it can be used to maximize the response obtained by the sensor by increasing the sensor thickness or decreasing the actuator thickness. The distance (c) between the centers of actuator and sensor affects the magnitudes at the valleys, and a small ratio between c and r_a increases the magnitude obtained at these points.

The introduced approach provides new equations to compute output voltages, and optimal frequencies can be easily determined in comparison with other methodologies from the literature. In a practical case, based on these new equations, the SHM analyst can compute the optimal frequencies and predict the output voltages by using a simple computational code, which makes easier and more accurate the design of a damage detection campaign.

Experimental tests were presented to demonstrate the proposed approach. An aluminum plate with two circular piezoelectric transducers type disc bender bonded to its surface was considered. The results show that an increase in frequency decreases the output and input voltage ratios if the input signal creates waves in the frequency range defined by a peak and the first valley in the right-hand side of the curve in the frequency domain. Theoretical and experimental results show a good agreement to each other, and they confirm the proposed strategy to obtain higher level of responses from piezoelectric circular sensors used to monitor thin plates.

5 FINAL REMARKS

This thesis presents an investigation into the scattering of longitudinal and flexural waves in damaged plate-like structures with symmetrical damage considering circular piezoelectric transducers and oblique incidence. The findings presented herein contribute for an improvement of the SHM systems based on wave propagation.

A model considering each wave packet for the transmitted and reflected waves is presented for longitudinal and flexural waves considering oblique incidence. In the case of longitudinal wave scattering, the results show that the wave packet amplitudes are constant over frequency, and the first transmitted wave packet has an amplitude larger than the following transmitted wave packets, especially for low-damage severity. It is shown that the optimal frequencies for damage detection based on the longitudinal waves only depend on the damage severity and the incidence angle does not affect them. On the other hand, for the case of the flexural waves, the optimal frequencies depend on both, that is, damage severity and incidence angle.

If a circular sensor is coupled to the plate, it is demonstrated that the number of wave packets collected by it depends on its radius, length of the damage l_x and its position on the plate. For example, if the longitudinal wave is created and the sensor radius is $r_L < 2l_x \tan(\theta)$, only the first reflected wave packet arrives at the sensor. In a practical application, the SHM analyst can define the damage length to be detected and compute the sensor size according to the number of wave packets to be collected and analyzed. In addition, for the longitudinal wave scattering, if only the first reflected wave packets is captured by the sensor, the SHM analyst can predict the damage depth and the optimal frequencies do not have be considered due to the no interference between wave packets. If the two first wave packets are captured by the sensor, it is shown that the results are similar to the case where the third wave packet is also captured, which indicates that the resulting waves are composed mainly by the two first wave packets, and the interference between them defines the resulting wave amplitude.

If a circular actuator is used to create radial waves, the sensors collect wave packets coming from different directions and with different angles of propagation, which depend on the relative position between actuator, damage and sensor. On the other hand, for flexural wave, if $r_{()} < 2l_x \tan(\phi_1)$, the sensor captures the first three wave packets propagating with angles α_1, α_2 and α_3, respectively, where $\alpha_1 > \alpha_2 > \alpha_3$. Experimental tests were presented to demonstrate the approach.

The thesis also introduces the modeling of circular piezoelectric transducers coupled to a plate-like structure, used to create and measure longitudinal and flexural waves. Optimal frequencies to create and measure the waves are obtained analytically in terms of the piezoelectric transducer and plate properties, and they can be easily determined in comparison with other methodologies from the literature. It is shown that the SHM analyst must be careful when defining the excitation frequency for SHM campaigns when using circular piezoelectric transducers. In a practical case, based on these new equations, the SHM analyst can compute the optimal frequencies and predict the output voltages by using a simple computational code, which makes easier and more accurate the design of a damage detection campaign. Experimental tests were presented to demonstrate the proposed approach. Based on the results presented herein, the SHM analyst can define the damage width l_x to be detected, compute the optimal frequencies to detect the particular damage and then determine a pair of actuator and sensor to obtain the optimal frequency to create and capture the waves close to the optimal frequency for damage detection, which contributes to detecting the damage.

5.1 SUGGESTIONS FOR FUTURE WORK

Future works can consider the methodology presented herein and derive new studies. Then, the following suggestions are presented:

- To reduce the length of the damage in the y direction;
- To consider an asymmetric damage with small length in the y direction;
- To investigate the modeling of different shapes of actuators and sensors, such as the square and diamond types, and others;
- To investigate how shear waves interact with the symmetric damage;
- To consider small crack, that is, $l_x \to 0$.

REFERENCES

AHMIDA, K.; ARRUDA, J. On the relation between complex modes and wave propagation phenomena. **Journal of Sound and Vibration**, v. 255, n. 4, p. 663 -- 684, 2002. ISSN 0022-460X.

AI, D.; LUO, H.; WANG, C.; ZHU, H. Monitoring of the load-induced rc beam structural tension/compression stress and damage using piezoelectric transducers. **Engineering Structures**, v. 154, p. 38 -- 51, 2018. ISSN 0141-0296.

AJITH, V.; GOPALAKRISHNAN, S. Wave propagation in stiffened structures using spectrally formulated finite element. **European Journal of Mechanics - A/Solids**, v. 41, p. 1 -- 15, 2013. ISSN 0997-7538.

BAPTISTA, F. G.; BUDOYA, D. E.; ALMEIDA, V. A. D. d.; ULSON, J. A. C. An experimental study on the effect of temperature on piezoelectric sensors for impedance-based structural health monitoring. **Sensors**, v. 14, n. 1, p. 1208--1227, 2014. ISSN 1424-8220.

BENMEDDOUR, F.; GRONDEL, S.; ASSAAD, J.; MOULIN, E. Study of the fundamental lamb modes interaction with asymmetrical discontinuities. **NDT & E International**, v. 41, n. 5, p. 330 -- 340, 2008. ISSN 0963-8695.

BHUIYAN, M. Y.; HAIDER, M. F.; PODDAR, B.; GIURGIUTIU, V. Guided wave crack detection and size estimation in stiffened structures. In: SHULL, P. J. (Ed.). **Nondestructive Characterization and Monitoring of Advanced Materials, Aerospace, Civil Infrastructure, and Transportation XII**. [S.l.]: SPIE, 2018. v. 10599, p. 423 -- 433.

BRENNAN, M. J. **Active Control of Waves on one-dimensional Structures**. Thesis (Ph. D.) --- University of Southampton, November 1994.

BROGIN, J. A. F.; FABER, J.; BUENO, D. D. Enhanced use practices in ssvep-based bcis using an analytical approach of canonical correlation analysis. **Biomedical Signal Processing and Control**, v. 55, p. 101644, 2020. ISSN 1746-8094.

CHO, Y. Estimation of ultrasonic guided wave mode conversion in a plate with thickness variation. **IEEE Transactions on Ultrasonics, Ferroelectrics, and Frequency Control**, v. 47, n. 3, p. 591--603, May 2000. ISSN 1525-8955.

CHO, Y.; ROSE, J. L. An elastodynamic hybrid boundary element study for elastic guided wave interactions with a surface breaking defect. **International Journal of Solids and Structures**, v. 37, n. 30, p. 4103 -- 4124, 2000. ISSN 0020-7683.

CUENCA, J. **Wave Models for the flexural waves vibrations of thin plates - Model of the vibrations of polygonal plates by the image source method**

- **Vibration damping using the acoustic black hole effect.** Dissertação (Ph.D Thesis - UniversitÈ du Maine), 2009.

DASGUPTA, D.; KRISHNAKUMAR, K.; WONG, D.; BERRY, M. Negative selection algorithm for aircraft fault detection. In: NICOSIA, G.; CUTELLO, V.; BENTLEY, P. J.; TIMMIS, J. (Ed.). **Artificial Immune Systems**. Berlin, Heidelberg: Springer Berlin Heidelberg, 2004. p. 1--13. ISBN 978-3-540-30220-9.

DOEBLING, S.; FARRAR, C.; PRIME, M.; SHEVITZ, D. Damage identification and health monitoring of structural and mechanical systems from changes in their vibration characteristics: A literature review. **Technical Report No. LA-13070-MS**, v. 30, 05 1996.

DOEBLING, S. W.; FARRAR, C.; PRIME, M. A summary review of vibration-based damage identification methods. v. 30, p. 91--105, 03 1998.

EBRAHIMIAN, M.; TODOROVSKA, M. I. Wave propagation in a timoshenko beam building model. **Journal of Engineering Mechanics**, v. 140, n. 5, p. 04014018, 2014.

ENDE, S. von; LAMMERING, R. Modeling and simulation of lamb wave generation with piezoelectric plates. **Mechanics of Advanced Materials and Structures**, Taylor & Francis, v. 16, n. 3, p. 188--197, 2009.

FILHO, J. V.; BAPTISTA, F. G.; INMAN, D. J. A pzt-based technique for shm using the coherence function. In: PROULX, T. (Ed.). **Advanced Aerospace Applications, Volume 1**. New York, NY: Springer New York, 2011. p. 111--118.

FILHO, J. V.; BAPTISTA, F. G.; INMAN, D. J. Time-domain analysis of piezoelectric impedance-based structural health monitoring using multilevel wavelet decomposition. **Mechanical Systems and Signal Processing**, v. 25, n. 5, p. 1550 -- 1558, 2011. ISSN 0888-3270.

GIURGIUTIU, V. Lamb wave generation with piezoelectric wafer active sensors for structural health monitoring. In: BAZ, A. M. (Ed.). **Smart Structures and Materials 2003: Smart Structures and Integrated Systems**. [S.l.]: SPIE, 2003. v. 5056, p. 111 -- 122.

GIURGIUTIU, V. Tuned lamb wave excitation and detection with piezoelectric wafer active sensors for structural health monitoring. **Journal of Intelligent Material Systems and Structures**, v. 16, n. 4, p. 291--305, 2005.

GIURGIUTIU, V. Chapter 4 - vibration of plates. In: GIURGIUTIU, V. (Ed.). **Structural Health Monitoring with Piezoelectric Wafer Active Sensors (Second Edition)**. Second edition. Oxford: Academic Press, 2014. p. 145 -- 197. ISBN 978-0-12-418691-0.

GIURGIUTIU, V. Chapter 5 - elastic waves. In: GIURGIUTIU, V. (Ed.). **Structural Health Monitoring with Piezoelectric Wafer Active Sensors (Second Edition)**. Second edition. Oxford: Academic Press, 2014. p. 199--292. ISBN 978-0-12-418691-0.

GIURGIUTIU, V. Chapter 6 - guided waves. In: GIURGIUTIU, V. (Ed.). **Structural Health Monitoring with Piezoelectric Wafer Active Sensors (Second Edition)**. Second edition. Oxford: Academic Press, 2014. p. 293--355. ISBN 978-0-12-418691-0.

GIURGIUTIU, V. Chapter 8 - coupling of pwas transducers to the monitored structure. In: GIURGIUTIU, V. (Ed.). **Structural Health Monitoring with Piezoelectric Wafer Active Sensors (Second Edition)**. Second edition. Oxford: Academic Press, 2014. p. 395--443. ISBN 978-0-12-418691-0.

GIURGIUTIU, V. **LABORATORY FOR ACTIVE MATERIALS AND SMART STRUCTURES products: softwares**. 2022.

GLUSHKOV, E.; GLUSHKOVA, N.; EREMIN, A.; GIURGIUTIU, V. Low-cost simulation of guided wave propagation in notched plate-like structures. **Journal of Sound and Vibration**, v. 352, p. 80 -- 91, 2015. ISSN 0022-460X.

GOLATO, A.; DEMIRLI, R.; SANTHANAM, S. Lamb wave scattering by a symmetric pair of surface-breaking cracks in a plate. **Wave Motion**, v. 51, n. 8, p. 1349 -- 1363, 2014. ISSN 0165-2125.

GONSALEZ-BUENO, C. G.

An investigation into the way in which longitudinal and flexural waves interact with corrosion-like damage, 2019. São Paulo State University (UNESP), School of Engineering of Ilha Solteira, Department of Mechanical Engineering, SP, Brazil.

GONSALEZ, C. G.; SILVA, S.; BRENNAN, M. J.; LOPES JR, V. Structural damage detection in an aeronautical panel using analysis of variance. **Mechanical Systems and Signal Processing**, v. 52-53, p. 206 -- 216, 2015. ISSN 0888-3270.

GRAFF, K. **Wave Motion in Elastic Solids**. [S.l.]: Dover Publications, 1991. (Dover Books on Physics Series). ISBN 9780486667454.

HAIDER, M. F.; BHUIYAN, M. Y.; PODDAR, B.; LIN, B.; GIURGIUTIU, V. Analytical and experimental investigation of the interaction of lamb waves in a stiffened aluminum plate with a horizontal crack at the root of the stiffener. **Journal of Sound and Vibration**, v. 431, p. 212 -- 225, 2018. ISSN 0022-460X.

HE, J.; HUO, H.; GUAN, X.; YANG, J. A lamb wave quantification model for inclined cracks with experimental validation. **Chinese Journal of Aeronautics**, 2020. ISSN 1000-9361.

HENDRICK, S. Damage detection and location in large space trusses. In: _____. **29th Structures, Structural Dynamics and Materials Conference**. [S.l.: s.n.], 1988.

HIBBELER, R. **Mechanics of Material**. [S.l.]: PRENTICE HALL BRASIL, 2010. ISBN 9788576053736.

HOU, J.; WANG, H.; XU, D.; JANKOWSKI, L.; WANG, P. Damage identification based on adding mass for liquid?solid coupling structures. **Applied Sciences**, v. 10, n. 7, 2020. ISSN 2076-3417.

HUANG, G.; SONG, F.; WANG, X. Quantitative modeling of coupled piezo-elastodynamic behavior of piezoelectric actuators bonded to an elastic medium for structural health monitoring: A review. **Sensors**, v. 10, n. 4, p. 3681--3702, 2010. ISSN 1424-8220.

KAPURIA, S.; AGRAHARI, J. K. Shear-lag solution for excitation, sensing, and time reversal of lamb waves for structural health monitoring. **Journal of Intelligent Material Systems and Structures**, v. 29, n. 4, p. 585--599, 2018.

KIM, B.; ROH, Y. Simple expressions of the reflection and transmission coefficients of fundamental lamb waves by a rectangular notch. **Ultrasonics**, v. 51, n. 6, p. 734 -- 744, 2011. ISSN 0041-624X.

KUBRUSLY, A. C.; WEID, J. P. von der; DIXON, S. Experimental and numerical investigation of the interaction of the first four sh guided wave modes with symmetric and non-symmetric discontinuities in plates. **NDT & E International**, v. 108, p. 102175, 2019. ISSN 0963-8695.

LEE, B. C.; STASZEWSKI, W. J. Modelling of lamb waves for damage detection in metallic structures: Part ii. wave interactions with damage. **Smart Materials and Structures**, v. 12, n. 5, p. 815, 2003.

LEE, J.; KIM, S. Structural damage detection in the frequency domain using neural networks. **Journal of Intelligent Material Systems and Structures**, v. 18, n. 8, p. 785--792, 2007.

LI, J.; KHODAEI, Z. S.; ALIABADI, M. H. Boundary element modelling of ultrasonic lamb waves for structural health monitoring. **Smart Materials and Structures**, IOP Publishing, v. 29, n. 10, p. 105030, sep 2020.

LIN, B.; GIURGIUTIU, V. Power and energy transduction analysis of piezoelectric wafer-active sensors for structural health monitoring. **Structural Health Monitoring**, v. 11, n. 1, p. 109--121, 2012.

LIN, B.; KAMAL, A.; GIURGIUTIU, V.; KAMAS, T. Multimodal lamb waves power and transfer function analysis of structurally-bonded pwas. In: . [S.l.: s.n.], 2012. (Smart Materials, Adaptive Structures and Intelligent Systems, Volume 1: Development and Characterization of Multifunctional Materials; Modeling, Simulation and Control of Adaptive Systems; Structural Health Monitoring), p. 765--771.

LIN, X.; YUAN, F. G. Diagnostic lamb waves in an integrated piezoelectric sensor/actuator plate: analytical and experimental studies. **Smart Materials and Structures**, IOP Publishing, v. 10, n. 5, p. 907--913, aug 2001.

LOPES JR, V.; PARK, G.; CUDNEY, H. H.; INMAN, D. J. Impedance-based structural health monitoring with artificial neural networks. **Journal of Intelligent Material Systems and Structures**, v. 11, n. 3, p. 206--214, 2000.

LOPES, K. W.; GONSALEZ-BUENO, C. G.; BUENO, D. D. On the frequencies for structural health monitoring in plates with symmetrical damage: An analytical approach. **Journal of Nondestructive Evaluation**, v. 41, n. 1, p. 29, 2022.

LOPES, K. W.; GONSALEZ-BUENO, C. G.; INMAN, D. J.; BUENO, D. D. On the frequencies for structural health monitoring in plates with symmetrical damage: An analytical approach. In: ASSOCIAÇÃO BRASILEIRA DE ENGENHARIA E CIÊNCIAS MECÂNICAS - ABCM. **26th International Congress of Mechanical Engineering (COBEM)**. [S.l.], 2021.

LOPES, K. W.; GONSALEZ-BUENO, C. G.; INMAN, D. J.; BUENO, D. D. On the frequencies for structural health monitoring in plates with asymmetrical damage: an analytical approach. In: FROMME, P.; SU, Z. (Ed.). **Health Monitoring of Structural and Biological Systems XVI**. [S.l.]: SPIE, 2022. v. 12048, p. 89 -- 104.

LOPES, K. W.; GONSALEZ-BUENO, C. G.; INMAN, D. J.; BUENO, D. D. Longitudinal wave scattering in thin plates with symmetric damage considering oblique incidence. **Ultrasonics**, p. 107161, 2023. ISSN 0041-624X.

LOPES, K. W.; GONSALEZ-BUENO, C. G.; INMAN, D. J.; BUENO, D. D. On the modeling of circular piezoelectric transducers for wave propagation-based structural health monitoring applications. **Journal of Intelligent Material Systems and Structures**, v. 0, n. 0, p. 1045389X221147668, 2023.

LOPES, K. W.; GONSALEZ-BUENO, C. G.; INMAN, D. J.; BUENO, D. D. On the symmetric damage detection with flexural waves using circular piezoelectric transducers. In: FROMME, P.; SU, Z. (Ed.). **Health Monitoring of Structural and Biological Systems XVII**. [S.l.]: SPIE, 2023. v. 12488, p. 124881W.

LOWE, M. J. S.; CAWLEY, P.; KAO, J.-Y.; DILIGENT, O. The low frequency reflection characteristics of the fundamental antisymmetric lamb wave a0 from a rectangular notch in a plate. **The Journal of the Acoustical Society of America**, v. 112, n. 6, p. 2612--2622, 2002.

LOWE, M. J. S.; DILIGENT, O. Low-frequency reflection characteristics of the s0 lamb wave from a rectangular notch in a plate. **The Journal of the Acoustical Society of America**, v. 111, n. 1, p. 64--74, 2002.

LUCA, A. D.; PERFETTO, D.; CAPUTO, F.; KHODAEI, Z. S.; ALIABADI, M. H. Simulation of guided waves in a cfrp plate at a specific temperature. In: RIZZO, P.; MILAZZO, A. (Ed.). **European Workshop on Structural Health Monitoring**. Cham: Springer International Publishing, 2023. p. 793--800. ISBN 978-3-031-07258-1.

LUCA, A. D.; PERFETTO, D.; LAMANNA, G.; AVERSANO, A.; CAPUTO, F. Numerical investigation on guided waves dispersion and scattering phenomena in stiffened panels. **Materials**, v. 15, n. 1, 2022. ISSN 1996-1944.

MACE, B. Wave reflection and transmission in beams. **Journal of Sound and Vibration**, v. 97, n. 2, p. 237 -- 246, 1984. ISSN 0022-460X.

MAL, A.; RICCI, F.; BANERJEE, S.; SHIH, F. A conceptual structural health monitoring system based on vibration and wave propagation. **Structural Health Monitoring**, v. 4, n. 3, p. 283--293, 2005.

MANKINS, J. C. **Technology Readiness Level**. [S.l.], 1995.

MARTIN, S. A.; JATA, K. V. FEM modeling of guided wave behavior in integrally stiffened plate structures. In: TOMIZUKA, M.; YUN, C.-B.; GIURGIUTIU, V. (Ed.). **Sensors and Smart Structures Technologies for Civil, Mechanical, and Aerospace Systems 2007**. [S.l.]: SPIE, 2007. v. 6529, p. 326 -- 336.

MIKLOWITZ, J. **The Theory of Elastic Waves and Waveguides**. [S.l.]: North Holland Publishing Company, 1978. (Applied mathematics and mechanics). ISBN 9780720405514.

NANDA, N.; KAPURIA, S. Spectral finite element for wave propagation analysis of laminated composite curved beams using classical and first order shear deformation theories. **Composite Structures**, v. 132, p. 310 -- 320, 2015. ISSN 0263-8223.

NASCIMENTO, R. F. **Wave propgation using finite element models of structural waveguide slices**. Thesis (Ph. D.), 2009. Engineering School, State University of Campinas.

NG, C.-T.; VEIDT, M. Scattering of the fundamental anti-symmetric lamb wave at delaminations in composite laminates. **The Journal of the Acoustical Society of America**, v. 129, n. 3, p. 1288--1296, 2011.

NIENWENHUI, J.; NEUMANN, J.; GREVE, D.; OPPENHEIM, I. Generation and detection of guided waves using pzt wafer transducers. **IEEE Transactions on Ultrasonics, Ferroelectrics, and Frequency Control**, v. 52, n. 11, p. 2103--2111, 2005.

NUCERA, C.; WHITE, S.; CHEN, Z. M.; KIM, H.; SCALEA, F. L. di. Impact monitoring in stiffened composite aerospace panels by wave propagation. **Structural Health Monitoring**, v. 14, n. 6, p. 547--557, 2015.

PAIN, D.; DRINKWATER, B. Detection of fibre waviness using ultrasonic array scattering data. **Journal of Nondestructive Evaluation**, v. 32, 09 2013.

PARK, D.-H.; HONG, S.-Y.; KIL, H.-G.; JEON, J.-J. Power flow models and analysis of in-plane waves in finite coupled thin plates. **Journal of Sound and Vibration**, v. 244, n. 4, p. 651 -- 668, 2001. ISSN 0022-460X.

PAU, A.; ACHILLOPOULOU, D. Interaction of shear and rayleigh?lamb waves with notches and voids in plate waveguides. **Materials**, v. 10, p. 841, 07 2017.

PAU, A.; ACHILLOPOULOU, D. V.; VESTRONI, F. Scattering of guided shear waves in plates with discontinuities. **NDT & E International**, v. 84, p. 67--75, 2016. ISSN 0963-8695.

PERFETTO, D.; LAMANNA, G.; PETRONE, G.; De Fenza, A.; De Luca, A. A modelling technique to investigate the effects of quasi-static loads on guided-wave based structural health monitoring systems. **Forces in Mechanics**, v. 9, p. 100125, 2022. ISSN 2666-3597.

PERFETTO, D.; LUCA, A. D.; LAMANNA, G.; CAPUTO, F. Analysis of guided waves dispersive behavior for damage detection in flat and curved composite panels. In: GERBINO, S.; LANZOTTI, A.; MARTORELLI, M.; BUIL, R. M.; RIZZI, C.; ROUCOULES, L. (Ed.). **Advances on Mechanics, Design Engineering and Manufacturing IV**. Cham: Springer International Publishing, 2023. p. 503--511.

PERFETTO, D.; LUCA, A. D.; LAMANNA, G.; MINARDO, A.; VALLIFUOCO, R.; CAPUTO, F. On the damage sensitivity of guided wave shm system under different loading conditions. In: LOPRESTO, V.; PAPA, I.; LANGELLA, A. (Ed.). **Dynamic Response and Failure of Composite Materials**. Cham: Springer International Publishing, 2023. p. 261--270.

PERFETTO, D.; Sharif Khodaei, Z.; De Luca, A.; ALIABADI, M.; CAPUTO, F. Experiments and modelling of ultrasonic waves in composite plates under varying temperature. **Ultrasonics**, v. 126, p. 106820, 2022. ISSN 0041-624X.

PODDAR, B.; GIURGIUTIU, V. Scattering of lamb waves from a discontinuity: An improved analytical approach. **Wave Motion**, v. 65, p. 79 -- 91, 2016. ISSN 0165-2125.

POVICH, C.; LIM, T. An artificial neural network approach to structural damage detection using frequency response functions. In: ______. **Adaptive Structures Forum**. [S.l.: s.n.], 1994.

RADWAŃSKA, M.; STANKIEWICZ, A.; WOSATKO, A.; PAMIN, J. **Plate and Shell Structures: Selected Analytical and Finite Element Solutions**. [S.l.]: Wiley, 2017. ISBN 9781118934548.

RAGHAVAN, A.; CESNIK, C. E. S. Modeling of piezoelectric-based Lamb wave generation and sensing for structural health monitoring. In: LIU, S.-C. (Ed.). **Smart Structures and Materials 2004: Sensors and Smart Structures Technologies for Civil, Mechanical, and Aerospace Systems**. [S.l.]: SPIE, 2004. v. 5391, p. 419 -- 430.

RAGHAVAN, A.; CESNIK, C. E. S. Finite-dimensional piezoelectric transducer modeling for guided wave based structural health monitoring. **Smart Materials and Structures**, IOP Publishing, v. 14, n. 6, p. 1448--1461, nov 2005.

RÉBILLAT, M.; HAJRYA, R.; MECHBAL, N. Nonlinear structural damage detection based on cascade of hammerstein models. **Mechanical Systems and Signal Processing**, v. 48, n. 1, p. 247--259, 2014. ISSN 0888-3270.

RHIM, J.; LEE, S. W. A neural network approach for damage detection and identification of structures. **Computational Mechanics**, v. 16, n. 6, p. 437--443, Nov 1995. ISSN 1432-0924.

ROBERTS, R. A. Guided wave propagation in integrally stiffened plates. **AIP Conference Proceedings**, v. 975, n. 1, p. 170--177, 2008.

RYUE, J.; THOMPSON, D.; WHITE, P.; THOMPSON, D. Wave reflection and transmission due to defects in infinite structural waveguides at high frequencies. **Journal of Sound and Vibration**, v. 330, n. 8, p. 1737 -- 1753, 2011. ISSN 0022-460X.

SANTHANAM, S.; DEMIRLI, R. Reflection of lamb waves obliquely incident on the free edge of a plate. **Ultrasonics**, v. 53, n. 1, p. 271 -- 282, 2013. ISSN 0041-624X.

SANTONI, G. B.; YU, L.; XU, B.; GIURGIUTIU, V. Lamb Wave-Mode Tuning of Piezoelectric Wafer Active Sensors for Structural Health Monitoring. **Journal of Vibration and Acoustics**, v. 129, n. 6, p. 752--762, 02 2007. ISSN 1048-9002.

SANTOS, R. B. **An alternative approach to design periodic rods**. Thesis (Ph. D.), 2018. Engineering School, São Paulo State University.

SANTOS, R. B.; CARNEIRO JR, J. P.; GONSALEZ-BUENO, C. G.; LUCCA, B. S. d.; BUENO, D. D. On the number of cells for flexural vibration suppression in periodic beams. **Meccanica**, v. 56, n. 11, p. 2813--2823, 2021.

SCALEA, F. Lanza di; MATT, H.; BARTOLI, I. The response of rectangular piezoelectric sensors to rayleigh and lamb ultrasonic waves. **The Journal of the Acoustical Society of America**, v. 121, n. 1, p. 175--187, 2007.

SCHAAL, C.; MAL, A. Lamb wave propagation in a plate with step discontinuities. **Wave Motion**, v. 66, p. 177 -- 189, 2016. ISSN 0165-2125.

SHEN, M.-H. H.; PIERRE, C. Natural modes of Bernoulli-Euler beams with symmetric cracks. **Journal of Sound and Vibration**, v. 138, n. 1, p. 115--134, 1990.

SHEN, Y.; GIURGIUTIU, V. Predictive modeling of nonlinear wave propagation for structural health monitoring with piezoelectric wafer active sensors. **Journal of Intelligent Material Systems and Structures**, v. 25, n. 4, p. 506--520, 2014.

SHEN, Y.; GIURGIUTIU, V. Combined analytical fem approach for efficient simulation of lamb wave damage detection. **Ultrasonics**, v. 69, p. 116--128, 2016. ISSN 0041-624X.

SILVA, S.; GONSALEZ, C. G.; LOPES JR., V. Adaptive filter feature identification for structural health monitoring in an aeronautical panel. **Structural Health Monitoring**, v. 10, n. 5, p. 481--489, 2011.

SPILLMAN, W.; HUSTON, D.; FUHR, P.; LORD, J. Neural network damage detection in a bridge element. **Proceedings of SPIE - The International Society for Optical Engineering**, 07 1993.

STASZEWSKI, W. Intelligent signal processing for damage detection in composite materials. **Composites Science and Technology**, v. 62, n. 7, p. 941 -- 950, 2002. ISSN 0266-3538.

SZEFI, J. T. **Helicopter gearbox isolation using periodically layered fluidic isolators**. Thesis (Ph. D.) --- The Pennsylvania State University, July 2003.

UGURAL, A. C. **Plates and Shells: Theory and Analysis**. 4th ed.. ed. [S.l.]: CRC Press, 2017.

WU, X.; GHABOUSSI, J.; GARRETT, J. Use of neural networks in detection of structural damage. **Computers & Structures**, v. 42, n. 4, p. 649 -- 659, 1992. ISSN 0045-7949.

XU, B.; GIURGIUTIU, V. Single mode tuning effects on lamb wave time reversal with piezoelectric wafer active sensors for structural health monitoring. **Journal of Nondestructive Evaluation**, v. 26, n. 2, p. 123--134, 2007.

YEO, S.-J.; HONG, S.-Y.; SONG, J.-H.; KWON, H.-W. Vibrational energy flow models for dilatational wave in elastic solids. **Advances in Mechanical Engineering**, v. 9, n. 12, p. 1687814017740709, 2017.

YEUM, C. M.; SOHN, H.; IHN, J. B. Lamb wave mode decomposition using concentric ring and circular piezoelectric transducers. **Wave Motion**, v. 48, n. 4, p. 358--370, 2011. ISSN 0165-2125.

YU, L.; BOTTAI-SANTONI, G.; GIURGIUTIU, V. Shear lag solution for tuning ultrasonic piezoelectric wafer active sensors with applications to lamb wave array imaging. **International Journal of Engineering Science**, v. 48, n. 10, p. 848--861, 2010. ISSN 0020-7225. Structural Health Monitoring in the Light of Inverse Problems of Mechanics.

YU, L.; SANTONI-BOTTAI, G.; XU, B.; LIU, W.; GIURGIUTIU, V. Piezoelectric wafer active sensors for in situ ultrasonic-guided wave shm. **Fatigue & Fracture of Engineering Materials & Structures**, v. 31, n. 8, p. 611--628, 2008.